Fakultät für Medizin

Characterization of the tumor microenvironment and cell-cell communication networks in pancreatic cancer subtypes

Stefanie Bärthel

Vollständiger Abdruck der von der Fakultät für Medizin der Technischen Universität
München zur Erlangung des akademischen Grades eines

Doctor of Philosophy (Ph.D.)

genehmigten Dissertation.

Vorsitzende: Prof. Dr. Alessandra Moretti

Betreuer: Prof. Dr. Dieter Saur

Prüfer der Dissertation:

1. Prof. Dr. Marc Schmidt-Supprian

2. Prof. Dr. Laszlo Nagy

3. Prof. Dr. Bernd Engelmann

Die Dissertation wurde am 11.07.2022 bei der Fakultät für Medizin der Technischen Universität München eingereicht und durch die Fakultät für Medizin am 08.09.2022 angenommen.

I. TABLE OF CONTENTS

II. LIST OF FIGURES

III. ABBREVIATIONS

ADEX	Aberrantly Differentiated Endocrine Exocrine
apCAF	Antigen presenting CAFs
APP	Amyloid precursor protein
CAF	Cancer-associated fibroblast
CRC	Colorectal cancer
CyTOF	Cytometry by time of flight
DMEM	Dulbecco’s modified eagle medium
ECC	Extrahepatic cholangiocarcinoma
ECM	Extracellular matrix
ER	Endoplasmic reticulum
FCS	Fetal calve serum
FFPE	Formalin fixed paraffin embedded
GEM	Gel-bead in emulsion
GEMM	Genetically engineered mouse models
H&E	Hematoxylin and eosin
iCAF	Inflammatory CAF
ICB	Immune checkpoint blockade
IHC	Immunohistochemistry
I-E TME	Infiltrated-excluded TME
I-I TME	Infiltrated-inflamed TME
IPMN	Intraductal papillary mucinous neoplasms
LSL	*LoxP-stop-LoxP*
loxP	locus of X-over P1
MCN	Mucinous cystic neoplasms
MDSC	Myeloid derived suppressor cells
MHC	Major histocompatibility complex
MSI	Microsatellite instable
myoCAF	Myofibroblastic CAF
NET	Neutrophil extracellular trap
NGS	Next generation sequencing
PanIN	Pancreatic intraepithelial neoplasms
PBS	Phosphate buffered saline
PCR	Polymerase chain reaction
PDAC	Pancreatic ductal adenocarcinoma
PD-L1	Programmed death-ligand 1
PMN	polymorphonuclear
PSC	Pancreatic stellate cells
RNA	Ribonucleic acid
scRNA-seq	Single-cell RNA sequencing
subTMEs	Sub-tumor microenvironment
TAM	Tumor associated macrophage
TIGIT	T cell immunoreceptor with Ig and ITIM domains
TME	Tumor microenvironment
Treg	Regulatory T cell
UMAP	Uniform Manifold Approximation and Projection
UMI	Unique molecular identifier

IV. ABSTRACT

Pancreatic ductal adenocarcinoma (PDAC) is a complex disease displaying extensive genetic heterogeneity along with a tumor microenvironment (TME) unique in its composition. While the PDAC TME is known to be highly immunosuppressive, the drivers of distinct TME states and modes of immunosuppression remain elusive. Moreover, it is poorly understood how distinct genetic alterations affect TME cell type recruitment and how this, in turn, influences progression and treatment outcome. Therefore, we systematically investigated the TME states and cell-cell communication networks in molecular PDAC subtypes.

Here, we describe the TME landscape of a comprehensive, genetically well-defined tumor cohort derived from PDAC mouse models, which represent multiple molecular subtypes. We used a multimodal approach by integrating single-cell RNA-sequencing (scRNA-seq) with histopathological, spatial transcriptomics and secretome analysis. Our results show that tumors of distinct molecular PDAC subtypes recruit divergent subpopulations of infiltrating immune cells, most notably evidenced by major differences in frequency and phenotype of macrophages and neutrophils. Functional secretome analysis of well-characterized *Kras*-driven mouse PDAC cell lines revealed subtype-specific factors which differ between the two main transcriptional subtypes (classical and mesenchymal). Accordingly, crosstalk between tumor and immune cells inferred by ligand-receptor interaction analysis from scRNA-seq data nominates the CSF signaling network as a key player in mesenchymal PDAC. Classical tumors, in contrast, leverage CXCL signaling hubs to mediate higher infiltration of immunosuppressive neutrophils. Moreover, immune checkpoint signaling by PD-L1 and TIGIT was elevated in mesenchymal PDAC.

In this work, we systematically delineate the subtype-specific TME states and cell-cell communication networks of PDAC. Our findings pinpoint molecular pathomechanisms that shape cell type recruitment and abundance into this immunologically cold tumor type and aid the identification of potential immunotherapeutic vulnerabilities. These results could be deployed for future therapeutic interventions directed towards immunomodulation and subtype-specific combinatorial therapies.

V. ZUSAMMENFASSUNG

Das duktale Pankreaskarzinom (PDAC) ist eine genetisch sehr komplexe Tumorentität, welche eine äußerst schlechte Prognose aufweist. Des Weiteren besitzt PDAC eine hohe genetische Heterogenität, sowie ein immunsuppressives Tumormikromilieu. Es ist bisher nur unzureichend charakterisiert, wie verschiedene Phänotypen des Tumormikromilieus zu Stande kommen und welche Mechanismen zur Entstehung eines immunsuppressiven Tumormikromilieus führen. Weiterhin ist noch unerforscht, wie verschiedene genetische Veränderungen der Tumoren die Rekrutierung von Immunzellen modulieren, und wie dies wiederum die Tumorprogression und den Therapieerfolg von PDAC-Patienten beeinflusst.

In der hier vorliegenden Arbeit wurde daher eine systematische Analyse der Tumormikromilieu-Phänotypen und der entsprechenden Zell-Zell-Kommunikationsnetzwerke in verschiedenen molekularen PDAC-Subtypen durchgeführt. Diese Analyse wurde in einer umfangreichen, genetisch charakterisierten Kohorte von PDAC-Mausmodellen mittels multimodaler Integration von scRNA-seq (Einzelzell-Transkriptom-Sequenzierung) Daten, histopathologischen Parametern, Spatial Transcriptomics (räumliche Transkriptom Analyse) Daten und den entsprechenden Sekretomen durchgeführt. Unsere Ergebnisse zeigen, dass sich das Tumormikromilieu verschiedener molekularer PDAC-Subtypen durch Infiltration von unterschiedlichen Immunzellen auszeichnet. Ein Beispiel ist der signifikante Unterschied in der Rekrutierung von Makrophagen und Neutrophilen. Durch eine funktionelle Sekretom-Analyse von Zellkulturen eines *Kras*^{G12D}-induzierten murinen PDAC-Modells wurden subtyp-spezifische sezernierte Faktoren identifiziert, die sich zwischen dem klassischem und dem mesenchymalem PDAC Subtyp unterscheiden. Weiterhin wurden die zugrundeliegenden Zell-Zell Interaktionen zwischen Tumor- und Immunzellen mithilfe einer Liganden-Rezeptoren-Interaktionsanalyse der scRNA-seq-Daten in den beiden PDAC Subtypen analysiert. Im mesenchymalen Subtyp interagieren Tumorzellen mit Makrophagen durch den CSF-Signalweg, wohingegen im klassischen PDAC die Interaktion von Tumorzellen mit Neutrophilen hauptsächlich über den CXCL-Signalweg stattfindet. Weiterhin ist der mesenchymale PDAC-Subtyp durch eine höhere Expression von Immun-Checkpoint-Signalwegen, wie PD-L1 und TIGIT, gekennzeichnet.

Zusammenfassend wurden sowohl die Komposition des Subtyp-spezifischen PDAC Tumormikromilieus charakterisiert, als auch Zell-Zell-Kommunikationsnetzwerke in klassischen und mesenchymalen Tumoren identifiziert. Durch diese Ergebnisse wurden molekulare Pathomechanismen aufgedeckt, welche der tumor-vermittelten Immunzellrekrutierung zu Grunde liegen. Unsere Analyse zeigt zahlreiche therapeutische Angriffspunkte im Tumormikromilieu auf, die in Zukunft für effektivere Therapiestrategien genutzt werden können. Dies kann z.B. durch eine Umprogrammierung des Tumormikromilieus oder durch die Kombination von immunmodulatorischen Therapien mit Tumorzell-fokussierten Therapeutika geschehen.

1. INTRODUCTION

1.1. Pancreatic ductal adenocarcinoma

Pancreatic cancer is a complex and heterogeneous tumor type characterized by a poor prognosis and high therapeutic resistance. In comparison to other tumor entities, the 5-year relative survival rate is one of the lowest with around 11% (Siegel et al., 2022). Moreover, pancreatic cancer is projected to become the second leading cause of cancer related deaths within the next decade, accompanied by rising incidence (Rahib et al., 2014; Ying et al., 2016).

Pancreatic ductal adenocarcinoma (PDAC) is the most common histological subtype of pancreatic cancer, accounting for over 85% of cases (Klimstra et al., 2009). A myriad of reasons contributes to the poor outcome in PDAC, including late-stage diagnosis (due to lack of early detection markers) aggravating resectability of end-stage tumors, frequent metastasis formation, and the lack of effective therapeutic options. On a genetic level, molecular analyses of large human PDAC cohorts revealed a complex genetic landscape with only few prevalent driver mutations, namely mutations in *KRAS* and the tumor suppressor genes *TP53, CDKN2A* and *SMAD4*, followed by multiple genetic alterations found at lower frequencies (Waddell et al., 2015; Witkiewicz et al., 2015). In addition to the genetic heterogeneity, PDAC is characterized by a stroma-rich, highly immunosuppressive tumor microenvironment (TME) diverse in its cellular composition, including multiple immune and stromal cell types (Hosein et al., 2020; Neesse et al., 2015). These unique characteristics present a challenge for the identification of therapeutic vulnerabilities and more effective treatment strategies **(Figure 1)**.

PDAC arises from the exocrine pancreas compartment and is preceded by microscopic precursors lesions, such as pancreatic intraepithelial (PanINs), intraductal papillary mucinous neoplasms (IPMNs) and mucinous cystic neoplasms (MCNs) which eventually progress to invasive carcinomas. As the most common precursor lesion, PanINs are characterized to advance through a stepwise progression due to acquisition of several key mutations (Hruban et al., 2000; Maitra and Hruban, 2008). Oncogenic *KRAS* mutations (> 90% patients) can already be detected in pre-cancerous lesions and early-stage PanINs (Kanda et al., 2012; Mueller et al., 2018). In high-grade PanINs as well as PDAC, additional mutations in *TP53, SMAD4* and *CDKN2A* are found in > 50% of patients, thus representing predominant mutations beyond *KRAS*. While other mutations, such as *ARID1A, KDM6A, MLL3 and TGFBR2* are present in a subset of patients (5-10%), most of the genetic alterations occur at lower frequencies (< 5%) (Bailey et al., 2016; Collisson et al., 2019).

For resectable PDAC, surgery remains the main option to tackle the disease. As most patients relapse after surgery, adjuvant chemotherapy with FOLFORINOX (a combination of folinic acid, fluorouracil, irinotecan and oxaliplatin) or gemcitabine-capecitabine is recommended after resection which has been shown to result in long-term survival for a subset of patients (Conroy et al., 2018; Neoptolemos et al., 2018). However, resection is not an option for >85% of PDAC patients due to advanced tumor stage, typically manifested as borderline resectable and/or locally advanced unresectable or metastatic PDAC. For the latter diagnosis, first-line treatment is chemotherapy, either by administration of FOLFIRINOX or nanoparticle albumin-bound paclitaxel (nab-paclitaxel) plus gemcitabine (Neoptolemos et al., 2018). For metastatic PDAC, FOLFORINOX led to a significantly overall survival benefit with a median of 11.1 months in comparison to gemcitabine (Conroy et al., 2011). Nab-paclitaxel in combination with gemcitabine significantly increased survival to 8.5 months compared to gemcitabine monotherapy (Von Hoff et al., 2013). For borderline resectable and/or locally advanced unresectable PDAC, neoadjuvant chemotherapy with FOLFORINOX constitutes the consensus treatment option (Neoptolemos et al., 2018). Dismal for patients, none of these therapy options generally evoked durable remissions and a large fraction of patients shows therapeutic resistance (Aung et al., 2018). Moreover, targeted therapy approaches have so far failed in clinical trials, albeit their extensive preclinical research and validation in mouse models. This leaves current research efforts with the task to systematically investigate pancreatic cancer intratumor- and TME heterogeneity with the aim of designing more effective therapeutic approaches, ultimately striving to achieve better outcomes for patients.

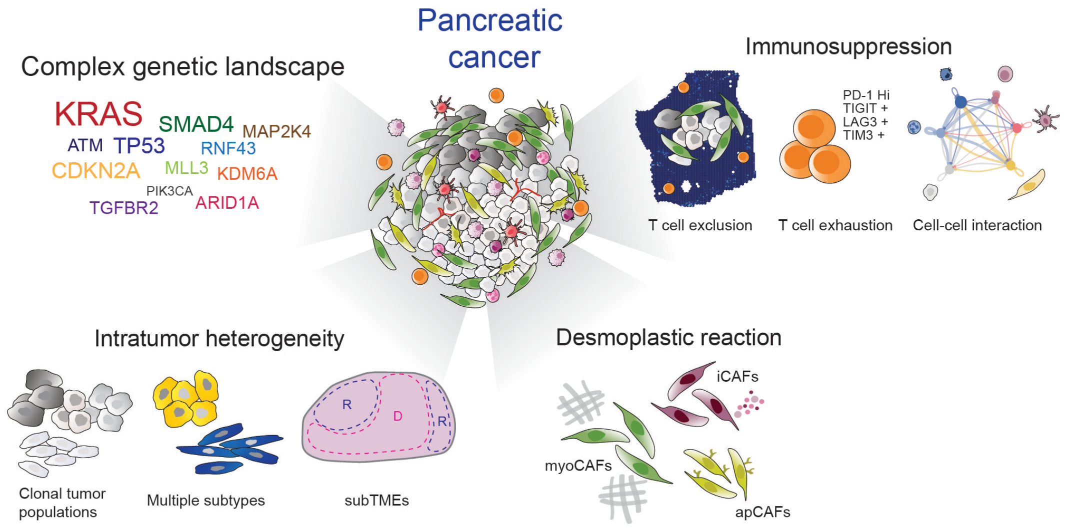

Figure 1. Hallmarks of pancreatic cancer

PDAC is a complex disease and characterized by several hallmarks: Left, PDAC displays a complex genetic landscape with *KRAS* mutations as main driver event in >90% of patients and *TP53, CDKN2A and SMAD4* mutations in >50% cases. Other genetic alterations occur at lower frequencies. Moreover, PDAC shows an extensive intratumor heterogeneity including clonal tumor populations, the presence of multiple subtypes within one tumor as well as multiple sub tumor microenvironments (subTMEs; R - reactive, D – deserted). Right, the PDAC TME is considered highly immunosuppressive leading to exclusion of T cells from the tumor core, T cell exhaustion and a dysfunctional T cell compartment. Immunosuppression is mediated by complex cell-cell interactions between all cell types within the tumor. In addition, PDAC presents a strong desmoplastic reaction and is designated as a stroma-rich tumor type. Cancer-associated fibroblasts (CAFs) show diverse phenotypes and modulate ECM production, immunosuppression and build the structural TME.

1.2. Molecular subtypes of PDAC

In the last decade, various sequencing studies conducted on human PDAC specimens allowed to investigate the extensive heterogeneity of the disease. Moreover, PDAC tumors could be stratified into molecular subtypes based on their transcriptional and histopathological profile.

1.2.1. Bulk RNA-sequencing subtyping approaches

In the first of these studies, Collisson et al defined three subtypes, namely classical, quasi-mesenchymal and exocrine-like, based on microarray data from microdissected PDAC epithelium obtained from treatment-naïve patients. Notably, the quasi-mesenchymal subtype was associated with poor prognosis and advanced stage of the tumors (Collisson et al., 2011). Further subtyping efforts by Moffitt and Bailey allowed more refined classifications, showing substantial overlap with the subtypes described by Collisson (Bailey et al., 2016; Collisson et al., 2011; Moffitt et al., 2015). Moffitt et al defined the basal-like and classical subtype as well as two stroma signatures which were designated as activated and normal stroma (Moffitt et al., 2015). Bailey et al proposed the occurrence of four distinct subtypes, which were named squamous, pancreatic progenitor, immunogenic and aberrantly differentiated endocrine exocrine (ADEX) (Bailey et al., 2016). Consistent within these classifications, the quasi-mesenchymal (Collisson), basal-like (Moffitt) and squamous (Bailey) subtypes were identified in corresponding data sets of other classifications, each showing association with poor survival and advanced disease stage compared to the classical subtypes. Therefore, all mentioned subtypes can be stratified into two major subtypes, which show features of classical (e.g. pancreatic progenitor) and mesenchymal (e.g. basal-like, squamous, quasi-mesenchymal) PDAC (Bailey et al., 2016; Chan-Seng-Yue et al., 2020; Collisson et al., 2019; Collisson et al., 2011; Kalimuthu et al., 2020; Moffitt et al., 2015). Generally, the classical PDAC subtype is characterized by a well-differentiated histopathology, associated with a better prognosis and shows a partial response to standard-of-care chemotherapy (Aung et al., 2018; Kalimuthu et al., 2020). Furthermore, classical PDAC shows a high expression of the transcription factor *GATA6,* which cooperates with *HNF1A* and *HNF4A* to sustain the epithelial identity and classical phenotype. Loss of *GATA6* is necessary for a shift to a mesenchymal gene expression state (Kloesch et al., 2022; Martinelli et al., 2017). Conversely, the mesenchymal PDAC subtype is associated with a poorly differentiated histopathology and exhibits mutations in chromatin modifiers such as *KDM6A, MLL2* and *MLL3* as well as *TP53* and *TP63* (Andricovich et al., 2018; Bailey et al., 2016; Collisson et al., 2011; Kalimuthu et al., 2020; Somerville et al., 2018). The mesenchymal subtype is further highly resistant to standard-of-care chemotherapy compared to classical PDAC and correlates with a poor prognosis in patients (Aung et al., 2018).

In conclusion, the stratification of molecular PDAC subtypes presents an important approach to predict prognosis and treatment outcome in PDAC patients but is currently not used to inform treatment strategies (Collisson et al., 2019). The identification of subtype-specific therapeutic vulnerabilities will help to improve treatment outcome, especially in the aggressive and highly resistant mesenchymal subtype. One important advancement to systematically analyze tumor-cell intrinsic features of the different subtypes was the generation of subtype-specific preclinical genetically engineered mouse models (GEMMs) which recapitulate the human diseases. With the help of these models, genotype-phenotype associations could be analyzed in great depth and evolutionary routes of PDAC tumorigenesis were delineated. For example, the mesenchymal subtype was characterized by homozygous loss of the tumor suppressor *Cdkn2a*, promoting a $\textit{Kras}^{MUT}$ oncogenic dosage increase and leading to an undifferentiated, highly metastatic phenotype, whereas the classical subtype was characterized by amplifications of alternative oncogenes (*Myc, Nfkb2* and *Yap1*) and lower $\textit{Kras}^{MUT}$ expression as well as more differentiated histology and lower metastatic potential (Miyabayashi et al., 2020; Mueller et al., 2018; Tiriac et al., 2018).

In addition to tumor cell heterogeneity, PDAC is described as a stroma-rich tumor type with a high desmoplastic reaction, posing a major challenge to evaluate not only the tumor cell subtype states but also to consider the surrounding stroma. The strong desmoplastic reaction of tumors has been shown to present a barrier for effective drug delivery as well as elicit tumor promoting features (Hosein et al., 2020; Neesse et al., 2015).

In addition to the identification of molecular PDAC subtypes of the malignant cell compartment, multiple studies described TME-related immune and stromal gene expression signatures (Bailey et al., 2016; Maurer et al., 2019; Moffitt et al., 2015; Nicolle et al., 2017; Puleo et al., 2018). For example, three distinct stromal and immune subtypes were identified in a study by Puleo et al, namely the immune classical, desmoplastic as well as stroma activated subtype, with the two latter correlating with a poor prognosis in PDAC patients (Puleo et al., 2018). Maurer et al identified two TME-related subtypes which are described as extracellular matrix-rich (ECM-rich) and immune-rich subtypes. Mesenchymal/ECM-rich tumors were associated with a poorer prognosis in comparison to classical/immune-rich PDAC (Maurer et al., 2019). These findings highlight the importance to acknowledge the heterogenous PDAC TME and further study the characteristics of subtype-specific TME composition, as this has the potential to aid the identification of therapeutic vulnerabilities, ideally by combinatorial approaches targeting the tumor cells and TME simultaneously.

All mentioned PDAC subtyping studies were derived from bulk RNA-seq measurements and thereby potentially disguise intratumor heterogeneity. Hence, the existence of multiple subtypes within the same tumor or intermediate cell states of a tumor cell as well as the presence of multiple tumor cell clones may be masked. Additionally, many studies enriched the tumor cell fraction for subtype stratification, but did not connect them to distinct TME features, thereby obscuring the heterogeneity of multiple diverse immune and stromal cell types in the PDAC TME.

1.2.2. scRNA-sequencing subtyping approaches

With the advent of single-cell profiling methods, particularly single-cell RNA sequencing (scRNA-seq), it became possible to delineate PDAC subtype states and TME heterogeneity at a high resolution (Chan-Seng-Yue et al., 2020; Hosein et al., 2019; Juiz et al., 2020; Krieger et al., 2021; Lin et al., 2020; Raghavan et al., 2021).

In a study by Chan-Seng-Yue and colleagues, the authors performed RNA-seq subtyping of purified PDAC epithelium within a large patient cohort and refined the existing subtype stratification into five distinct subtypes, namely Basal-like A, Basal-like B, Hybrid, Classical-A and Classical-B subtypes. The Hybrid cluster was characterized by co-expression of mesenchymal (basal-like) and classical gene expression signatures, indicating a high intratumor heterogeneity for a large subset of PDAC patients. Using scRNA-seq of resected PDAC, the intratumoral co-existence of classical and mesenchymal PDAC subtypes could be further elucidated. Notably, in >85% of the cases both classical and mesenchymal tumor cells were present within the same tumor, accentuating the high heterogeneity of PDAC (Chan-Seng-Yue et al., 2020). Moreover, Raghavan et al identified an 'intermediate co-expressor' subtype presenting intermediate expression levels of classical and mesenchymal signatures within individual PDAC cells in addition to the previously classical and mesenchymal subtypes. The scRNA-seq data set was generated from metastatic PDAC patient samples and scRNA-seq analysis was performed from biopsies as well as patient-matched *in vitro* organoid cultures. Cells expressing the intermediate co-expressor subtype signature showed elevated expression of genes related to RAS signaling, inflammatory/stress response as well as enrichment in developmental gene sets. This novel subtype might represent a transitional state between the classical and mesenchymal subtype. In addition, the identified subtypes were linked to TME associations inferred from the scRNA-seq data set of non-malignant cells, thereby delineating state-specific TME compositions. The mesenchymal subtype was enriched in *C1QC*$^+$ macrophages and displayed a low TME diversity. Conversely, the classical subtype showed a higher TME cell type diversity and specific enrichment in *SPP1*$^+$ macrophages. The intermediate co-expressor subtype presented a higher T cell infiltration (*IFNG*$^+$ CD8$^+$ T cells) compared to classical and mesenchymal subtypes (Raghavan et al., 2021). This study suggests striking differences between molecular PDAC subtypes, which warrant further systematical validation. As indicated by the previously mentioned study, mesenchymal PDAC correlates with a higher infiltration of macrophages. In line with these observations, Tu et al. propose a cell-cell interaction model between TNFα-expressing macrophages and mesenchymal PDAC cells, in which the malignant cells secrete the chemokine CCL2 leading to recruitment of TNFα^+ macrophages which in turn sustain the aggressive mesenchymal cell state (Tu et al., 2021).

In conclusion, scRNA-seq analyses refined previous PDAC subtype classifications and revealed intermediate subtype states. Moreover, single-cell profiling offers the possibility to connect tumor cell states with TME features, which needs to be analyzed more systematically to dissect the subtype-specific cell-cell communication networks.

1.3. Tumor microenvironment of PDAC

The TME of PDAC is special in multifaceted aspects, both with regard to occurrence of immune and stromal cell types as well as their corresponding functions and phenotypes. According to the diverse tasks of various cell types, the PDAC TME can be compartmentalized into the structural and immune TME. Grünwald et al recently contextualized the structural and immune TME of PDAC by classification of recurrent TME phenotypes, namely the deserted, reactive and intermediate TME phenotypes. The deserted TME is described as immunologically “cold” with an accumulation of thin, spindle shaped cancer-associated fibroblasts (CAFs), whereas the reactive TME is characterized as immunologically “hot”, thus showing enrichment in plump CAFs with enlarged nuclei. The intermediate TME represents a transitional phenotype with characteristics of both TMEs. As these TME phenotypes co-occurred within the same tumor in defined spatial localizations, they were further annotated as “sub-tumor microenvironments” (subTMEs), corroborating the observation of extensive intratumor heterogeneity in PDAC (Grünwald et al., 2021). The two major subTME phenotypes displayed distinct characteristics with respect to ECM deposition, CAF activation and immune cell infiltrates. Moreover, they could be correlated to treatment outcome in PDAC patients, as for instance the deserted subTME showed higher resistance to chemotherapy. Co-occurrence of the deserted and reactive subTMEs was associated with the poorest prognosis compared to tumors which consist in main parts of only one subTME (Grünwald et al., 2021). In the following paragraphs, the composition of the structural and immune PDAC TME as well as functional implications are specified.

1.3.1. The structural TME in PDAC

One hallmark of PDAC is a strong desmoplastic reaction, leading to a stroma-rich tumor. This stroma is characterized by the presence of numerous CAF subpopulations responsible for ECM production which shapes the so-called ‘structural TME’. Pancreatic stellate cells (PSC), a cell type present in the healthy pancreas as well, are one source of activated CAFs in the TME and transdifferentiate during tumorigenesis. CAFs exhibit various functions, such as remodeling of the ECM, regulation of metabolic functions, immune cell crosstalk and secretion of growth and other soluble factors. Due to the extensive ECM deposition and fibrotic reaction, the structural TME presents a barrier for effective drug delivery to the tumor core and hinders vascularization of the tumor (Hosein et al., 2020; Neesse et al., 2015; Rhim et al., 2014; Sahai et al., 2020). Generally, CAFs are associated with tumor promoting functions by influencing tumor growth, mediating immunosuppression and possibly tumor cell dissemination; however, there is also evidence of tumor restricting functions of specific CAF subsets (Sahai et al., 2020). Recently, multiple CAF subpopulations were identified based on specific gene expression profiles and their spatial distribution within the tumor. The major CAF subsets are termed myofibroblastic CAFs (myoCAFs), inflammatory CAFs (iCAFs) and antigen presenting CAFs (apCAFs). MyoCAFs are characterized by elevated expression levels of *aSMA*, upregulated TGFβ signaling and a localization in close proximity to tumor cells. In contrast, iCAFs are localized further away from the tumor cells and generally dispersed within the tumor stroma. They are associated with a secretory phenotype and high expression of *IL6* and *LIF* (Biffi et al., 2019; Öhlund et al., 2017). The apCAF subpopulation was identified in a recent scRNA-seq analysis of human and mouse PDAC tumors. This CAF subset shows high expression of *MHCII* and *CD74* but lacks the expression of co-stimulatory molecules needed for induction of T cell proliferation (Elyada et al., 2019). It was recently shown that apCAFs originate from mesothelial cells in PDAC and that they are inducing regulatory T cell (Treg) differentiation and proliferation, thereby fostering an immunosuppressive phenotype (Huang et al., 2022).

1.3.2. The immune TME in PDAC

The other of the identified TME compartments, the immune TME, can be further sub-stratified on a pan-cancer level into two distinct groups according to immune cell infiltration and spatial dispersion of immune cell subpopulations. These two subgroups are the infiltrated-excluded (I-E TME) and infiltrated-inflamed TME (I-I TME). PDAC is associated with the I-E TME class and described as immunologically “cold” and highly immunosuppressive tumor as cytotoxic T cells are excluded from the tumor core and display a dysfunctional phenotype (Binnewies et al., 2018). In addition, PDAC is highly infiltrated by myeloid cell populations which are thought to mediate immunosuppression of T cells (Veglia et al., 2021b; Zhu et al., 2017). Moreover, PDAC is eminently refractory to immune checkpoint blockade (ICB) which prominently led to higher response rates in other solid tumor entities, such as melanoma and lung cancer (Bear et al., 2020; Thorsson et al., 2018), further corroborating the lack of activated immune cells in PDAC.

In contrast, tumors displaying an I-I TME are described as immunologically “hot” tumors, characterized by high infiltration rates of activated T cells and clinical response to ICB, e.g. in MSI-high colorecral cancer (CRC). These are features not frequently observed in PDAC (Binnewies et al., 2018).

Recently, numerous studies set out to characterize the heterogenous PDAC immune TME in large patient cohorts by using a multimodal approach including scRNA-seq, multiplexed immunohistochemistry and flow cytometry analyses to delineate phenotypes and spatial localization of immune cell infiltrates (Grünwald et al., 2021; Hosein et al., 2019; Kemp et al., 2021b; Liudahl et al., 2021; Steele et al., 2020). Multiplexed immunohistochemistry analysis of treatment-naïve, resected PDAC identified distinct immune phenotypes based on cell type densities which could be stratified into hypo-inflamed, myeloid and lymphoid immune TMEs. However, no association between the immune clusters and overall survival of patients was detected. Moreover, densities of immune cells varied substantially within individual tumors, with respect to both histological regions as well as patients (Liudahl et al., 2021). Using scRNA-seq analyses, the PDAC immune landscape could be analyzed at a high resolution. Steele et al combined scRNA-seq, CyTOF (Cytometry by time of flight) and multiplexed immunohistochemistry analyses to systematically delineate immune cell infiltration in PDAC as well as peripheral blood of patients. The expression levels of immune checkpoints, which can be harnessed for immunotherapy, differed between immune cell populations and individual patients indicating a high level of heterogeneity. Profiled $CD8^+$ T cells of PDAC showed an exhausted phenotype by expressing exhaustion markers such as *EOMES* and *GZMK.* The receptor *TIGIT* was the only immune checkpoint receptor that showed higher expression levels in $CD8^+$ T cells when comparing PDAC with adjacent normal tissue. Interestingly, *TIGIT*-positive cells could also be identified in patient's blood and correlated with the expression levels in the tumor. Hence, *TIGIT* inhibition might present a therapeutic vulnerability in patients with elevated expression of this immune receptor (Steele et al., 2020). Myeloid cells, in particular macrophages and neutrophils, are one of the most abundant immune cell types in PDAC. Single-cell profiling of human and mouse PDAC models characterized the phenotypic diversity of these cell types. Tumor associated macrophages (TAMs) show high expression of the complement factors *C1QA* and *C1QB* as well as *APOE*, *TREM2* and *ARG1*. Conversely, expression of the *C1Q* complement factors and *APOE* was also observed in the blood samples of PDAC patients (Kemp et al., 2021a; Kemp et al., 2021b). Co-expression of *Trem2* and *Arg1* in TAMs was previously described as a feature of immunosuppressive myeloid derived suppressor cells (MDSC) in a mouse fibrosarcoma model. Subsequent ablation of *Trem2* decreased exhausted T cells and led to an increase in cytotoxic T and NK cells (Katzenelenbogen et al., 2020). Activated *Arg1* signaling mediates immunosuppression by leading to a deficiency of arginase in the TME which is needed for T cell activation and proliferation (Bronte et al., 2003). Multiple chemoattractants including cytokines, chemokines and interleukins are known to recruit macrophages to tumors. Specifically, the chemokines CCL2, CCL3, CCL4 and CXCL12, the cytokine CSF1 as well as IL-6, IL-1β and VEGFA are known to induce macrophage/monocyte recruitment to the tumor (Lesokhin et al., 2012; Pathria et al., 2019).

Neutrophil-like polymorphonuclear MDSCs (PMN-MDSC) are another immunosuppressive myeloid population originating from the granulocytic myeloid lineage and are associated with poor prognosis in cancer patients. PMN-MDSCs enable suppression of T cells, B cells and NK cells by different modes, e.g. upregulation of *STAT3, ARG1 and S100A8/A9 as well as* induction of endoplasmic reticulum (ER) stress signaling. Moreover, they also play a role in metastatic dissemination of tumor cells and are involved in formation of the pre-metastatic niche (Veglia et al., 2021b). Recruitment of PMN-MDSC to the tumor site is controlled by chemoattractants such as G-CSF, GM-CSF and IL-1 (Bronte et al., 2016; Veglia et al., 2021b).

In summary, the immune PDAC TME represents an accumulation of immunosuppressive myeloid cell subpopulations which lead to repression of T cells. However, the exact modes of immunosuppression and complex cell-cell interactions between tumor, myeloid and T cells in PDAC have not been systematically delineated so far.

1.3.3. Therapeutic approaches to target the PDAC TME

The composition of the PDAC TME offers many potential therapeutic opportunities by targeting the fibrotic stroma and ECM to enhance drug delivery. Equally, reprogramming of the immune TME to enable ICB or recruitment and signaling of distinct immune cell populations holds promising possibilities for therapeutic approaches.

Immunotherapies, particularly ICB, have transformed cancer therapy in many solid cancer types but showed disappointing results in the context of PDAC. This can be explained by the dysfunctional T cell compartment and the high accumulation of immunosuppressive myeloid populations. As stated above, PDAC is almost entirely refractory to ICB targeting PD-1/PD-L1 or CTLA-4 either in a monotherapy or as combination (Bear et al., 2020; Brahmer et al., 2012; O'Reilly et al., 2019; Royal et al., 2010). Therefore, therapeutic approaches targeting or reprogramming the immunosuppressive myeloid compartment can potentially result in susceptibility of PDAC to ICB therapies and prolonged T cell responses. Among myeloid cells, several targetable options have emerged, namely TAMs and MDSCs. Particularly, targeting of receptor-ligand interactions to inhibit recruitment as well as targeting signaling pathways, epigenetic regulation, metabolism or angiogenesis to modulate the immunosuppressive myeloid phenotype to an antitumor phenotype present as reasonable treatment strategies (Bear et al., 2020; Goswami et al., 2022; Pathria et al., 2019). However, tackling the CAF compartment mainly failed in preclinical and clinical studies so far. For example, the approach to deplete aSMA$^+$ myoCAFs in a mouse model resulted in poorly differentiated tumors and shortened survival of mice (Özdemir et al., 2014). This highlights the importance to thoroughly study functional phenotypes of TME cell types, thus enabling to stratify immune cell types according to tumor promoting or restricting properties.

Future approaches to effectively target the TME need to account for the broad cellular diversity in PDAC, with the imperative to identify targets or combinatorial approaches aiming to reverse the immunosuppressive phenotype.

1.4. Mouse models of pancreatic cancer

Mouse models are a valuable preclinical model system in cancer research to systematically dissect multiple aspects of tumor biology *in vivo.* Among these, effects of genetic alterations on tumor initiation and progression, the interplay between tumor cells and the surrounding microenvironment and efficacy of novel therapies can be studied. Importantly, the development of PDAC GEMMs allowed the recapitulation of the human disease along with its extensive genetic heterogeneity and diverse TME landscape. Mutations in *KRAS,* particularly the *G12D* hotspot mutation, are the most predominant oncogenic driver mutations in >90 % of PDAC patients. Correspondingly, intercross of the *Kras*$^{LSL\text{-}G12D}$ allele and a pancreas-specific Cre-recombinase, either a transgenic *Pdx1-Cre* or knock-in *Ptf1a*^{Cre} line, resulted in the first reliable PDAC model mimicking the step-wise tumor progression, histopathology and metastatic dissemination of the human context (Hingorani et al., 2003; Jackson et al., 2001). In this model, endogenous *Kras*^{G12D} expression is silenced by a *LSL*-cassette *(LoxP-stop-LoxP),* consisting of two *LoxP* sites flanking a transcriptional STOP element. This construct was introduced upstream of exon 2 in the *Kras* locus. Upon Cre-mediated recombination, the STOP cassette and one *LoxP* site are excised, resulting in *Kras*^{G12D} expression specifically in the pancreas (Hingorani et al., 2003). To understand the influence of specific genetic alterations on PDAC tumorigenesis, the *Kras*$^{LSL\text{-}G12D}$ was combined with inactivation of other alleles, such as the main tumor suppressors *Trp53*$^{R172H/+}$ (mutated) or *Trp53*$^{flox/flox}$ (knock-out), *Cdkn2a*$^{flox/flox}$, *Smad4*$^{flox/flox}$ or *Tgfbr2*$^{flox/flox}$ (Ijichi et al., 2006; Krimpenfort et al., 2001; Marino et al., 2000; Olive et al., 2004; Yang et al., 2002). Within the last decade, next-generation PDAC models were generated which combine the *Cre/LoxP* and *Flp/frt* recombination systems, thereby allowing sequential genetic manipulation or targeting of TME cell types in a time-dependent manner. These dual-recombinase models enhance the possibilities of conventional PDAC GEMMs (Schönhuber et al., 2014).

In addition to endogenous GEMMs, mouse orthotopic allografts present another valuable model system in PDAC research. Orthotopic transplantations of murine PDAC cells, with known molecular and histological features, present a reproducible, cost-effective system to investigate tumor-host interaction and treatment studies *in vivo.*

1.5. Single cell RNA-sequencing analyses in PDAC

Single cell profiling of tumors, particularly scRNA-seq analyses, has significantly contributed to our understanding of the genetic and TME heterogeneity in the last decade. Compared to conventional bulk RNA-seq analysis, scRNA-seq can profile samples at a high-resolution, thereby interrogating gene expression profiles of individual cells. In contrast, bulk RNA-seq assesses the average gene expression of a cell population. As a drawback, scRNA-seq analyses come at a higher cost and data sets are more complex to analyze compared to bulk RNA-seq approaches. Droplet-based microfluidic approaches to encapsulate thousands of single cells in parallel are widely applied to assess the transcriptional profiles and phenotypes of diverse cell types (Baslan and Hicks, 2017; Giladi and Amit, 2018; Sun et al., 2021). In short, droplet-based scRNA-seq experimental workflows consist as a first step of the generation of a single-cell suspension by dissociating the desired tissue. Next, single cells are encapsulated in droplets containing barcoded beads which will add a unique nucleotide sequence (i.e. a molecular barcode) to the transcriptome of each cell using a microfluidics system. The input of cells in a high dilution ensures that only single cells are captured in droplets, rendering the majority of droplets empty. Within each droplet that encapsulated a cell, lysis is performed and the released mRNA is captured. Each transcript is additionally barcoded by a unique molecular identifier (UMI), which allows to distinguish between different transcripts from the same gene, plus a common cell barcode to distinguish different cells. Next, the mRNA is reversely transcribed to cDNA, followed by cDNA amplification. Then, sequencing libraries are constructed by enriching 3' ends of the cDNA and adding indices and adapters to the amplified fragments which can then be subjected to sequencing. The obtained reads can be analyzed by numerous computational toolkits to identify cell types and investigate cell states, gene expression dynamics, trajectories and cellular interactions (Luecken and Theis, 2019).

Multiple studies in PDAC research applied scRNA-seq analyses to investigate heterogeneity of the tumor cell compartment by identification of novel intermediate PDAC subtypes and their phenotypes. Moreover, immune cell subsets, e.g. a specific population of *Arg1*$^+$ *Trem2*$^+$ immunosuppressive macrophages, and CAF subpopulations, such as immunosuppressive apCAFs, were recently identified through scRNA-seq analysis (Elyada et al., 2019; Han et al., 2021; Katzenelenbogen et al., 2020; Raghavan et al., 2021).

In addition to analyzing the transcriptional states of cells, scRNA-seq data can be deployed to infer cell-cell interactions within tumors and thereby enable prediction of communication patterns between distinct cell types. To this end, the gene expression of ligand-receptor interaction pairs is analyzed between cell types and computationally predicted based on statistical methods from *a priori* knowledge about ligands and cognate receptors. Consequently, for predicting interactions between cell types, curated databases of ligand-receptor pairs can be interrogated. Inferred cell-cell communication networks build a basis for experimental validation of cell-cell interactions and aid to understand complex processes in the TME, for example how immunosuppression towards T cell is mediated (Armingol et al., 2021). As an example, Steele et al analyzed the interactions originating from macrophages, granulocytes, dendritic cells, endothelial cells and epithelial cells towards CD4, CD8 and NK cells using a ligand-receptor interaction prediction algorithm in a human PDAC scRNA-seq data set. Immune checkpoint ligands were highly expressed on myeloid cells and were predicted to signal to T and NK cells. Among those upregulated immune checkpoints were *ICOS/ICOSLG, SIRPA/CD47* and *TIGIT/PVR,* all identified as communication axis between macrophages and T cells/NK cells (Steele et al., 2020). This instance presents implications for immunotherapy and shows one possibility to dissect the PDAC TME cell-cell communication networks.

1.6. Objective

PDAC remains one of the most lethal cancer entities with a poor prognosis and a rising incidence. Recent studies described the extensive heterogeneity of the genetic landscape and the immunosuppressive TME in PDAC using single cell technologies. Although sequencing studies stratified PDAC into molecular subtypes, it remains elusive how the subtype-specific TME is composed and what drives immunosuppression in these states. To this end, the following questions need to be addressed: (i) Are molecular PDAC subtypes differing in their TME composition? (ii) What are the drivers of immunosuppressive immune cell recruitment in distinct subtypes? (iii) Is immunosuppression mediated via a direct interaction between tumor cells and T cells or via immune cell interactions?

The aim of this study is to conduct a comprehensive characterization of the TME composition in molecular PDAC subtypes using well-characterized GEMMs and orthotopic transplantation models of PDAC and to stratify them according to their TME state. Furthermore, we aim to infer the subtype-specific cell-cell communication networks to identify mechanisms of tumor-immune and immune-immune crosstalk, ultimately indicative of potential vulnerabilities for more effective therapeutic targeting of PDAC. To conduct this study systematically, we use a multimodal approach, ranging from bulk to single cell level, integrating histopathological analysis, flow cytometry, scRNA-seq, spatial transcriptomics and MS-based secretome analysis.

2. MATERIALS

This section contains all materials which I used myself to conduct experiments and analysis. Materials for methods which were performed by collaboration partners are not included.

2.1. Cell lines

All mouse PDAC cell lines were previously generated in the groups of Prof. Dieter Saur and Prof. Günter Schneider. The following cell lines were characterized and subtype stratified in the publication of Müller et al in close collaboration with Prof. Roland Rads group (Mueller et al., 2018).

Cell line ID	*Description*	*Subtype*
5671	Mouse PDAC	Classical – C2a
16990	Mouse PDAC	Classical – C2a
53578	Mouse PDAC	Classical – C2a
5748	Mouse PDAC	Classical – C2a
8182	Mouse PDAC	Classical – C2a
B590	Mouse PDAC	Classical – C2b
53631	Mouse PDAC	Classical – C2b
53646	Mouse PDAC	Classical – C2b
8442	Mouse PDAC	Classical – C2b
8661	Mouse PDAC	Classical – C2b
2259	Mouse PDAC	Classical – C2b
9591	Mouse PDAC	Classical – C2b
53704	Mouse PDAC	Classical – C2c
4900	Mouse PDAC	Classical – C2c
8296	Mouse PDAC	Classical – C2c
S821	Mouse PDAC	Classical – C2c
4706	Mouse PDAC	Classical – C2c
6075	Mouse PDAC	Classical – C2c
8028	Mouse PDAC	Mesenchymal – C1
8570	Mouse PDAC	Mesenchymal – C1
16992	Mouse PDAC	Mesenchymal – C1
9091	Mouse PDAC	Mesenchymal – C1
5320	Mouse PDAC	Mesenchymal – C1
8513	Mouse PDAC	Mesenchymal – C1
8349	Mouse PDAC	Mesenchymal – C1
3202	Mouse PDAC	Mesenchymal – C1

2.2. Cell culture medium and reagents

Product	*Manufacturer*
Acetic acid	Sigma
AMPure XP	Beckman Coulter
Bluing Buffer, Dako	Agilent
DMEM high glucose	Sigma
Eosin Y Solution, 0,5 %	Sigma

Ethanol (100 %)	Merck
Ethanol (80 %)	BrüggemannAlcohol
Fetal calve serum (FCS)	Sigma
Glycerol	Sigma
Hematoxylin, Mayer’s (Lilie’s Modification)	Agilent
Hydrochloric Acid Solution, 0.1N	Thermo Fisher
KAPA SYBR FAST qPCR Master Mix (2X)	KAPA Biosystems
Low TE Buffer (10 mN Tris-HCl pH 8.0, 0.1 mM EDTA)	Thermo Fisher
Methanol, for HPLC	Sigma
Penicillin (10,000 units/mL)/Streptomycin (10,000 µg/mL)	Invitrogen GmbH
Phosphate buffered saline (PBS)	Sigma
RNAse inhibitor, mouse	NEB
SSC Buffer 20X Concentrate	Sigma
SDS solution, 10% in water	Sigma
Tissue-Tek O.C.T compound	Sakura Finetek
Qiagen Buffer EB	Qiagen

2.3. Kits

Product	*Catalog number*	*Manufacturer*
Tumor dissocation kit, mouse	#130-096-730	Miltenyi Biotec
Debris removal kit, mouse	#130-109-398	Miltenyi Biotec
Dead cell removal kit, mouse	#130-090-101	Miltenyi Biotec
Chromium Next GEM Single Cell 3’ GEM, Library & Gel Bead Kit v3.1, 16 rxns	#1000121	10x Genomics
Chromium Next GEM Chip G Single Kit, 48 rxns	#1000120	10x Genomics
Chromium Single Cell 3’ GEM, Library & Gel Bead Kit v3, 4 rxns	#1000092	10x Genomics
Chromium Chip B Single Cell Kit, 16 rxns	#1000074	10x Genomics
Chromium i7 Multiplex Kit, 96 rxns	#120262	10x Genomics
Visium Spatial Tissue Optimization Reagent Kit, 4 slides	#1000192	10x Genomics
Visium Spatial Tissue Optimization Slide Kit	#1000191	10x Genomics
Visium Spatial Gene Expression Reagent Kit, 16 rxns	#1000186	10x Genomics
Library Construction Kit, 16 rxns	#1000190	10x Genomics
Dual Index Plate TT Set A	#3000431	10x Genomics
Agilent High Sensitivity DNA Kit	#5067-4626	Agilent
Zombie Aqua Fixable Viability Kit	#423102	Biolegend

2.4. Antibodies

Specificity	*Cat.number/RRID*	*Manufacturer*	*Application*
CD4 BUV805 (Clone GK1.5)	Cat #564922; RRID:AB_2739008	BD Biosciences	FACS: 1:100
CD3ε BUV395 (Clone 145-2C11)	Cat #563565, RRID:AB_2738278	BD Biosciences	FACS: 1:20
CD11c BUV737 (Clone HL3)	Cat #564986, RRID:AB_2739034	BD Biosciences	FACS: 1:30
NK1.1 BUV395 (Clone PK136)	Cat #564144, RRID:AB_2738618	BD Biosciences	FACS: 1:25
Siglec-F BB515	Cat #564514, RRID:AB_2738833	BD Biosciences	FACS: 1:100
CD8a BV785 (Clone 53-6.7)	Cat #100749, RRID:AB_11218801	Biolegend	FACS: 1:100
CD45 PerCP Cy5.5 (Clone I3/2.3)	Cat #147705, RRID:AB_2563537	Biolegend	FACS: 1:100

CD19 FITC (Clone 6D5)	Cat #115505, RRID:AB_313640	Biolegend	FACS: 1:100
EpCAM APC/AF647 (Clone G8.8)	Cat #118212, RRID:AB_1134101	Biolegend	FACS: 1:200
Ly6C BV785 (Clone HK1.4)	Cat #128041, RRID:AB_2565852	Biolegend	FACS: 1:200
CD11b BV650 (Clone M1/70)	Cat #101239, RRID:AB_11125575	Biolegend	FACS; 1:100
F4/80 BV421/PB (Clone BM8)	Cat #123131, RRID:AB_10901171	Biolegend	FACS: 1:30
Ly6G PE (Clone 1A8)	Cat #127607, RRID:AB_1186104	Biolegend	FACS: 1:200
CD68 APC-CY7 (Clone FA-11)	Cat #137023, RRID:AB_2616812	Biolegend	FACS: 1:20
CD25 BV650 (Clone PC61)	Cat #102038, RRID:AB_2563060	Biolegend	FACS: 1:50
TCR γ/δ BV421 (Clone GL3)	Cat #118120, RRID:AB_2562566	Biolegend	FACS: 1:50
CD62L PE (Clone MEL-14)	Cat #104408, RRID:AB_313095	Biolegend	FACS: 1:500
CD44 APC/Fire750 (Clone IM7)	Cat #103062, RRID:AB_2616727	Biolegend	FACS: 1:30
TruStain FcX CD16/32 (Clone 93)	Cat #101320, RRID:AB_1574975	Biolegend	FACS; 1:100
TER-119/Erythroid Cells BV421	Cat #116233, RRID:AB_10933426	Biolegend	FACS; 1:100
CD45 APC/AF647 (Clone 30-F11)	Cat #103124, RRID:AB_493533	Biolegend	FACS: 1:20
CD31 APC/AF647 (Clone 390)	Cat #102416, RRID:AB_493410	Biolegend	FACS: 1:20

2.5. Software and databases

Software	*URL/manufacturer*	*Reference*
BayesSpace (v1.5.1)	https://github.com/edward130603/BayesSpace	(Zhao et al., 2021)
BBKNN	https://github.com/Teichlab/bbknn	(Polański et al., 2020)
bioinfokit visuz (v2.0.8)	https://github.com/reneshbedre/bioinfokit	n/a
CellChat (v1.0.0)	https://github.com/sqjin/CellChat	(Jin et al., 2021)
CellRanger (v3.1.0)	https://support.10xgenomics.com/single-cell-gene-expression/software (10x Genomics)	n/a
Corrplot (v0.9.2)	https://github.com/taiyun/corrplot	n/a
FlowJo (v10.8.1)	FlowJo LLC, Ashland, OR, USA	n/a
GraphPad Prism (v8)	GraphPad Software, Inc.	n/a
GSEApy (v0.10.8)	https://github.com/zqfang/GSEApy	n/a
ImageScope (v12.3)	Leica Biosystems, Wetzlar	n/a
Leiden (v0.8.1)	https://github.com/vtraag/leidenalg	(Traag et al., 2019)
MaxQuant3 (v1.6.2.10)	https://www.maxquant.org	(Cox and Mann, 2008b)
R (v4.0.3)	https://www.R-project.org (R Core Team, 2016)	n/a
Python (v3.8.3)	https://www.python.org (Python Software)	n/a
Scanpy (v1.8.1)	https://github.com/theislab/scanpy	(Wolf et al., 2018)
Seurat (v4.0.6)	https://satijalab.org/seurat	(Hao et al., 2021)
Squidpy (v1.0.0)	https://github.com/scverse/squidpy	(Palla et al., 2022)
SpaceRanger (v.1.10)	https://support.10xgenomics.com/spatial-gene-expression/software (10x Genomics)	n/a
UMAP (v0.4.6)	https://github.com/lmcinnes/umap	(Becht et al., 2018)

3. METHODS

3.1. Mouse strains and animal experiments

All animal studies were conducted in compliance with the European guidelines for the care and use of laboratory animals and ARRIVE. All studies were approved by the Institutional Animal Care and Use Committees (IACUC) of the local authorities of Technische Universität München and the Regierung von Oberbayern. Mice were housed in a vivarium facility, with a light-dark cycle on 12:12 hours, a constant housing temperature between 20 and 24°C and a relative air humidity of 55%. The following mouse strains were included in this study:

Allele name	***Mouse strain***	***Reference***
Ptf1a$^{Cre/+}$	Ptf1atm1(cre)Hnak	(Nakhai et al., 2007)
Pdx1-Flp	Tg(Pdx1-flpo)#Dsa	(Schönhuber et al., 2014)
LSL-Kras$^{G12D/+}$	Krastm4Tyj	(Hingorani et al., 2003; Jackson et al., 2001)
FSF-Kras$^{G12D/+}$	Krastm1Dsa	(Schönhuber et al., 2014)
FSF-R26$^{CAG-CreERT2/+}$	Gt(ROSA)26Sortm4(CAG-Cre/ERT2)Dsa/J	(Schönhuber et al., 2014)
LSL-Trp53$^{R172H/+}$	B6.129S4(Cg)-*Trp53*$^{tm2.1Tyj}$/J	(Olive et al., 2004)
Trp53$^{lox/+}$	B6.129P2-*Trp53*^{tm1Brn}/J	(Marino et al., 2000)
Trp53$^{frt/+}$	Trp53tm1.1Dgk	(Lee et al., 2012)
p16$^{Ink4a*/+}$	Cdkn2atm1Rdp	(Krimpenfort et al., 2001)
Tgfbr2$^{flox/+}$	Tgfbr2tm1.2Hlm	(Chytil et al., 2002; Ijichi et al., 2006)
LSL-R26$^{Snail/+}$	n/a	(Paul, 2013)
LSL-R26$^{Tgfb1/+}$	Gt(ROSA)26Sortm3(TGFb1)/J	(Hieber, 2021)
Smad4$^{flox/+}$	Smad4$^{tm2.1Cxd}$	(Yang et al., 2002)
LSL-Pik3ca$^{H1047R/+}$	Gt(ROSA)26Sortm2(Pik3ca*)Dsa	(Eser et al., 2013)

The following genotype groups were investigated in this study:

Genotype group	***Allele combination***
PK	*Ptf1a*$^{Cre/+}$*,LSL-Kras*$^{G12D/+}$*; Pdx1-Flp, FSF-Kras*$^{G12D/+}$
PKC	*Ptf1a*$^{Cre/+}$*,LSL-Kras*$^{G12D/+}$*; p16*$^{Ink4a*/+}$*, Ptf1a*$^{Cre/+}$*,LSL-Kras*$^{G12D/+}$*; p16*$^{Ink4a*\ Ink4a*}$
PKP	*Ptf1a*$^{Cre/+}$*,LSL-Kras*$^{G12D/+}$*,LSL-Trp53*$^{R172H/+}$*; Ptf1a*$^{Cre/+}$*,LSL-Kras*$^{G12D/+}$*, Trp53*$^{lox/+}$*; Pdx1-Flp, FSF-Kras*$^{G12D/+}$*,Trp53*$^{frt/+}$*; Ptf1a*$^{Cre/+}$*,LSL-Kras*$^{G12D/+}$*,LSL-Trp53*$^{R172H/R172H}$*; Ptf1a*$^{Cre/+}$*,LSL-Kras*$^{G12D/+}$*, Trp53*$^{lox/lox}$*; Pdx1-Flp, FSF-Kras*$^{G12D/+}$*,Trp53*$^{frt/frt}$
PKS	*Ptf1a*$^{Cre/+}$*,LSL-Kras*$^{G12D/+}$*,LSL-R26*$^{Snail/+}$
PKSC	*Ptf1a*$^{Cre/+}$*,LSL-Kras*$^{G12D/+}$*,LSL-R26*$^{Snail/+}$*,p16*$^{Ink4a*/+}$
PKPS	*Ptf1a*$^{Cre/+}$*,LSL-Kras*$^{G12D/+}$*,LSL-Trp53*$^{R172H/+}$*,LSL-R26*$^{Snail/+}$
PKT	*Ptf1a*$^{Cre/+}$*,LSL-Kras*$^{G12D/+}$*,Tgfbr2*$^{flox/+}$*; Ptf1a*$^{Cre/+}$*,LSL-Kras*$^{G12D/+}$*,Tgfbr2*$^{floxflox+}$
PKPT	*Ptf1a*$^{Cre/+}$*,LSL-Kras*$^{G12D/+}$*, LSL-Trp53*$^{R172H/+}$*,Tgfbr2*$^{flox/+}$
PKTo	*Ptf1a*$^{Cre/+}$*,LSL-Kras*$^{G12D/+}$*, LSL-R26*$^{Tgfb1/+}$
PKPCSm	*Pdx1-Flp, FSF-Kras*$^{G12D/+}$*, FSF-R26*$^{CAG-CreERT2/+}$*,Trp53*$^{lox/+}$*, p16*$^{Ink4a*/+}$*,Smad4*$^{flox/+}$*; Pdx1-Flp, FSF-Kras*$^{G12D/+}$*, FSF-R26*$^{CAG-CreERT2/+}$*,Trp53*$^{lox/lox}$*, p16*$^{Ink4a*/\ Ink4a*}$*,Smad4*$^{flox/flox}$
PPI3K	*Ptf1a*$^{Cre/+}$*,LSL-Pik3ca*$^{H1047R/+}$
PPI3KP	*Ptf1a*$^{Cre/+}$*,LSL-Pik3ca*$^{H1047R/+}$*,LSL-Trp53*$^{R172H/+}$*; Ptf1a*$^{Cre/+}$*,LSL-Pik3ca*$^{H1047R/+}$*,LSL-Trp53*$^{R172H/R172H}$

3.2. Orthotopic implantation of mouse PDAC cell lines

For orthotopic transplantation of PK mouse PDAC cell lines, cancer cells (2500 to 10000 cells) were orthotopically injected into the pancreas tail of syngeneic immunocompetent C57Bl/6J animals. Mouse cell cultures for implantation were sex-matched as well as matched to the genetic background of the host animal to avoid graft rejection and immunogenicity. Orthotopic implantations were performed together with Chiara Falcomatà, Jack Barton and Saskia Ettl.

3.3. Cell culture of mouse PDAC cell lines

Cell culture experiments were performed in biosafety cabinets under sterile conditions. Previously generated mouse PDAC cell lines were cultured in DMEM supplemented with 10% FCS and 1% Penicillin/Streptomycin unless otherwise stated. Cell cultures were kept in incubators at 37°C and 5% CO_2 condition. All cell lines were routinely tested for mycoplasma contaminations by using an in-house PCR test as well as previously confirmed for their genotype by PCR (Mueller et al., 2018).

3.4. Histopathological analysis of PDAC samples

Collection and H&E staining of the PDAC histology cohort (n=500 tumors) was performed mainly by Dr. Chen Zhao (Zhao, 2021) and former lab members of the Saur group. The histopathological analysis was conducted by board-certified pathologist Prof. Moritz Jesinghaus and documented by Dr. Chen Zhao (Zhao, 2021). Stroma content, granulocyte and lymphocyte infiltration were estimated as percentage of the tissue area from the H&E-stained tumor sections and up to 2 replicates per individual tumor were analyzed. Mitoses were counted per high power-field in areas showing increased mitotic activity. Unsupervised clustering analysis of the data set was performed by Chiara Falcomatà.

3.5. Immunophenotyping by flow cytometry

Freshly harvested tumor samples were minced and enzymatically digested with the tumor dissociation kit (Miltenyi Biotec) for 40 min at 37°C with agitation. The cell suspension was strained through a 100 µm strainer, spun down and resuspended in 2% FCS/PBS. Cells were blocked for 10 min on ice with anti-mouse CD16/CD32 FC block (Biolegend, 1:100) and stained with Zombie Aqua Fixable Viability Kit (Biolegend, 1:500) and the following antibody cocktails: CD4 BUV805 (BD, 1:100), CD3εBUV395 (BD, 1:20), CD8a BV785 (Biolegend, 1:100), CD45 PerCP Cy5.5 (Biolegend, 1:100), CD19 FITC (Biolegend, 1:100), EpCAM APC/AF647 (Biolegend, 1:200) for acquisition of adaptive immune cells; CD11c BUV737 (BD, 1:30), NK1.1 BUV395 (BD, 1:25), Ly6C BV785 (Biolegend, 1:200), CD11b BV650 (Biolegend, 1:100), F4/80 BV421/PB (Biolegend, 1:30), CD45 PerCP Cy5.5 (Biolegend, 1:100), Ly6G PE (Biolegend, 1:200), CD68 APC-CY7 (Biolegend, 1:20), EpCAM APC/AF647 (Biolegend, 1:200) for acquisition of innate immune cells. Per panel 1,000,000 events were acquired on the BD LSRFortessa. Flow cytometry data was analyzed using FlowJo software (v10.6.2). Flow cytometry experiments were performed together with Chiara Falcomatà and Jack Barton. Spearman's rank cell type correlation analysis resulting from flow cytometry data in classical and mesenchymal implanted tumors was performed by Chiara Falcomatà using the corrplot toolkit.

3.6. scRNA-seq experiments and computational analysis

3.6.1. Tissue dissociation and sample preparation

Dissociation and sample preparation was conducted as described in Falcomatà et al.: “Tumor specimens were dissociated and enzymatically digested with the tumor dissociation kit as described above. The cell suspension was strained through a 100 µm strainer, spun down and resuspended in 2% FCS/PBS including RNase inhibitor (1:100). Debris removal solution (Miltenyi Biotec) was used to remove cell debris from the dissociated tissue. Then, a dead cell removal kit (Miltenyi Biotec) was used to enrich for living cells. For specific samples, the cell suspension was spun down, resuspended in PBS and blocked for non-antigen-specific binding for 10 min on ice with anti-mouse CD16/CD32 FC block (Biolegend, 1:100). Cells were stained with the following antibodies for FACS sorting: TER-119 BV421 (Biolegend, 1:100), CD45-AF647 (Biolegend, 1:20), CD31-AF647 (Biolegend, 1:20) and EPCAM-AF647 (Biolegend, 1:20) for 30 min on ice. Cell sorting was performed using the BD FACS Aria Fusion. The sorted cells from the TER-119-negative/CD45-/CD31-/EPCAM-positive fraction (for enrichment of immune, endothelial and epithelial tumor cells and exclusion of erythrocytes) as well as TER-119-/CD45-/CD31-/EPCAM-negative fraction (for enrichment of fibroblasts/mesenchymal tumor cells and exclusion of erythrocytes) were collected in 2% FCS/PBS.” (Falcomatà et al., 2022). Sample preparation was performed together with Chiara Falcomatà.

3.6.2. Library preparation and sequencing

Library preparation and sequencing was performed as described in Falcomatà et al.: “The (sorted) cells were counted, diluted to an appropriate cell number in 2% FCS/PBS and loaded on a 10x Chromium chip (up to 20,000 cells per lane) to generate gel beads in emulsion (GEMs). Single cell GEM generation, barcoding and library construction was performed by using 10x Chromium Single Cell 3’ v3 and v3.1 chemistry according to the manufacturer’s instructions. cDNA and generated libraries were examined for library size and quality on an Agilent Bioanalyzer 2100 using HS DNA Kit (Agilent). Libraries were sequenced on Illumina NovaSeq 6000 S2 (PE, 28+94 bp) and NovaSeq 6000 S4 (PE, 100 bp).” (Falcomatà et al., 2022). Albulena Toska helped with generating the scRNA-seq libraries.

3.6.3. Pre-processing of data, integration and quality control

Pre-processing, data integration and quality control was performed as described in Falcomatà et al.: Alignment of the scRNA-seq data to the mouse reference genome (mm10, release 108.20200622), filtering, barcode and unique molecular identifier (UMI) counting was performed using the 10x Genomics Cell Ranger software (v3.1.0). Python (v3.8.3) and the Python software package Scanpy was employed for all further analyses (v1.8.1) (Wolf et al., 2018). Cells that expressed less than 200 genes, had less than 1000 or more than 20000 counts or had more than 10% mitochondrial gene counts were excluded from the analysis. In addition, genes with less than 20 counts were filtered out. Counts were per-cell normalized and (log+1)-transformed. Highly variable genes were computed using the first n=4000 most variable genes for the analyses across all cell types. Batch-effect correction was performed using BBKNN (batch balanced k nearest neighbors, v1.5.1) (Polański et al., 2020)." (Falcomatà et al., 2022). Initial data analysis was supported by Jonas Mir and Albulena Toska.

3.6.4. Dimensionality reduction, clustering and cell type annotation

Dimensionality reduction, clustering and cell type annotation was performed as described in Falcomatà et al.: "The Leiden algorithm (v0.8.1) (Traag et al., 2019) was used for cell clustering and Uniform Manifold Approximation and Projection (UMAP, v0.4.6) (Becht et al., 2019) for dimensionality reduction. The clusters were further annotated by assessment of known cell-type specific markers. Principal component analysis was performed with default parameters. Neighborhood graphs were computed based on n=10 principal components and k=30 neighbors and the calculation of all UMAP projections was based on default parameters. The optimal number of Leiden clusters was adjusted according to the sample of consideration." (Falcomatà et al., 2022).

3.6.5. Macrophage cluster analysis

Macrophages were initially identified by expression of *Cd68* and *Lyz2,* extracted from the quality-controlled data set and further normalized as well as batch corrected as described above using the same parameters (total 8,145 cells). Macrophage and monocyte subpopulations were assessed by using different reference data sets (Kemp et al., 2021b; Zhang et al., 2020; Zilionis et al., 2019). Differential gene expression analysis between macrophages/monocytes from mesenchymal and classical tumors was performed by using Wilcoxon rank-sum test. Then, genes were ranked (log2fc_min=0.5, pval_cutoff=0.01) and gene set enrichment analysis was performed using the 'MSigDB_Hallmark_2020' gene set with the GSEApy toolkit.

3.6.6. Neutrophil cluster analysis

Neutrophils were identified by expression of *S100a8/S100a9* and *Cxcr2,* extracted from the quality-controlled data set and further normalized and batch corrected as described above using the same parameters (total 3,017 cells). To assess phenotypic characteristics, the expression of 'PMN-MDSC' and 'activated PMN-MDSC' gene sets were analyzed (Veglia et al., 2021a).

3.6.7. T cell cluster analysis

Cd3g expressing cells were extracted from the quality-controlled data set for T cell analysis and further normalized and batch corrected as described above using the same parameters (total

20,055 cells). T cell subpopulations were annotated as previously described (Falcomatà et al., 2021).

3.6.8. Tumor cell cluster analysis

Tumor cells (*Krt19, Krt18* expression) were extracted from the quality-controlled data set and further normalized and batch corrected as described above using the same parameters (total 11,953 cells). Differential gene expression analysis between tumor cells from mesenchymal and classical tumors was performed by using Wilcoxon rank-sum test.

3.6.9. CAF cluster analysis

CAF cells, expressing high levels of *Pdpn*, *Dcn* and showing no expression of *Krt19/Krt18*, were extracted from the quality-controlled data set and further normalized and batch corrected as described above using the same parameters (total 1,414 cells). CAF subpopulations were annotated by previously published using marker gene sets (Elyada et al., 2019).

3.7. CellChat ligand-receptor interaction analysis

CellChat was used to infer cell-cell communication between immune cell subpopulations as well as between tumor cells and immune cells *in vivo* by integration of scRNA-seq data of orthotopically implanted PK tumors (Jin et al., 2021). As input for the CellChat analysis, normalized scRNA-seq data with assigned cell type labels was used and converted to a CellChat object (Jin et al., 2021). Next, relevant CellChatDB (database), either 'secreted signaling' or 'cell-cell contact', was chosen. Overexpression of ligand or receptors belonging to either database in a cell type were identified as well as ligand-receptor interactions between cell types if either ligand or receptor was overexpressed in a cell type. CellChat calculates a communication probability value for each ligand-receptor interaction and performs a permutation test. The probability value of the interaction is assigned by integration of gene expression and prior knowledge of ligand-receptor pair interactions using law of mass action. For calculating the average gene expression per cell type, we set the 'trimean' function to 10% truncated mean.

CellChat objects were separately processed for the classical and mesenchymal scRNA-seq data set. For direct comparison of the two subtypes, both CellChat objects were merged into one combined CellChat object. CellChat then compared the number of identified ligand-receptor interactions and interaction strength across different cell types. Thereby, enhanced or decreased interaction patterns/signaling pathways can be identified between the classical and mesenchymal subtype. First, the 'secreted signaling' CellChatDB was used for assessing the interactions between tumor cells and TME cell types as well as between Macrophages – T cells and Neutrophils – T cells. Additionally, the 'cell-cell contact' CellChatDB was interrogated to infer interactions between Macrophages – T cells and Neutrophils – T cells.

3.8. Spatial transcriptomics experiments and computational analysis

3.8.1. Sample acquisition, tissue optimization and Visium spatial gene expression library preparation and sequencing

Fresh frozen tumor samples were stored in OCT and sectioned at 10 µm using a cryotome (Leica), followed by careful placement on the capture areas (6,5 x 6,5 mm) of the Visium Tissue Optimization Slide (10x Genomics) and Visium Gene Expression Slide (10x Genomics). First, the tissue optimization workflow was performed to identify the optimal permeabilization time for each individual tumor. The Visium Spatial Gene Expression workflow was performed according to the manufacturer’s instructions. Next, cDNA and generated libraries were examined for sample size and quality on an Agilent Bioanalyzer 2100 using HS DNA Kit (Agilent). Libraries were sequenced on Illumina NovaSeq 6000 S1 (PE, 100 bp) with minimum 50,000 read pairs per tissue covered spot on the capture area. Sectioning of fresh frozen samples onto Visium slides was performed by Olga Seelbach (Katja Steiger group).

3.8.2. Pre-processing of data and quality control

Alignment and initial data analysis was performed by Giovanni Palla (Fabian Theis Lab) in close collaboration. The raw sequencing reads of the spatial transcriptomics data were quality checked and aligned to the mouse reference genome (mm10, release 108.20200622) using Space Ranger (v1.10). The resulting gene-spot matrices were further analyzed with the Squidpy (v1.0.0) toolkit in Python (Palla et al., 2022). Spots were filtered for a minimum expression of 200 genes, minimum read counts of 5000 and maximum read count number of 35,000 counts. Spots with more than 10% mitochondrial gene counts were excluded from the analysis. In addition, genes with fewer than 10 read counts were removed. Counts were per-spot normalized and (log+1)-transformed. Highly variable genes were computed with the cellranger method in scanpy and the first n=2000 most variable genes were kept for downstream analysis (Wolf et al., 2018). Principal component analysis was performed with default parameters.

3.8.3. BayesSpace enhanced clustering and cluster annotation

To enhance the capture spot resolution of the Visium gene expression slide, we employed the BayesSpace toolkit, which subsets each capture spot into 6 subspots. First, number of clusters were selected based on the pseudo-log-likelihood by choosing the cluster number around the elbow of the plot. Spatial clustering implementing a Bayesian model with a Markov random field was performed using 10,000 iterations (nrep=10000). Next, the clustering was enhanced at the subspot level similar to the previous spot-level clustering using 100,000 iterations (nrep=100000). To enhance gene expression at the supspot-level, BayesSpace uses a fitted model to predict gene expression at high-resolution (Zhao et al., 2021). Visualizations of heatmaps were performed in Seurat.

3.9. Secretome analysis of tumor cell-derived conditioned media

Collection of conditioned media was performed together with Constantin Schmitt and Chiara Falcomatà. The MS-based secretomics experiment and data processing was performed by Jonathan Swietlik (Meissner group).

3.9.1. Conditioned media collection

Classical and mesenchymal PK cell lines were cultured in 10-cm dishes under standard conditions until 80-90% confluency was reached. Cells were washed thoroughly twice with PBS, once with serum/phenol-red-free DMEM and incubated for 12h in 5 ml serum/phenol-red-free DMEM. The conditioned media was collected, filtered through 0.2 µm pores, snap frozen and then further processed for MS-based secretomics analysis.

3.9.2. MS-based secretomics

MS-based secretome analysis was conducted as described in Falcomatà et al.: “Serum- and phenol red free PDAC cell conditioned media was concentrated to ~250 µl and washed with 50 mM Tris, pH 8 (Amicon Ultra 3 kDa cutoff filter units, Merck) at 4°C, 4,000 x g. 50 µl of concentrated supernatants were complemented with 10 mM TCEP and 40 mM 2-chloroacetamide and then heated in a thermoshaker for 10 minutes at 95°C, 1,000 rpm. Next, samples were digested with 1.5 µg trypsin/ LysC mix for 16 h at 37°C, 1000 rpm. Samples were acidified by adding 100 µl isopropanol, 1% TFA and desalted using in-house made SDB-RPS StageTips. Desalted peptide mixtures were reconstituted in buffer A (0.1% formic acid) and analyzed with an EASY-nLC 1200 ultrahigh-pressure system (Thermo Fisher Scientific) coupled to an Orbitrap Exploris 480 instrument (Thermo Fisher Scientific). 300 ng peptide were loaded onto a 50-cm in-house made column with 75 µm inner diameter, packed with C18 1.9 µm ReproSil beads (Dr. Maisch GmbH). Peptides were eluted with a linear gradient from 5% to 30% buffer B (0.1% formic acid, 80% acetonitrile) for 95 minutes at flow rate of 300 nl min-1. An in-house made column oven ensured a constant temperature at 60°C. Data acquisition was performed with a data-dependent MS/MS method. Full scans (300 to 1650 m/z, R = 60,000 at 200 m/z) at a normalized AGC target of 300% were followed by 15 MS/MS scans with higher energy collisional dissociation (normalized AGC target 100%, maximum injection time 28 ms, isolation window 1.4 m/z, HCD collision energy 30%, R = 15,000 at 200 m/z). Dynamic exclusion of 30 s was enabled.” (Falcomatà et al., 2022)

3.9.3. Data preprocessing

Data preprocessing was performed as described in Falcomatà et al.: “The Andromeda search engine built into MaxQuant3 (v1.6.2.10) (Cox and Mann, 2008a) was used to process MS raw files. Next, MS/MS spectra were matched against the mouse UniProt FASTA database (June 2019) with an FDR of 0.01 at the protein and peptide level and a minimum peptide length of seven amino acids. Match between runs was enabled and the minimal ratio count for label-free quantification was set to one. Proteins were filtered for extracellular annotation (GOCC terms "extracellular space" and "extracellular matrix", UniProt keywords "secreted"). Missing values were replaced from a Gaussian distribution (30 % width and downshift by 1.8 standard deviations of measured values) and t-tests were performed with a permutation-based FDR of 0.05." (Falcomatà et al., 2022). Differentially secreted proteins were visualized in a volcano plot using the bioinfokit visuz (v2.0.8) toolkit in Python. Then, proteins were ranked (log2fc_min=0.5, pval_cutoff=0.05) and gene set enrichment analysis was performed using the 'MSigDB_Hallmark_2020' and 'GO_Biological_Process_2021' gene sets with the GSEApy toolkit in Python

4. RESULTS

Context-specific oncogenic signaling across organs can differ substantially in various tissues, thus influencing tumorigenesis as well as treatment outcome and resistance (Falcomatà et al., 2019; Schneider et al., 2017). To dissect signaling downstream of oncogenic drivers in various tissues, we elucidated the role of context specific PI3K and Kras signaling for extrahepatic cholangiocarcinoma (ECC) and PDAC initiation in mouse models. We showed that oncogenic Pik3ca^{H1047R} activation leads to transformation of the biliary epithelium, while oncogenic Kras^{G12D} signaling initiates exclusively PDAC formation. Further molecular analysis revealed that the tumor suppressor p27^{Kip1} presents a barrier to ECC tumorigenesis. In conclusion, we generated the first GEMM for functional studies of ECC and identified PI3K signaling output strength and tumor suppressor function of p27^{Kip1} as integral determinants for ECC development. These results have been recently published in the research article "Genetic Screens Identify a Context-Specific PI3K/p27Kip1 Node Driving Extrahepatic Biliary Cancer ", Falcomatà, Bärthel, Ulrich et al. (Cancer Discovery. 2021 Dec 1;11(12):3158-3177.) (Falcomatà et al., 2021).

During this PhD work, we further focused on Kras^{G12D}-driven PDAC and investigated a novel combinatorial therapy approach in molecular PDAC subtypes. The combination consisting of the MEK inhibitor trametinib and the multi-kinase inhibitor nintedanib was specifically effective in the aggressive mesenchymal PDAC subtype. Moreover, the therapy reprogrammed the immunosuppressive TME in vivo by inducing T cell infiltration, which sensitized the mesenchymal subtype, but not the classical, to ICB by PD-L1 inhibition. This work was recently published in the research article "Selective multi-kinase inhibition sensitizes mesenchymal pancreatic cancer to immune checkpoint blockade by remodeling the tumor microenvironment ", Falcomatà, Bärthel et al. (Nature Cancer 2022 Mar;3(3):318-336.) (Falcomatà et al., 2022).

The striking difference in therapy response in both subtypes, particularly the effect on the TME, prompted us to investigate the TME characteristics of PDAC subtypes in a treatment-naïve state. The results of this comprehensive analysis are not published as research article to this date and are presented in this PhD dissertation in the next chapters. Contributions from colleagues and collaborators to the results presented in this work are indicated in the methods section and the figure legends.

The PDAC TME consists of various immune and stromal cell types presenting a heterocellular ecosystem, which aggravates the already difficult to dissect heterogeneity in the genetic landscape of this cancer entity. Given the previous classification of molecular PDAC subtypes (classical and mesenchymal) which defines tumor compartment-intrinsic characteristics, we hypothesized that the TME composition of the subtypes equally differs to a large extent (Collisson et al., 2019).

In the scope of this doctoral thesis, we conducted a comprehensive analysis of the PDAC subtype-specific TME to (i) characterize the TME architecture, focusing on immune infiltrates, (ii) analyze the tumor cell-mediated communication network between tumor- and immune cells and (iii) infer the aggregated immune-immune interaction network in classical and mesenchymal PDAC **(Figure 2a)**. We addressed these questions through an *in vivo* and *in vitro* multimodal approach by integration of single cell resolution methods, such as flow cytometry and scRNA-seq, with bulk resolution methods, e.g. large-scale histopathological analysis. Therefore, it is possible to analyze the subtype-specific TME attributes on multiple levels (e.g., population dynamics of immune cells as well as molecular features of subtype-specific infiltrates) **(Figure 2b)**.

The analysis was performed by leveraging a large cohort of mouse PDAC tumors, previously generated in the Saur group, and corresponding mouse PDAC cell cultures established thereof. Mouse models recapitulate the spectrum of human PDAC subtypes and are therefore a valuable model system to systematically study the TME characteristics in a treatment-naïve setting.

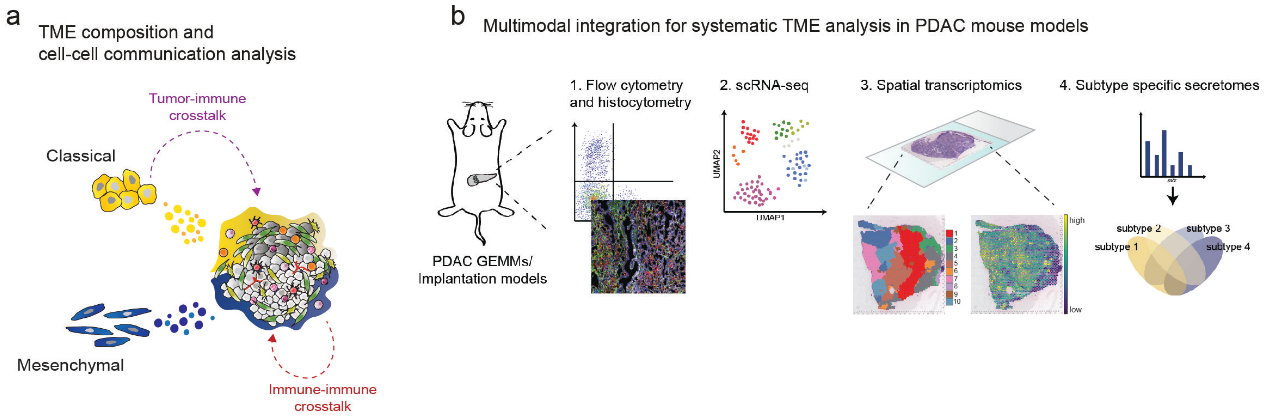

Figure 2. Overview of systematic TME characterization

a, Schematic depiction of analysis strategy for the subtype-specific TME in PDAC, focusing on a comprehensive characterization of the TME composition and analysis of cell-cell communication networks in classical and mesenchymal PDAC. Within the scope of this work, we focus on tumor-immune and immune-immune crosstalk.
b, Schematic overview of methods integrated in the TME characterization. Using mouse models of PDAC subtypes, the subtype-specific TME was analyzed by (1.) Flow cytometry and histocytometry, (2.) scRNA-seq analysis, (3.) spatial transcriptomics and (4.) MS-based secretomics.
Individual graphical elements and panel b by courtesy of Chiara Falcomatà.

4.1. Integrative histopathological analysis and single-cell profiling reveals TME heterogeneity across molecular PDAC subtypes

We first aimed to characterize the TME composition in mouse models of molecular PDAC subtypes defined by distinct genetic alterations. By using mouse models with previous molecular annotation, we hypothesized that faithful recapitulation of human PDAC tumorigenesis and influence of specific alterations on tumor progression and TME composition is facilitated, thereby reducing the complex genetic landscape of human PDAC.

To this end, a large cohort of mouse PDAC FFPE tissue samples (n=500) was previously generated in the Saur Lab for which H&E staining was performed on each tissue section. Chen Zhao compiled the cohort of 500 PDAC specimens. Next, a comprehensive histopathological analysis was conducted by board-certified pathologist, Moritz Jesinghaus, providing assessment of tumor grade, annotation of stroma content and immune cell infiltration, as well as quantification of mitoses per HPF for each individual H&E-stained slide.

Tumors were graded according to the following grading system: G1 – well differentiated (low grade), G2 – moderately differentiated (intermediate grade), G3 – poorly differentiated (high grade) and G4 – undifferentiated (high grade) (Edge and Compton, 2010). Representative images of each grading can be found in **Figure 4b**.

Genotypic composition of our cohort encompassed predominantly *Kras*-driven models, either harboring an oncogenic *Kras*^{G12D} alone (PK group) or in combination with additional genetic alterations, such as *Trp53, Cdkn2a, Snail or Tgf*β*.* In contrast, a subset of tumors expressed mutant *Pik3ca*^{H1047R} as main oncogenic driver **(Figure 3a)**. This genotype distribution reflects the human mutational spectrum, where the majority of PDAC patients show activating *KRAS* mutations in combination with recurrent alterations of tumor suppressor genes, most notably *TP53, CDKN2A* and *SMAD4.* Importantly, these GEMMs are molecularly well-defined and extensively characterized in our lab.

Of note, histopathological analysis of prominent TME features, particularly the amount of stroma content or lymphocyte infiltration, revealed high intra- as well as inter-group heterogeneity with respect to individual genotypes. Tumors belonging to the PK (*Kras*^{G12D} mutated) group displayed varying stroma content (between 5 and 70%), while PKT (additional *Tgfbr2* deletion) and *Pik3ca*^{H1047R}-driven (PPI3K and PPI3KP) tumors generally showed higher stroma abundance, although similar variance within the respective groups was noted. In comparison to the overall high stroma content across the PDAC cohort, the proportion of infiltrating lymphocytes (combining T cells and B cells) was mostly low with an average percentage of lymphocytes per section below 10% **(Figure 3b)**.

After integration of all histologically determined variables, we performed unbiased hierarchical clustering of the whole data set, thereby aiming to combine all annotated TME features and link distinct TME phenotypes to their oncogenic driver or histopathological grading. This approach revealed five different clusters, distinguished by unique properties with respect to their TME composition: C1 – lymphocyte high, C2 – proliferating/hybrid, C3 – granulocyte high, C4 – immune excluded and C5 – stroma high **(Figure 3c)**.

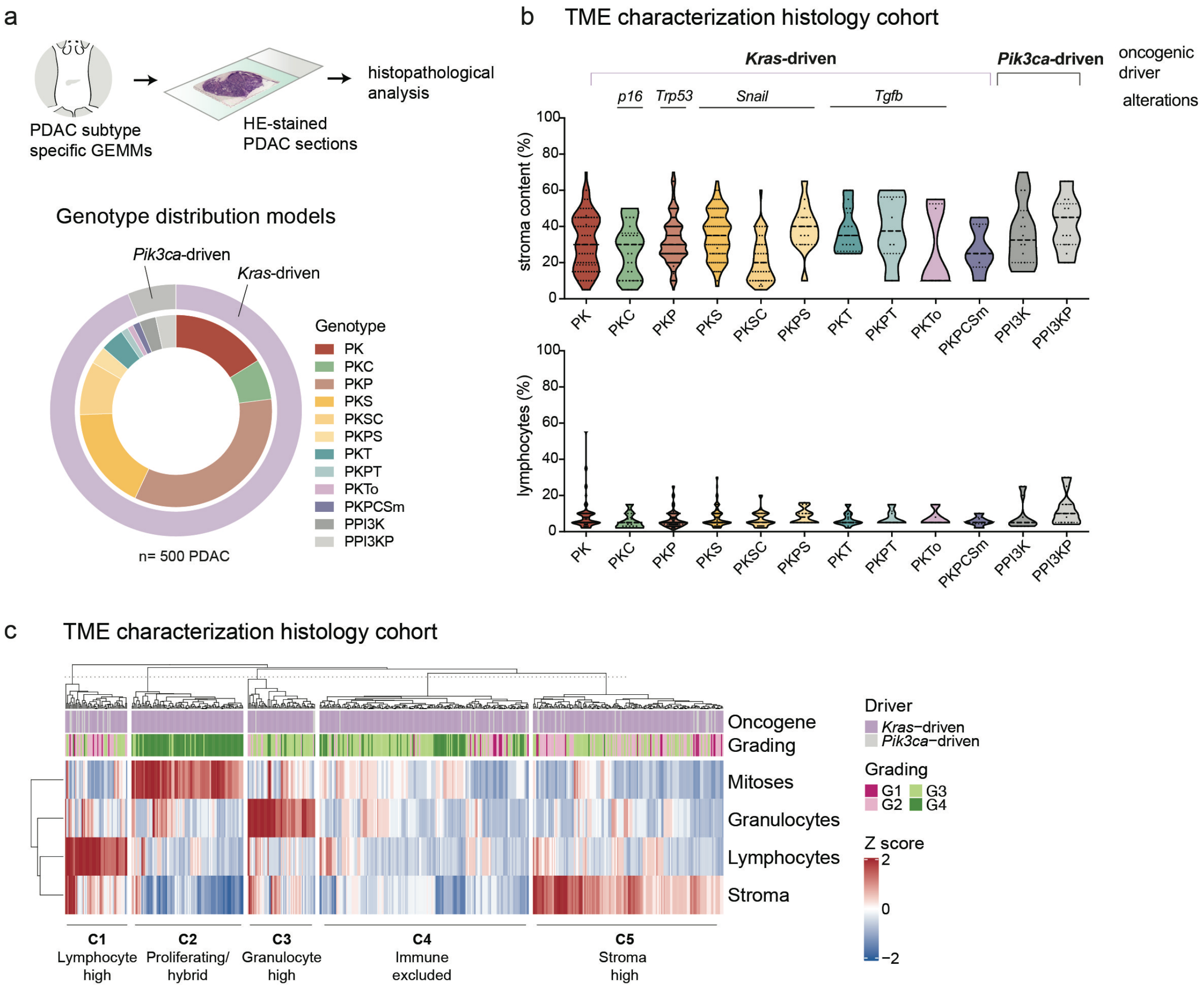

Figure 3. Histopathological analysis and characterization of the TME composition in molecular mouse PDAC subtypes

a, Schematic overview of histopathological workflow (top); pie chart depicting mouse PDAC cohort (n=500 tumors) and genotype model distribution (bottom). PDAC GEMMs were generated by lab members of the Saur and Schneider labs. Sectioning of FFPE specimens and subsequent H&E staining as well as scanning of slides was performed by Chen Zhao. Board-certified pathologist Moritz Jesinghaus assessed tumor grading, granulocyte and lymphocyte infiltration, stroma content and quantified mitoses. Graphical visualization by courtesy of Chiara Falcomatà.

b, Violin plots showing the amount of stroma content (top) and infiltration of lymphocytes (bottom, both in %) across genotype groups in mouse PDAC tissue sections. Genotype groups are annotated with the main oncogenic driver and optionally additional genetic alterations. Each dot represents an individual tumor. The mean is indicated by a dashed line.

c, Unbiased hierarchical clustering of mouse PDAC samples according to annotated histopathological features (mitoses, granulocytes, lymphocytes and stroma content). Samples are further annotated with oncogenic driver and grading. Clustering analysis was performed by Chiara Falcomatà.

Pik3ca^{H1047R}-driven tumors were enriched in the lymphocyte high (C1) and stroma high (C5) cluster. These tumors were also more differentiated as shown by grading assessment (31/40 *Pik3ca*-driven tumors were graded as G1/G2). Generally, the stroma high (C5) cluster was largely composed of G1/G2 tumors. In contrast, undifferentiated (G4) tumors contributed mostly to the proliferating/hybrid (C2) cluster as they displayed the highest abundance of mitotic figures, suggestive of a rapid invasive tumor growth.

The large cohort of *Kras*-driven PDAC samples was represented throughout all grading stages, which was particularly noted for the PK genotype group (n=81), showing no preference of occurrence for any of the grading groups.

Subtyping of human PDAC patients revealed classical and mesenchymal (squamous, basal-like) PDAC as the two major subtypes based on their transcriptional profiles. Molecular subtypes can be used to predict standard chemotherapy sensitivity and tumor progression, and these transcriptional subtypes are also correlative to the differentiation state of the tumor, with the classical subtype being more differentiated and the mesenchymal subtype being poorly differentiated or undifferentiated (Bailey et al., 2016; Collisson et al., 2019; Mueller et al., 2018). On this basis, we stratified the H&E sections of the PK tumors into classical (G1/G2) and mesenchymal (G3/G4) subtypes and conducted a comparative analysis to identify subtype-specific TME differences **(Figure 4a and b).** The classical (G1/G2) cohort (n=30) showed significantly higher stroma content and infiltration of lymphocytes, while the mesenchymal (G3/G4) group (n=51) had a higher number of mitoses indicative of a higher tumor proliferation rate **(Figure 4d)**. Indeed, when comparing the survival of both groups, the mesenchymal (G3/G4) tumors displayed a significant shorter survival compared to the classical (G1/G2) tumors **(Figure 4c)**.

The histopathological assessment did not allow for the identification of specific cell types, such as the distinction between T and B cells or identification of macrophages. Therefore, spatial transcriptomics data of one differentiated classical (G2) and one undifferentiated mesenchymal (G4) tumor was generated, enabling us to analyze the infiltration of immune cell types and their transcriptional states simultaneously in a spatially resolved manner **(Figure 5b)**.

To this end, we used the Visium platform, a spot-based assay which can map the gene expression profile of each capture spot (55 µm in diameter) back to the spatial location within the tissue. This assay does not provide transcriptional profiles at single cell resolution, but can rather capture multiple cell types, depending on their size, on one spot (typically between 3-12 cells). To overcome this limitation, we computationally enhanced the spot resolution to a subspot level by using the BayesSpace toolkit (Zhao et al., 2021). First, spatial clustering was performed with a Bayes clustering algorithm to identify regions with similar gene expression profiles. Next, clustering was enhanced to the subspot level by dividing each spot into six smaller ones **(Figure 5c and e)**. This allowed refinement of spatial clusters, enabling us to investigate the spatial distribution of various cell types of interest in two tumors. Based on their marker gene expression, we identified tumor cells, fibroblasts, macrophages, neutrophils as well as T cells and B cells

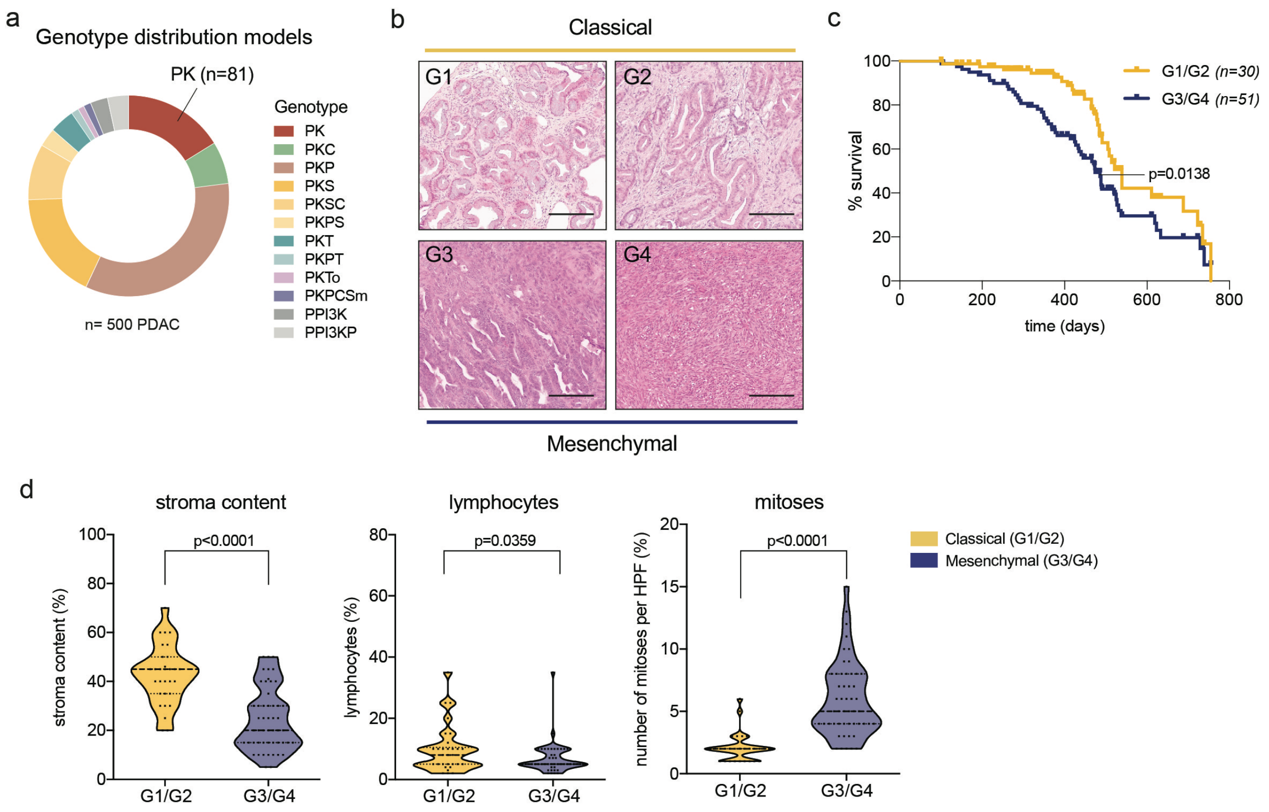

Figure 4. Comparative histopathological analysis of the classical and mesenchymal subtype in Kras-driven mouse PDAC samples

a, Pie chart depicting the mouse PDAC cohort (n=500 tumors) and genotype model distribution, with the proportion of PK tumors highlighted (n=81 tumors). PDAC GEMMs were generated by lab members of the Saur and Schneider labs. Sectioning of FFPE specimens and subsequent H&E staining as well as scanning of slides was performed by Chen Zhao. Board-certified pathologist Moritz Jesinghaus assessed tumor grading, granulocyte and lymphocyte infiltration, stroma content and quantified mitoses.
b, Representative H&E-stained tumor sections of G1-G4-graded PK tumors. G1/G2 are stratified as classical subtype, while G3/G4 tumors are associated to the mesenchymal subtype.
c, Kaplan-Meier survival curve comparing G1/G2 (median survival=539 d) and G3/G4 (median survival=474 d) tumors of the PK cohort. The number of mice per group is indicated and the *P* value was calculated using the Log-Rank (Mantel-Cox) test.
d, Violin plots depicting stroma content, lymphocyte infiltration and number of mitoses by comparing classical (G1/G2) vs mesenchymal (G3/G4) PK tumors. Each dot represents an individual tumor. *P* values were calculated by using a two-tailed, unpaired Student's *t*-test.

(Figure 5e and f). For highly abundant TME cell types, like fibroblasts, macrophages and neutrophils, substantial overlap of their marker gene expression pattern with enhanced spatial clusters was evident.

In contrast, both T cell (*Cd3g*) and B cell *(Cd19)* marker genes were only found to be highly expressed in a scarcity of Bayes-refined subspots, showing that PDAC tumors are excluded from T cells as described in the literature (Binnewies et al., 2018). Accordingly, we identified six subspots with high T cell marker gene expression in the classical tumor and 16 subspots in the mesenchymal tumor **(Figure 6a and b).** Notably, we observed a striking difference in immune infiltration of the cells from the myeloid compartment: the classical tumor showed high expression of neutrophil marker genes (*S100a8, S100a9, Cxcr2*) widely distributed across the tissue section in close proximity to and partly surrounding areas of high tumor cell marker expression. In contrast, the mesenchymal tumor displayed high abundance and spatial distribution of macrophages (*Cd68, Arg1*) over the whole tissue section. As mesenchymal tumors are more undifferentiated, it is challenging to annotate cell-type specific areas based on the morphological appearance from the H&E-stained tissue sections compared to the classical tumors, where tumor-cell- and stroma-rich areas can be clearly identified **(Figure 5b)**. It was furthermore challenging to distinguish mesenchymal tumor cells (*Krt18*, *Cdh2*) from fibroblasts (*Dcn, Pdpn, Col1a2*), as they share a similar gene expression profile. In mesenchymal PDAC, fibroblasts are lowly abundant (as shown by our histopathological analysis), but these tumors are densely packed with mesenchymal tumor cells. Interestingly, we observed a small area of higher classical tumor cell gene expression (*Krt19, Cdh1*) within the mesenchymal tumor. This observation was in concordance with the histopathological annotation of these tumor lesions to be a G2-grade tumor. We furthermore identified several subspots with high expression of neutrophil genes in close proximity to these classical tumor lesions, which recapitulated the phenotype from the classical tumors **(Figure 5f and 6c)**. This observation also highlights the presence of intratumoral heterogeneity and shows that PDAC can consist of multiple subTMEs (Grünwald et al., 2021).

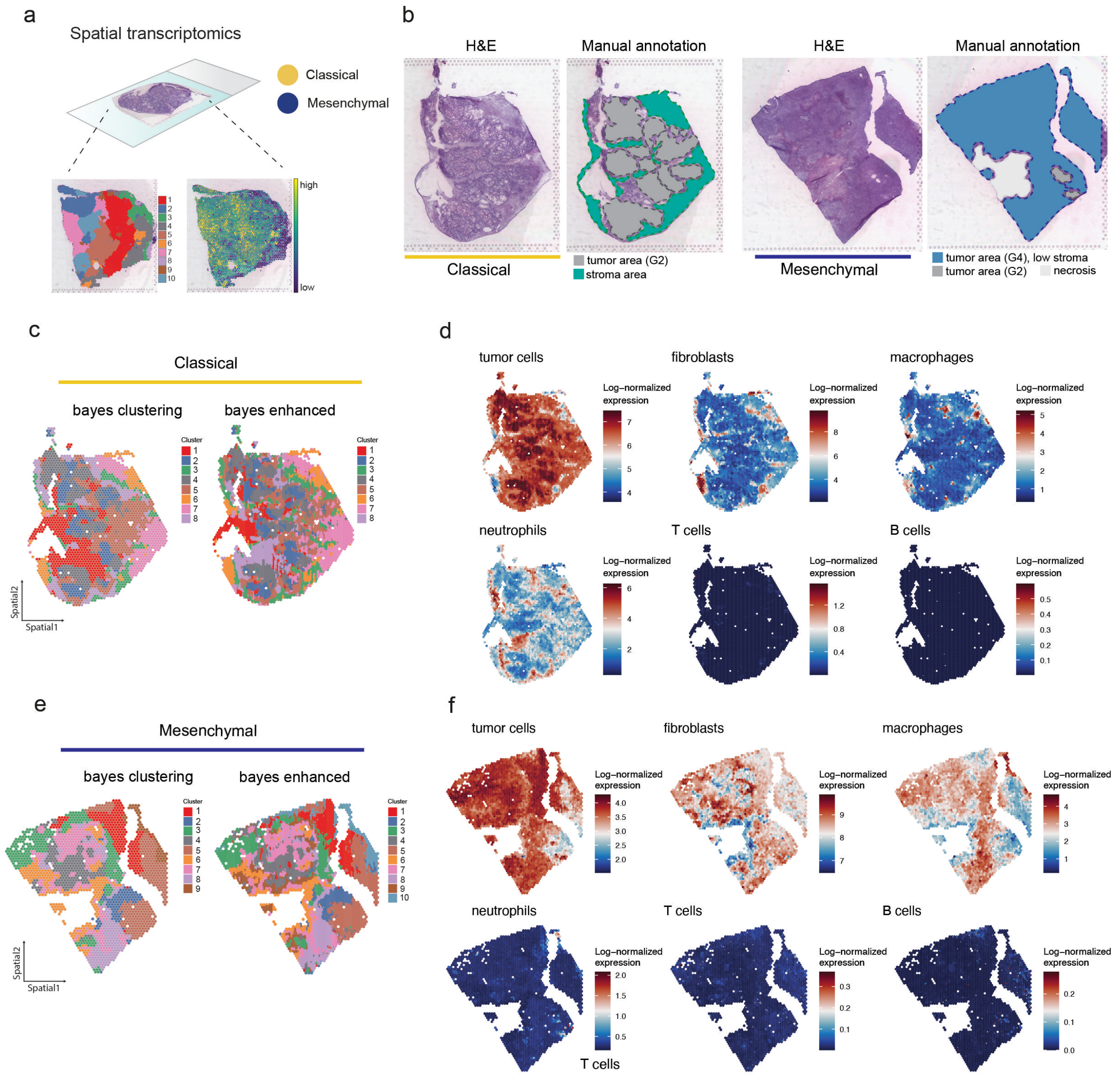

Figure 5. Spatial transcriptomics analysis of classical and mesenchymal tumors to analyze subtype-specific TME features

a, Schematic overview of spatial transcriptomics analysis: a fresh frozen tissue section of interest is placed on a gene expression slide with capture areas. First, fixation of tissue, H&E staining and afterwards imaging of the tissue is performed. Following the 10x genomics Visium Spatial workflow, spatial transcriptomics libraries are generated and sequenced. After alignment of the data, spatial clustering of the barcoded capture spots and other downstream analysis can be performed. We analyzed one classical, differentiated (G2) and one mesenchymal, undifferentiated (G4) tumor. Graphical visualization by courtesy of Chiara Falcomatà.
b, Overview of spatial transcriptomics samples: Left, H&E-stained tissue sections of the classical and mesenchymal tumors are shown. Right, manual annotation of major tumor areas performed by board-certified pathologist Moritz Jesinghaus.
c, Spatial embedding plots of the classical tumor. Left, Bayes spatial clustering of eight identified clusters. Right, Bayes-enhanced spatial clustering at subspot resolution of eight identified clusters.
d, Spatial expression plots at subspot resolution for different cell types defined by marker gene expression: tumor cells (*Krt19, Cdh1)*, fibroblasts (*Dcn, Pdpn, Col1a2),* macrophages (*Cd68, Arg1*), neutrophils (*S100a9, S100a8, Cxcr*2), T cells (*Cd3g*) and B cells (*Cd19*).
e, Spatial embedding plots of the mesenchymal tumor. Left, Bayes spatial clustering of nine identified clusters. Right, Bayes-enhanced spatial clustering at subspot resolution of ten identified clusters.
f, Spatial expression plots at subspot resolution for different cell types defined by marker gene expression: tumor cells (*Krt18, Cdh2*), fibroblasts (*Dcn, Pdpn, Col1a2),* macrophages (*Cd68, Arg1*), neutrophils (*S100a9, S100a8, Cxcr*2), T cells (*Cd3g*) and B cells (*Cd19*). Spatial Transcriptomics cohort was generated together with Chiara Falcomatà. Alignment and initial pre-processing and quality control of data was performed by Giovanni Palla (Theis Lab).

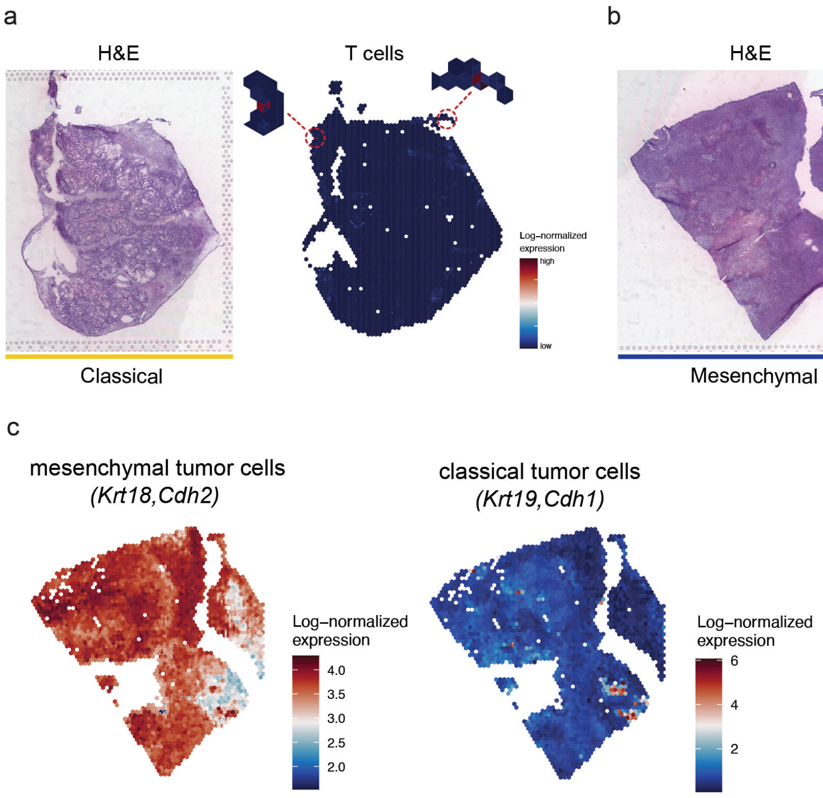

Figure 6. Spatial transcriptomics analysis reveals T cell exclusion and intratumor heterogeneity of tumor cells

a, Left, H&E-stained PDAC section of classical tumor. Right, spatial expression plot for *Cd3g*$^+$ T cells at subspot resolution. Regions with high expression of *Cd3g* are circled in red and zoomed in.
b, Left, H&E-stained PDAC section of mesenchymal tumor. Right, spatial expression plot for *Cd3g*$^+$ T cells at subspot resolution. Regions with high expression of *Cd3g* are circled in red and zoomed in.
c, Spatial expression plots at subspot resolution for mesenchymal (*Krt18, Cdh2*) and classical (*Krt19, Cdh1*) tumor cell marker genes. The mesenchymal tumor shows intratumor heterogeneity and expression classical tumor cell marker genes in a distinct region of the tumor.
Alignment and initial pre-processing and quality control of data was performed by Giovanni Palla (Theis Lab).

Next, to further investigate the spatial dispersion and neighborhoods of the most abundant cell types, we performed differential gene expression analysis of the Bayes enhanced clusters in both subtypes **(Figure 7a and d)**. This yielded in identification of the top enriched marker genes for each cluster, enabling us to link them to specific cell types. Based on the neutrophil spatial dispersion and abundance, we could draw a connection to clusters 5 and 8 of the enhanced Bayes clustering in the classical tumor, whereas clusters 2 and 4 could be mapped to tumor cell marker expression, thus potentially presenting different tumor cell populations **(Figure 7 a,b and c)**. Especially tumor cluster 2 and 4 were directly adjacent to the identified neutrophil clusters 5 and 8, suggesting potential cell-cell interactions between these populations which need to be further explored. Fibroblasts were linked to cluster 3, 6 and highly expressed collagens and ECM genes, such as *Fn1, Col8a1, Col1a2* and *Sparc* **(Figure 7 a and c)**.

In the mesenchymal subtype data set, cluster 1,3 and 5 were annotated as macrophages. Their differentially expressed genes indicated the presence of multiple subpopulations, e.g. *Apoe*^{hi} macrophages showing a different spatial dispersion in comparison to *Ly6c1*^{hi} macrophages. It was furthermore possible to annotate tumor cell dominant clusters (7,8 and 9) which were adjacent to the highly infiltrating macrophage clusters. We hypothesize that cluster 10 presents a fibroblast-dominated cluster as expression of fibroblast associated genes, such as *Tagln* and *Acta2,* but not the tumor cell related genes from cluster 7,8 and 9, was evident **(Figure 7b and c)**. However, further analysis is needed to confirm the purity of our annotation, possibly aided by refined gene expression signatures to profoundly be able to distinguish mesenchymal tumor cells from fibroblasts.

In summary, we analyzed the histopathological features of the two major transcriptional PDAC subtypes and identified differences in their subtype-specific TME composition. Using spatial transcriptomics, we could integrate large-scale gene expression profiling into a histopathological context, providing indications for potential cell-cell crosstalk between tumor and immune cell populations which we set out to further explore in this study.

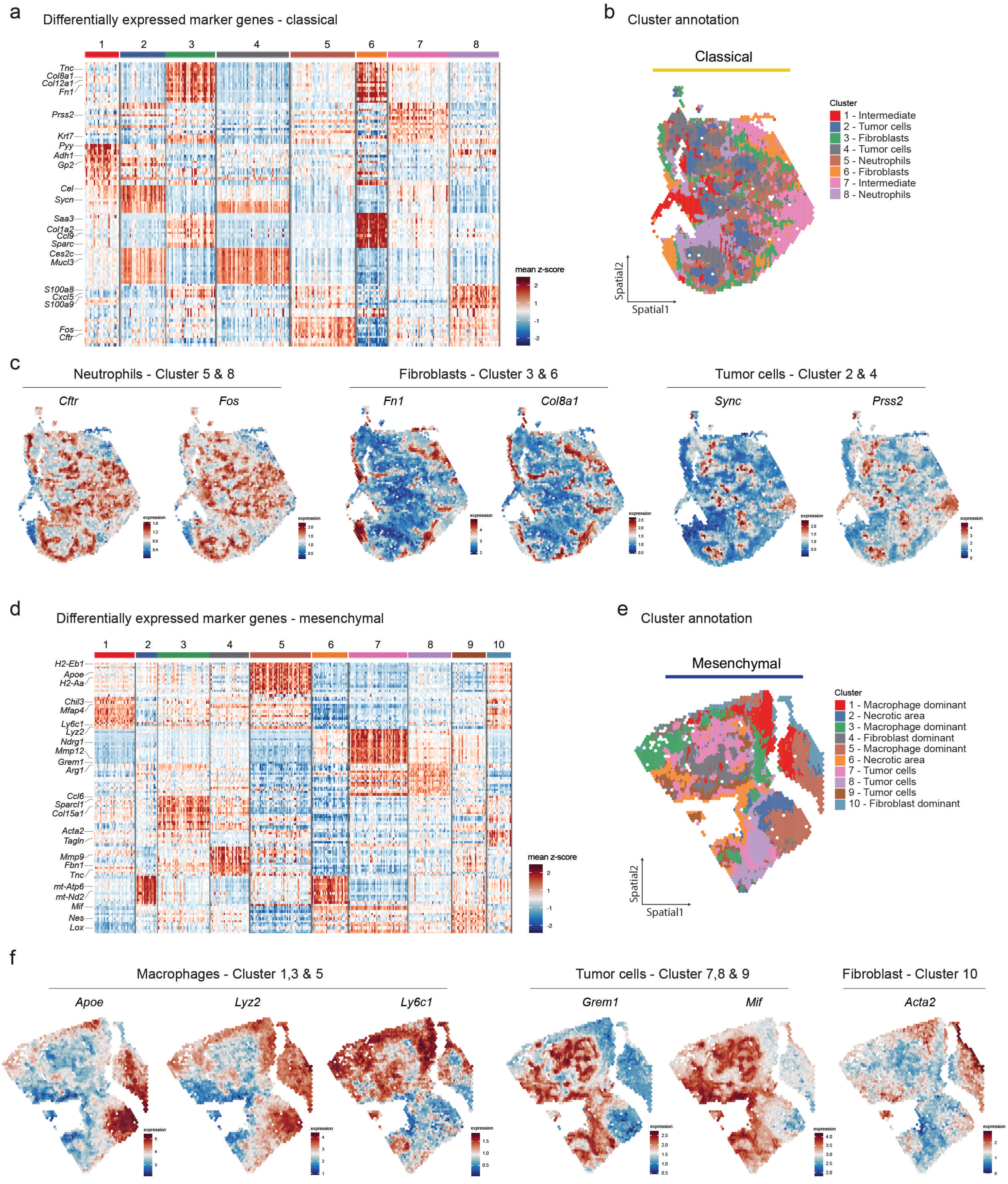

Figure 7. Bayes enhanced clustering reveals spatially variable TME cell types

a, Heatmap displaying the top 15 differentially expressed genes per cluster of the classical tumor. Selected genes are annotated on the left site.
b, Bayes-enhanced spatial clustering at subspot resolution of eight identified clusters with annotated cell type populations of the classical tumor.
c, Spatial expression plots at subspot resolution for neutrophils – cluster 5 & 8 (*Cftr, Fos*), fibroblasts – cluster 3 & 6 (*Fn1, Col8a1*) and tumor cells – cluster 2 & 4(*Sync, Prss2*) in the classical tumor.
d, Heatmap displaying the top 15 differentially expressed genes per cluster of the mesenchymal tumor. Selected genes are annotated on the left site.
e, Bayes-enhanced spatial clustering at subspot resolution of ten identified clusters with annotated cell type populations of the mesenchymal tumor.
f, Spatial expression plots at subspot resolution for macrophages – cluster 1,3 & 5 (*Apoe, Lyz2, Ly6c1*), tumor cells – cluster 7,8 & 9 (*Grem1, Mif*) and fibroblast – cluster 10 (*Acta2*).

4.2. Classical and mesenchymal PDAC differ substantially in infiltrating myeloid cells

Next, to assess sub-type specific TME characteristics in a systematic fashion, we performed flow cytometry and scRNA-seq of both subtypes, using an *in vivo* orthotopic implantation model. This enabled us to focus specifically on immune infiltrates **(Figure 8a)**. Orthotopic allografts are standardized and reproducible PDAC models which hold important advantages over endogenous GEMMs to systematically analyze immune infiltration, such as predictable tumor progression and known phenotypic peculiarity of PDAC subtypes of interest. Endogenous PDAC GEMMs from the same genotype often display a high heterogeneity in terms of tumor progression, metastasis formation and differentiation state, as seen in our initial histopathological analysis. Previously, we performed a large-scale implantation experiment to analyze treatment-induced effects of a combinatorial therapy in both subtypes which among other things revealed that the classical and mesenchymal subtype of the implanted cell line was preserved after implantation **(Figure 8b)** (Falcomatà et al., 2022). Moreover, we can utilize this system to genetically perturb cell lines, e.g. via CRISPR-Cas9, to then study these effects on the TME composition. Thus, orthotopic implantation models present a valuable tool for functional studies.

For the purpose of immune infiltrate characterization, previously generated mouse cell lines from endogenous PK mice were used: these cell lines were deeply characterized and stratified into classical and mesenchymal subtypes based on their gene expression profile by RNA-seq analysis, which also correlated to the cell line morphology and histological grading of the tumors arising after orthotopic implantation of the respective cell line **(Figure 8b, left)** (Mueller et al., 2018). This procedure enables to systematically link tumor-cell intrinsic attributes to TME phenotypes according to the classical or mesenchymal subtype. Thus, we chose multiple PK cell lines representing the classical (n=5) and mesenchymal (n=5) subtype and orthotopically implanted them into the pancreas of syngeneic immunocompetent C57Bl6/J mice. Flow cytometry analysis of an innate and adaptative antibody panel was performed when mice were moribund. Using the innate panel, the following immune cell populations were analyzed: macrophages, neutrophils, dendritic cells and NK cells. With the adaptive panel, we could identify B cells and T cells as well as specific T cell subsets. Classical and mesenchymal PK tumors displayed a remarkable difference in the abundance of myeloid cells. Neutrophils occurred in significantly higher amounts in classical tumors while, in contrast, mesenchymal tumors displayed significantly elevated numbers of macrophages **(Figure 8c, upper panels)**. We did not observe a significant difference in T cell infiltration, but some mesenchymal tumor lines showed a higher CD8$^+$ and CD4$^+$ T cell fraction than most classical lines **(Figure 8c, lower panels)**.

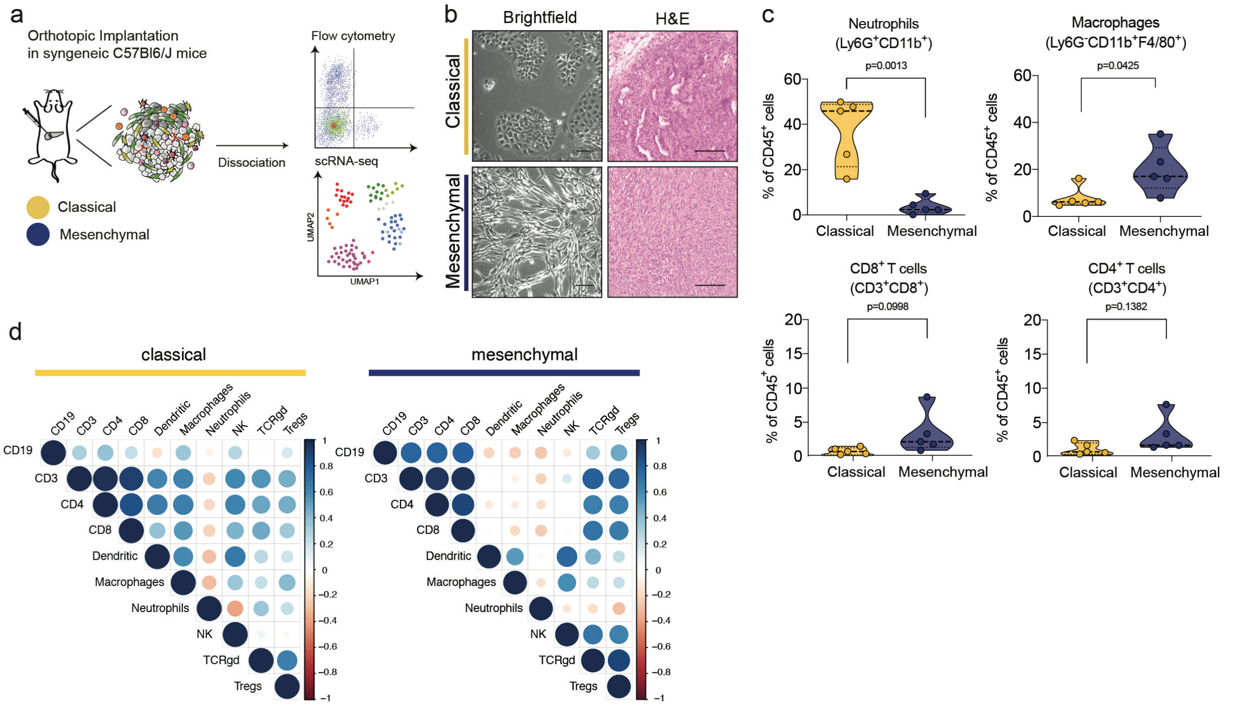

Figure 8. Systematic analysis of immune infiltration in PDAC subtypes by using an orthotopic implantation model

a, Schematic overview of analysis workflow: orthotopic implantation of multiple cell lines representing the classical and mesenchymal subtype into the pancreas of syngeneic C57Bl6/J mice. Resulting tumors were dissociated and deployed for flow cytometry immunophenotyping and/or scRNA-seq analysis.
Graphical visualization by courtesy of Chiara Falcomatà.
b, Left, representative brightfield images of classical and mesenchymal PK cell lines. Right, representative H&E-stained tissue sections of implanted classical and mesenchymal tumors. Scale bars are 100 µm..
c, Flow cytometry staining for neutrophils (Ly6G$^+$CD11b$^+$), macrophages (Ly6G$^-$CD11b$^+$F4/80$^+$), CD8$^+$ T cells (CD3$^+$CD8$^+$) and CD4$^+$ T cells (CD3$^+$CD4$^+$) of classical and mesenchymal tumors, depicted as fraction of CD45$^+$ cells (in %). Each dot represents an individual implanted cell line from at least 3 recipient mice, and average values are depicted. *P* values were calculated by using a two-tailed, unpaired Student's *t*-test.
d, Cell type correlation analysis resulting from flow cytometry data by Spearman's rank correlation in classical and mesenchymal implanted tumors. All *P* values are shown. Orthotopic implantations and flow cytometry experiments were performed together with Chiara Falcomatà, Jack Barton and Saskia Ettl. The correlation analysis was performed by Chiara Falcomatà.

In classical tumors, we noted a negative correlation of neutrophils to T cell subsets (CD8$^+$, CD4$^+$), B cells and NK Cells as well as macrophages and dendritic cells. In mesenchymal tumors, macrophage occurrence was negatively correlated to the same T cell subsets and neutrophils, but positively correlated to dendritic cells **(Figure 8d)**.

Next, we performed scRNA-seq analysis from selected tumors of our implantation experiment, representing both subtypes (classical n=2 lines, mesenchymal n=3 lines). In total we generated fourteen 3'-scRNA-seq libraries using the 10x v3 and v3.1 chemistry, which were comprised of up to 3 replicates (individual tumors) per implanted cell line to enhance robustness and cell type representation in our analysis. All libraries were pre-processed jointly and then integrated with BBKNN batch correction in the Scanpy environment (Polański et al., 2020; Wolf et al., 2018). The final data set with all integrated tumor samples contained 54,835 cells and the resulting Leiden clusters were annotated by using well-known marker genes for each cell type **(Figure 9a and d)**.

Individual libraries, including replicates, were first jointly annotated according to tumor-inducing cell line which were further stratified either as classical or mesenchymal subtype (classical: 8442, 8661; mesenchymal: 9091, 8513, 8570) **(Figure 9b)**.

Next, cell type proportions of classical and mesenchymal tumors were compared and, similar to the flow cytometry phenotyping, differences in cell type abundance between classical and mesenchymal tumors were noted. Higher fractions of macrophages as well as monocytes were identified in the samples derived from mesenchymal tumors, whereas higher proportions of neutrophils, NK cells and B cells were detected in the classical subtype **(Figure 9c)**. Interestingly, fibroblasts were lowly abundant, especially in the classical tumors, which contradicts our previous histopathological and spatial transcriptomics analysis. One possible explanation is that more sensitive cell types, such as fibroblasts, are underrepresented in scRNA-seq analysis, because they are more prone to undergo apoptosis during the long tissue preparation process, particularly during tissue dissociation. While immune cells are generally considered more viable under tissue dissociation stress, they are also smaller in size and are therefore expected to be captured more effectively during the microfluidics single cell encapsulation.

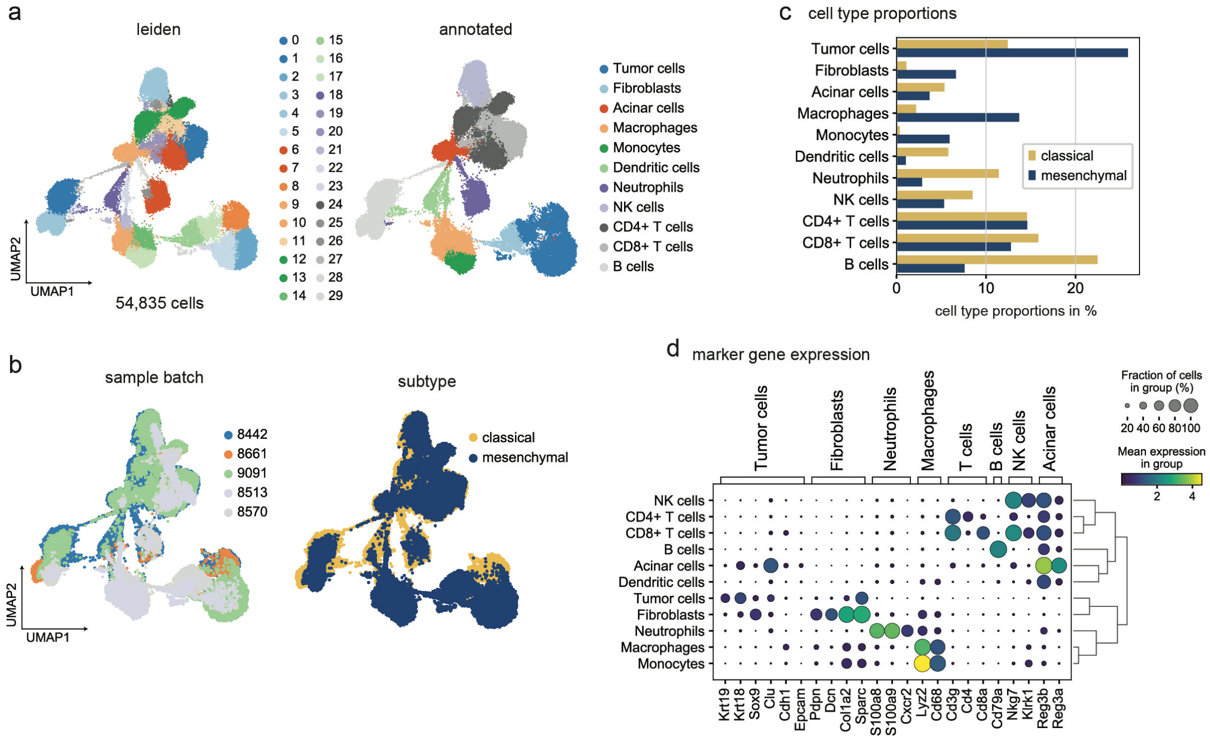

Figure 9. scRNA-seq analysis of implanted classical and mesenchymal tumors to analyze the subtype-specific immune cell phenotypes

a, Left, UMAP embedding shows the Leiden clustering of the integrated scRNA-seq data set (54,835 cells). Clustering resolution was adjusted to distinguish fibroblasts from mesenchymal tumor cells as they have a similar gene expression profile. Right, the resulting 29 clusters were annotated according to typical marker gene expression.
b, Left, UMAP plots showing integration of 5 different tumor lines (classical: 8442, 8661; mesenchymal: 9091, 8513 and 8570) after BBKNN batch correction. Right, UMAP embedding showing annotation of classical and mesenchymal subtype.
c, Cell type proportions in percent of annotated cell types divided into classical and mesenchymal subtype.
d, Dot plot depicting expression of selected marker genes for each annotated cell type for both subtypes.
Single cell experiments were performed together with Chiara Falcomatà and supported by Albulena Toska.

To investigate the phenotypic states of specific cell types, we extracted these cells from the whole scRNA-seq data set and re-clustered them at a higher resolution, aiming to identify functional subsets. First, we analyzed the tumor cell clusters and annotated them according to their previously known subtype as classical or mesenchymal. Tumor cells derived from classical implanted tumor lines clustered together and were separated from the mesenchymal lines, which were not overlapping to a large extent, potentially indicating that these differ in their mesenchymal gene expression states **(Figure 10a and b)**. We performed a differential gene expression analysis between the classical and mesenchymal annotated cells and showed that they were mainly distinguished by classical and mesenchymal marker genes, such as *Clu* and *Krt19* for classical tumor cells and *S100a4* and *Timp1* for mesenchymal tumor cells **(Figure 10 c and d)**.

Moreover, we investigated CAF subtypes in our data sets and extracted the fibroblast cluster for this analysis. As mentioned above, the number of sequenced fibroblasts from both subtypes did not match to our results of the histopathological analysis. With this bias in mind, we annotated the clusters with well-known CAF subsets, which were previously identified in studies of mouse and human PDAC (Elyada et al., 2019; Öhlund et al., 2017). The majority of fibroblasts derived from mesenchymal tumors belonged to the myoCAF and iCAF subtypes, while only a minority of cells was annotated as apCAFs. In contrast, classical tumors displayed high abundance of myoCAFs **(Figure 10 e and f)**. To enhance this analysis, it would be desirable to enrich for fibroblasts and then subject this enriched cell type to scRNA-seq analyses. Moreover, optimized dissociation protocols of tumors could lead to higher fibroblast fractions as well (Dominguez et al., 2020; Elyada et al., 2019; Hutton et al., 2021).

As shown above, classical and mesenchymal tumors varied significantly in their amount of infiltrating myeloid cells. To characterize their phenotypes, we analyzed the clusters of neutrophils and macrophages/monocytes more in depth by extracting them from the whole data set and performing clustering with a higher resolution. For the macrophage/monocyte dataset (8,154 cells), three distinct macrophage clusters could be identified: *C1q*-high, *Spp1*-high and *Ly6c*-high macrophages which were annotated by the expression of signifying marker genes **(Figure 11f)**. The occurrence of these subtypes is in line with recent evidence that describes these populations of tumor-associated macrophages in the context of cancer. Furthermore, *Ly6c*-high monocytes, MonoDCs (Monocytes expressing dendritic cell specific genes) and a fraction of dendritic cells emerged as separate clusters **(Figure 11a, left)**. The majority of cells from this data set is derived from the mesenchymal subtype, whereas a substantially smaller fraction of cells belongs to the classical subtype **(Figure 11a, right)**. Higher contribution of cells from the mesenchymal subtype was noted for all three major macrophage subsets as well as the *Ly6c*-high monocytes. Conversely, cells derived from classical tumors contributed to the majority of MonoDCs and dendritic cells **(Figure 11b)**. Analyzing the cell type proportions of individual tumors from both subtypes, we observed heterogeneity within subtypes. Tumors arising from the implantation of mesenchymal tumor line 9091, for example, displayed a lower fraction of total macrophages

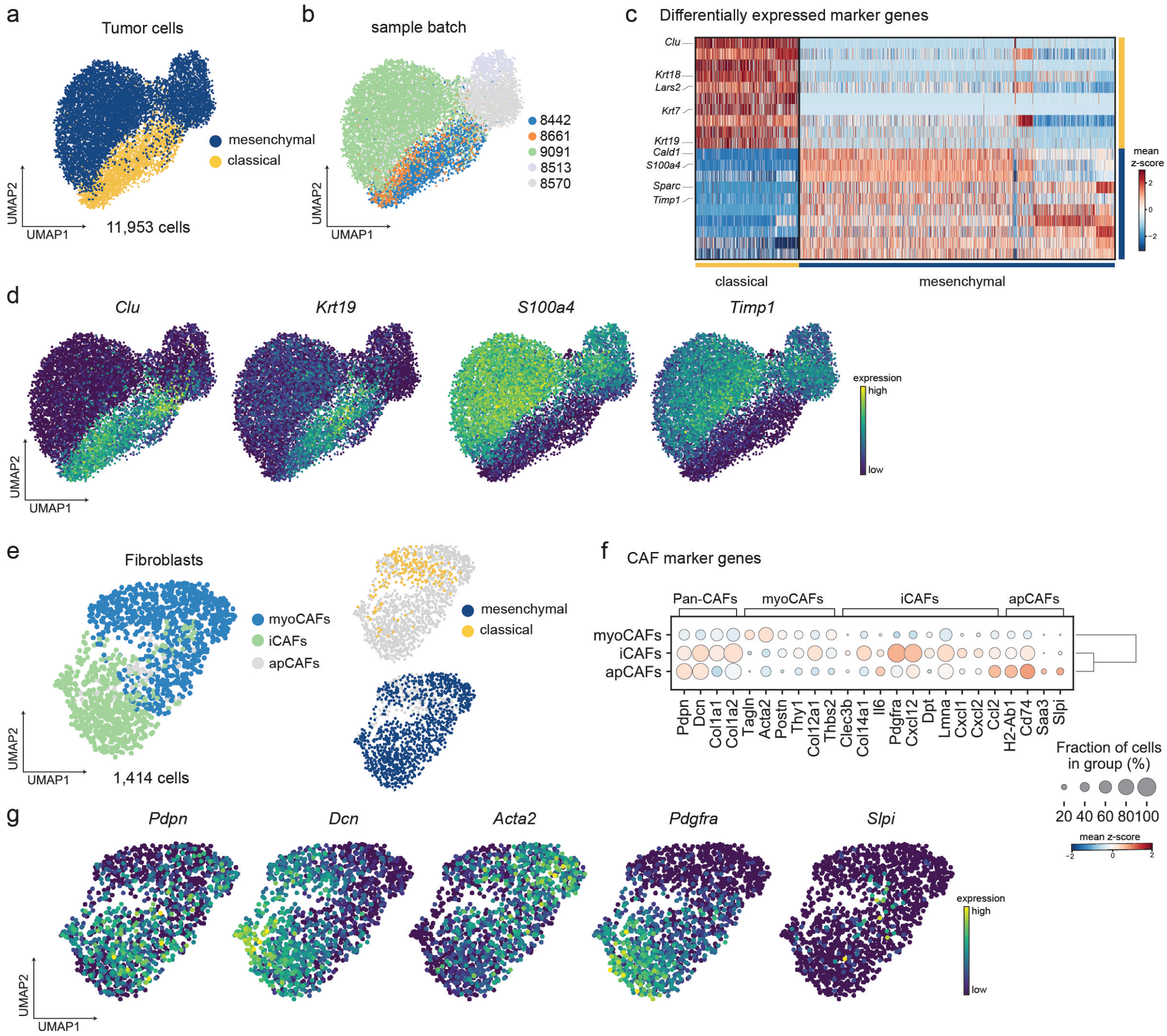

Figure 10. scRNA-seq analysis of tumor cells and fibroblasts

a, UMAP plot of tumor cells (11,953 cells) colored by annotated classical and mesenchymal subtype.
b, UMAP plot showing integration of 5 different tumor lines (classical: 8442, 8661; mesenchymal: 9091, 8513 and 8570) after BBKNN batch correction.
c, Heatmap displaying the top 10 differentially expressed genes per annotated cluster. Selected genes are annotated on the left site.
d, UMAP plots showing expression of differentially expressed genes; classical: *Clu* and *Krt19*, mesenchymal: *S100a4* and *Timp1.*
e, Left, UMAP plot of fibroblasts (1,414 cells) colored by annotated CAF subpopulations. Right, UMAP plots showing the distribution of cells from classical and mesenchymal tumors.
f, Dot plot depicting expression of selected marker genes for each annotated CAF subpopulation for both subtypes
g, UMAP plots showing expression of pan-CAF markers *Pdpn* and *Dcn*, myoCAF marker *Acta2*, iCAF marker *Pdgfra* and apCAF marker *Slpi*.
Single cell experiments were performed together with Chiara Falcomatà and supported by Albulena Toska.

compared to the other two mesenchymal lines and had similar proportions to the classical 8661 line. Interestingly, classical tumors showed no contribution to *Ly6c*-high monocytes.

Differential gene expression analysis between identified myeloid cell subpopulations revealed that *C1q-high* macrophages are characterized by the highest expression of *Apoe*, previously identified as marker gene for immunosuppressive macrophages in PDAC (Kemp et al., 2021a).

In contrast, the smaller fraction of *Spp1*-high macrophages showed the highest expression of *Fn1, Vegfa* and *Arg1* **(Figure 11d)**. *Arg1* as well as *Trem2* were recently reported as marker genes of highly immunosuppressive macrophage populations and are strongly expressed in our annotated macrophage subpopulations, but not in monocytes/dendritic cells (Katzenelenbogen et al., 2020). Although *Spp1*-high macrophages showed the highest expression of *Arg1* and *C1q*-high macrophages the highest *Trem2* expression, all macrophage populations generally co-expressed both marker genes **(Figure 11g)**. We performed differential gene expression between cells derived from the mesenchymal and classical dataset and analyzed HALLMARK gene sets, focusing on enrichments in mesenchymal-derived cells. Two of the top immune-related enriched gene sets in the mesenchymal subtype were ‘TNFα signaling’ as well as ’Interferon gamma response’, suggesting inflammatory functions **(Figure 11e)** (Tu et al., 2021).

Collectively, our macrophage/monocyte-centered analysis revealed the presence of distinct macrophage subpopulations characterized by an immunosuppressive gene expression profile. *C1q*-high, *Spp1*-high and *Ly6c*-high cells were predominantly derived from the mesenchymal PDAC subtype, whereas the classical subtype showed higher fractions of MonoDC cells.

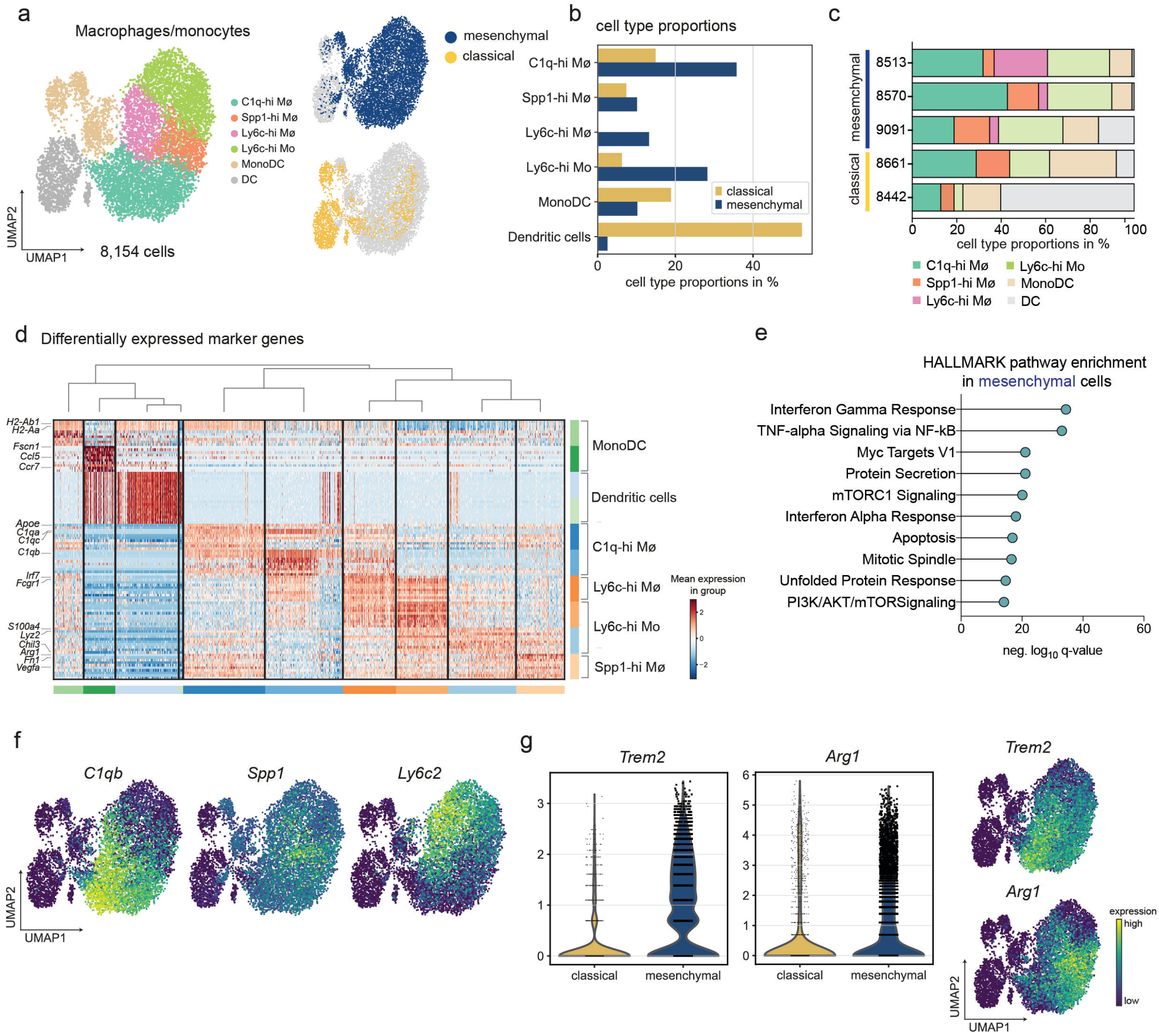

Figure 11. scRNA-seq analysis reveals immunosuppressive phenotype of infiltrating macrophages/monocytes

a, Left, UMAP plot of macrophage/monocyte cells (8,154 cells) colored by annotated cell subpopulation from classical and mesenchymal tumors. Right, UMAP plots showing the distribution of cells from classical and mesenchymal tumors.
b, Cell type proportions in percent of annotated macrophage/monocyte subpopulations divided into classical and mesenchymal subtype.
c, Cell type proportions in percent of annotated macrophage/monocyte subpopulations divided by implanted PK cell lines from classical and mesenchymal subtypes.
d, Heatmap displaying the top 10 differentially expressed genes per cluster. Selected genes are annotated on the left site and clusters are annotated with identified subpopulations on the right.
e, GSEA pathway enrichments (HALLMARK gene set) from differentially expressed genes in cells derived from mesenchymal tumors compared to classical tumors.
f, UMAP plots showing expression of macrophage marker genes *C1qb*, *Spp1* and *Ly6c2*.
g, Left, Violin plots showing the expression of *Trem2* and *Arg1* which characterize an immunosuppressive macrophage subset, between classical and mesenchymal tumors. Right, UMAP plots showing expression of *Trem2* and *Arg1.*
Single cell experiments were performed together with Chiara Falcomatà and supported by Albulena Toska.

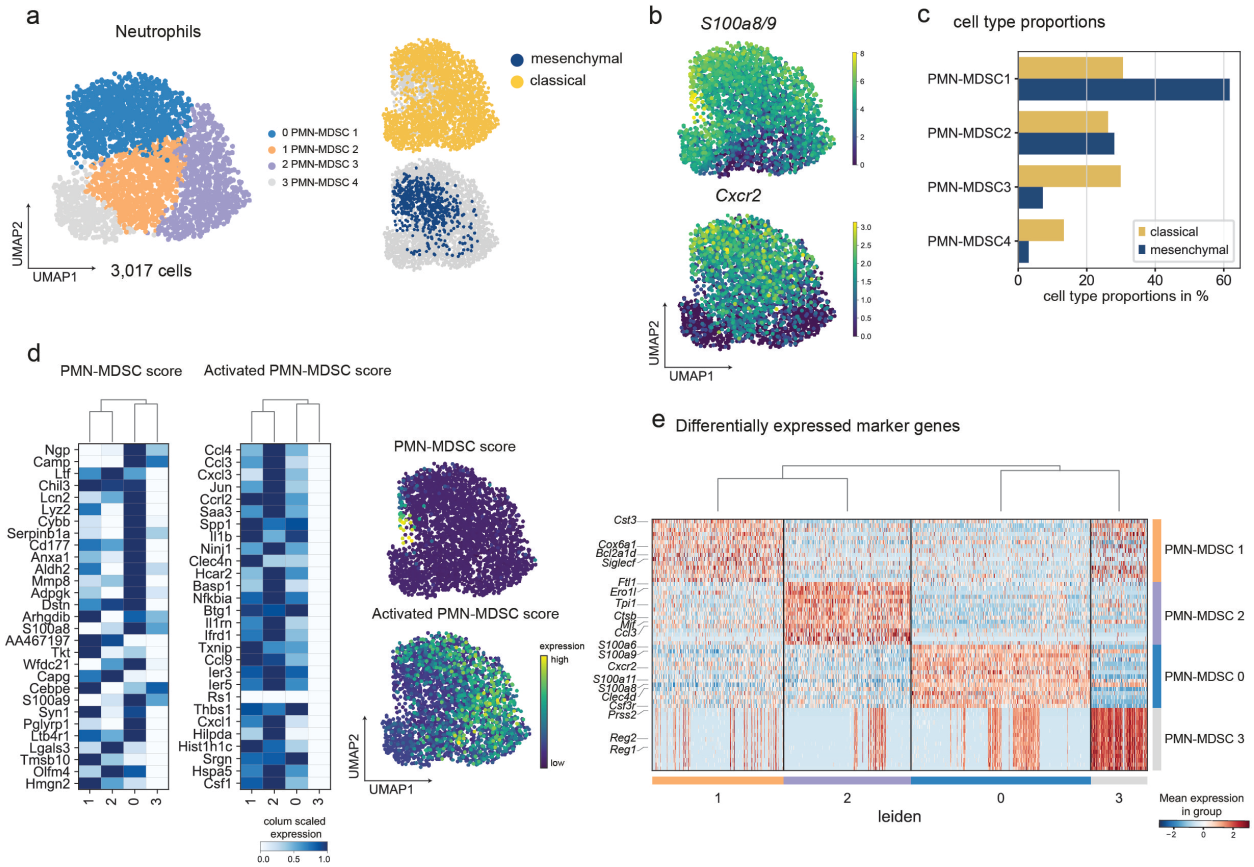

Figure 12. Neutrophil subpopulations display an immunosuppressive activated PMN-MDSC phenotype and are enriched in classical tumors

a, Left, UMAP plot of neutrophil cells (3,017 cells) colored by annotated Leiden clusters with cell subpopulations from classical and mesenchymal tumors. Right, UMAP plots showing the distribution of cells from classical and mesenchymal tumors.
b, UMAP plots depicting expression of neutrophil marker genes *S100a8/9* and *Cxcr2*.
c, Cell type proportions in percent of annotated neutrophil subpopulations divided into classical and mesenchymal subtype.
d, Left, heatmap displaying the expression of genes from ‘PMN-MDSC’ and activated ‘PMN-MDSC’ gene sets. Right, UMAP plot depicting the score of ‘PMN-MDSC’ and ‘activated PMN-MDSC’ gene sets.
e, Heatmap displaying the top 15 differentially expressed genes per cluster. Selected genes are annotated on the left and clusters with identified PMN-MDSC subpopulations on the right side.
Single cell experiments were performed together with Chiara Falcomatà and supported by Albulena Toska.

Next, we performed immunophenotyping of the subtype-specific neutrophil compartment following the same analysis workflow as for the macrophage data set. In general, neutrophils can be characterized by high expression of the marker genes *S100a8, S100a9 and Cxcr2* **(Figure 12b)** (Bronte et al., 2016).

In contrast to the macrophage dataset, cells derived from classical tumors make up the majority of neutrophils, while mesenchymal derivates only show a minor contribution **(Figure 12a)**. This recapitulates our results from the flow cytometry phenotyping, showing a significantly higher infiltration of neutrophils in classical PDAC tumors. As neutrophils are often synonymously described as PMN-MDSC cells in cancer, we compared the gene expression profiles and phenotypes of PDAC PMN-MDSC cells against results of a recent study which provided comprehensive functional characterization of tumor-derived PMN-MDSCs (Veglia et al., 2021a).

We analyzed the expression of the reported ‘PMN-MDSC’ and ‘Activated PMN-MDSC’ gene sets in our neutrophil data set and computed scores for both gene sets. Remarkably, the majority of cells belonging to clusters 0-2 (annotated as PMN-MDSC1-3) displayed high expression of the activated PMN-MDSC genes and only a small fraction of cells from cluster 0 (PMN-MDSC1) were highly expressing the PMN-MDSC genes **(Figure 12d)**. Notably, cluster 0 (PMN-MDSC1) consisted of a higher fraction of cells derived from mesenchymal tumors compared to cells from classical tumors **(Figure 12d)**. Activated PMN-MDSC genes are associated with an immunosuppressive activity and corresponding cells that express these signatures are widely present in cancer (Veglia et al., 2021a; Veglia et al., 2021b). Cluster 3 (PMN-MDSC4) was generally characterized by a lower transcriptional activity and did not express activated PMN-MDSC genes at a high level.

In summary, the here identified neutrophils mostly display an activated PMN-MDSC phenotype, indicating an immunosuppressive activity in conjunction with high expression of multiple chemokines.

4.3. The PDAC T cell compartment is characterized by T cell exhaustion

PDAC is described as an immunologically “cold” tumor, characterized by exclusion of T cells from the tumor core and an overall marginal infiltration of T cells (Binnewies et al., 2018). Concordantly, we detected low numbers of T cells in our flow cytometry analysis. Next, we analyzed the T cell compartment within our scRNA-seq data and identified distinct T cell subpopulations **(Figure 13a)**. We captured a large number of T and NK cells (20,055 cells) for both classical and mesenchymal subtype, which stands in contrast to our flow cytometry data. However, this discrepancy can be attributed to an increased viability of immune cells, especially T cells, after tumor dissociation in comparison to relatively large tumor cells or fibroblasts, thus providing explanation for the observed enrichment in the scRNA-seq analysis. T cell subsets were identified by analysis of reference marker genes describing naïve-like, cytotoxic, effector, memory and regulatory T cells as well as NK cells **(Figure 13c and d)**. The T cell compartment in many solid cancer entities is described as exhausted and dysfunctional (Wherry and Kurachi, 2015). Therefore, we analyzed the expression of T cell exhaustion markers, such as *Pdcd1, Havcr2, Lag3* and *Tigit* as well as other co-stimulatory genes **(Figure 13e and f)**. We observed high expression of these genes in the CD8$^+$ subset as well as regulatory T cells which was accompanied by a low cell cycle score within these populations, indicating an exhausted phenotype **(Figure 13g).** Effector T cells – typically only represented by a small fraction of cells – on the other hand showed a high expression of these activation markers and a high cell cycle score **(Figure 13g)**. Generally, mesenchymal dataset-derived cells were enriched in the cytotoxic CD8$^+$ and Tregs cluster, and classical cells showed highest representation in naïve-like CD4$^+$ and NK cell cluster **(Figure 13b)**.

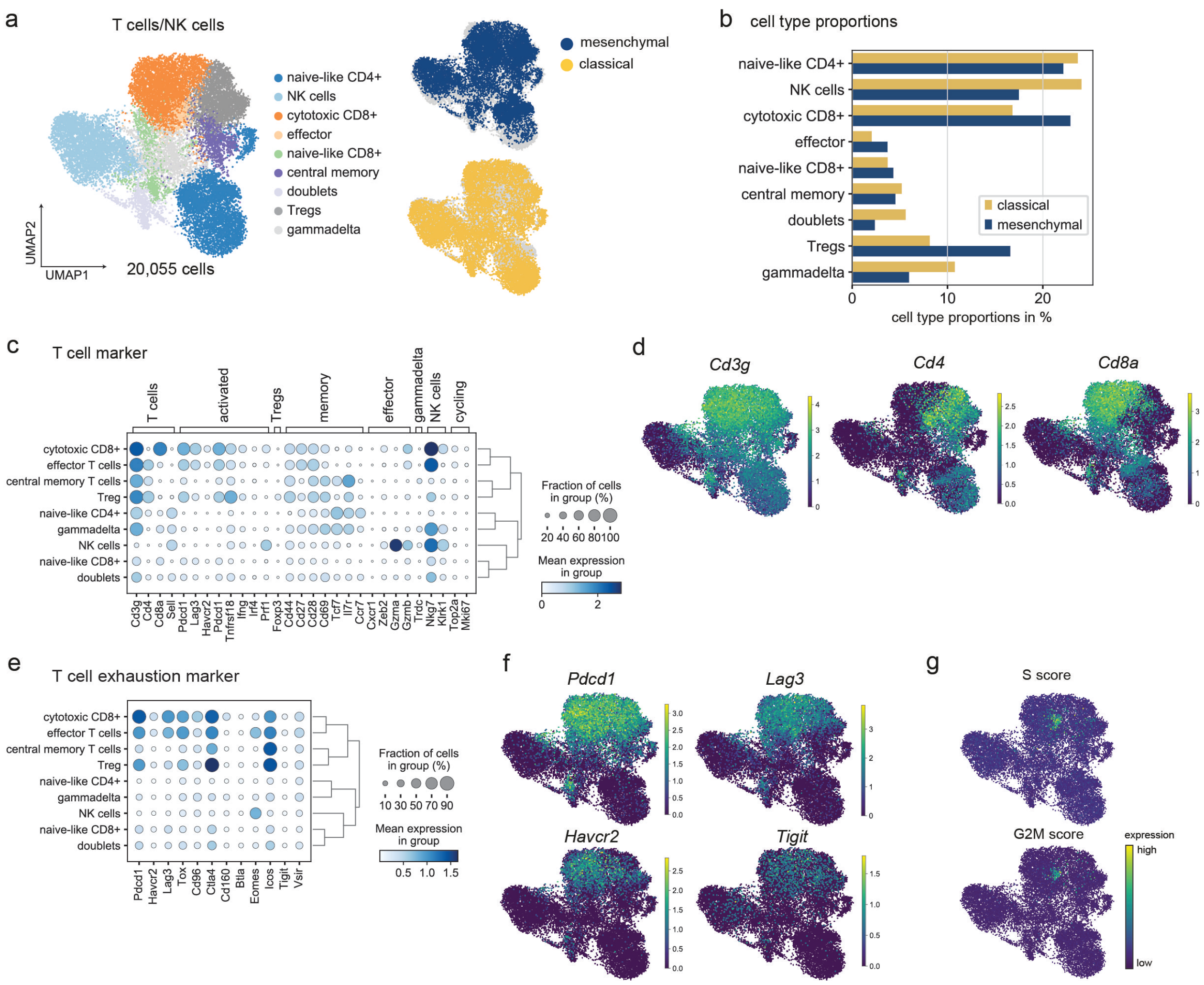

Figure 13. T cells in both classical and mesenchymal tumors are characterized by an exhausted phenotype

a, Left, UMAP plot of T and NK cells (20,055 cells) colored by annotated Leiden clusters with cell subpopulations from classical and mesenchymal tumors. Right, UMAP plots showing the distribution of cells from classical and mesenchymal tumors.
b, Cell type proportions in percent of annotated T and NK cell subpopulations divided into classical and mesenchymal subtype.
c, Dot plot depicting marker gene expression of various T cell subpopulations and NK cells. Annotated cell subsets can be found on the left y-axis.
d, UMAP embeddings displaying the expression of *Cd3g, Cd4* and *Cd8a*.
e, Dot plot depicting expression of different T cell exhaustion marker genes, mainly inhibitory receptors, across annotated subpopulations.
f, UMAP plots show expression of selected exhaustion markers: *Pdcd1, Lag3, Havcr2* and *Tigit*.
g, UMAP plots depicting the cell cycle scores (S and G2M) based on a cell cycle gene set.
Single cell experiments were performed together with Chiara Falcomatà and supported by Albulena Toska.

4.4. Cell-cell communication analysis reveals distinct routes of immune cell recruitment and immunosuppression

We next set out to delineate the context-specific cell-cell communication networks in the classical and mesenchymal PDAC subtype by performing a systematic interaction analysis, thereby aiming to address the following questions: (i) Which factors are secreted by classical and mesenchymal tumor cells, leading to distinct myeloid infiltrates in the TME? (ii) Is T cell suppression mediated via a direct tumor – T cell interaction or indirectly, through myeloid – T cell interactions? and (iii) How do classical and mesenchymal PDAC globally differ in signaling pathways of their cell-cell communication network? From the evidence of our scRNA-seq data, we propose a cell-cell communication model which we wanted to refine further **(Figure 14)**. To this end, we first addressed the question of how tumor cell subtypes govern immune cell recruitment by secretion of chemokines/cytokines whose signaling activity leads to infiltration and proliferation of immune cell populations. We integrated two complimentary approaches: first, *in vitro* MS-based secretome analysis of conditioned media from cell cultures (n=25 cell lines) derived from each subtype allowed us to identify tumor cell secreted proteins. Second, we inferred ligand-receptor interactions (using the CellChat toolkit) from our integrated scRNA-seq data set of both subtypes, with the directionality of signaling from tumor cells (source of ligands) to immune cells (expression of the corresponding receptors) (Jin et al., 2021).

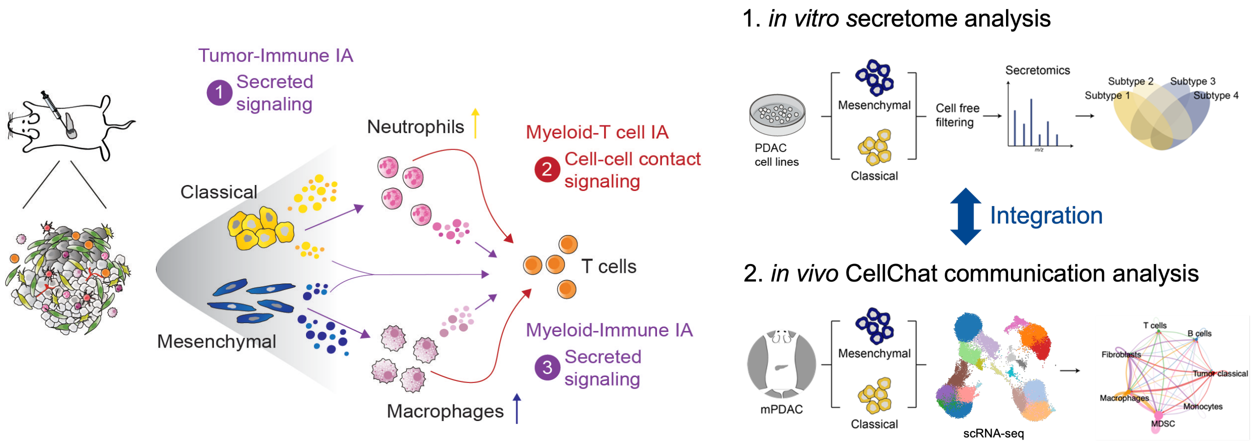

Figure 14. Cell-cell communication analysis integrating secretome and scRNA-seq data to delineate the subtype-specific interaction network

Left, Schematic overview of proposed cell-cell communication model: (1) Investigation of tumor-immune signaling to identify secreted factors of tumor cell subtypes which differently recruit myeloid immune cells (neutrophils or macrophages) to the PDAC TME. (2) Analysis of cell-cell contact signaling between myeloid cells and T cells to identify signaling routes of T cell suppression. (3) Analysis of secreted signaling between myeloid cells and T cells. Right, Schematic overview of workflow for (1) MS-based *in vitro* secretome analysis by using supernatants of cultured cells from both subtypes (classical and mesenchymal), performing cell free filtering, then MS detection of peptides. Differential peptide analysis is carried out to identify top secreted chemokines/cytokines per subtype. (2) *in vivo* CellChat communication analysis to infer intercellular communication networks using scRNA-seq data as input. Individual graphical elements by courtesy of Chiara Falcomatà.

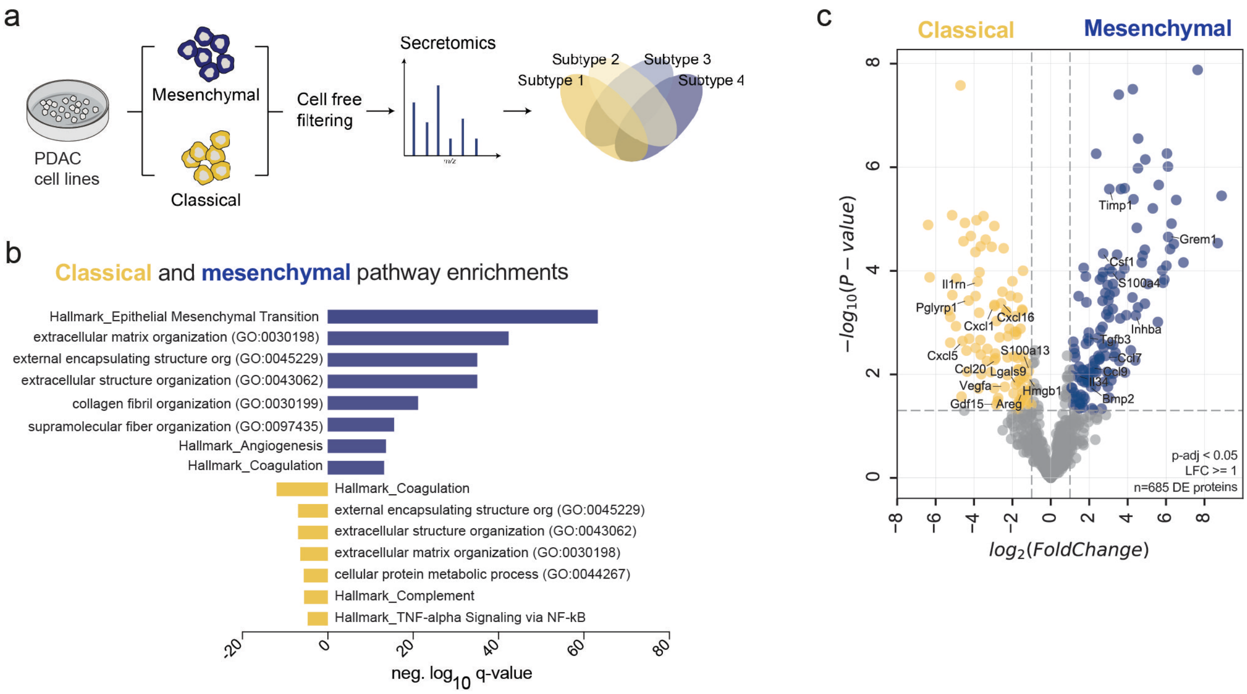

Figure 15. In vitro secretome analysis of classical and mesenchymal mouse PDAC cells reveals subtype-specific secreted factors

a, Schematic overview of experimental workflow for the MS-based secretomics approach: conditioned media was generated from classical and mesenchymal PK cell lines, supernatants were filtered and then subjected to MS-based secretomics analysis. Graphical elements by courtesy of Chiara Falcomatà.
b, GSEA analysis of enriched secreted proteins in classical versus mesenchymal cell lines. Top enriched terms from the HALLMARK and GO (Biological Process 2021) are depicted for both subtypes.
c, Differential testing between mesenchymal and classical secreted proteins was performed to identify top secreted factors per subtype. Volcano plot depicts statistically significant differentially secreted proteins (p-adj < 0.05 and LFC ≥ ±1). Top secreted proteins, which are annotated as chemokines/cytokines, are labelled in the plot. Collection of conditioned media was conducted together with Constantin Schmitt and Chiara Falcomatà. MS-based secretome analysis and data preprocessing was performed by Jonathan Swietlik (Meissner Lab).

As outlined, we first analyzed secretome data generated from *in vitro* cell cultures of both subtypes **(Figure 15a)**. After sample processing and mass spectrometry-aided peptide identification, our data set consisted of 4,348 proteins identified through this approach. To understand global differences between both subtypes, we performed gene set enrichment analysis. Mesenchymal tumor cells were enriched in multiple ECM terms, EMT and collagen organization, indicating that they secrete proteins involved in ECM production. For classical tumor cells, the top enriched term was coagulation. They were also enriched in some ECM gene sets, but to a much lower extent in comparison to mesenchymal tumor cells **(Figure 15b)**. Next, to identify enriched secreted proteins, a differential test between classical and mesenchymal samples was performed. As immune cell recruitment or proliferation is mostly mediated by chemokines and cytokines, we specifically focused on secreted proteins with a corresponding annotation as chemokines/cytokines (manually curated), which is highlighted in the volcano plot **(Figure 15c)**.

As a complimentary approach, we performed ligand-receptor interaction analysis between tumor cells and immune cells by leveraging our *in vivo* scRNA-seq data. Here, we used data for one classical (8442) and for one mesenchymal (9091) tumor line as these data sets exhibited the highest sequencing depth (> 150,000 reads per cell) to detect chemokine/cytokine expression in the tumor cell clusters.

The CellChat toolkit was used to infer the cell-cell communication network in both subtypes by identifying highly expressed ligands and their cognate receptor genes in two distinct cell types, followed by calculation of a communication probability for each specific interaction. This metric is based on the average gene expression of ligands by one cell type and receptors by another cell type and furthermore integrates prior knowledge of ligand-receptor interaction. CellChat analysis is supported by three databases with curated ligand-receptor pairs for secreted signaling, cell-cell contact signaling and ECM-receptor signaling. To identify relevant chemokines mediating crosstalk in the two PDAC subtypes, we chose to query the secreted signaling database. First, we analyzed the aggregated communication networks in both subtypes, by inferring the total number of interactions between cell types. Both subtypes show similar numbers of identified ligand-receptor interaction pairs (classical: 1575, mesenchymal: 1586 interactions), reflected in the overall interaction pattern as well **(Figure 16b)**. To address the first main question, namely which factors are secreted by classical versus mesenchymal tumor cells leading to recruitment of neutrophils (classical tumors) and macrophages (mesenchymal tumors), secretome and CellChat data were integrated and a comparative analysis to systematically identify top tumor cell-secreted factors was performed. We reasoned that factors emerging as shared candidates from both approaches would represent robust candidates and thus performed an overlap of secreted chemokines/cytokines from the secretome analysis and ligands expressed by tumor cells from the CellChat analysis. The intersection resulted in 15 secreted ligands for classical and 17 ligands for mesenchymal tumor cells **(Figure 16c, left panels)**. Next, ligands were assigned to signaling pathways according to the CellChat database. Classical tumor cells were enriched in CXCL chemokines and growth factor signaling related ligands, while in mesenchymal tumor cells ligands belonging to CSF and ACTIVIN/BMP/TGFb signaling were prominently identified. Then, each ligand was queried for their cell-cell interaction pattern to delineate factors which mediate signaling from tumor cells to either neutrophils or macrophages. For the interaction between classical tumor cells and neutrophils, two specific interactions pairs were identified: *Cxcl5-Cxcr2* and *Cxcl1-Cxcr2* which signal specifically between tumor cells and neutrophils. The third identified interaction pair was *Gdf15-Tgfbr2* which not only conveys signaling to neutrophils, but also to all tested cell types present in the tumor and therefore seems to mediate a broader communication pattern rather than specific tumor-neutrophil interaction. In contrast, query of mesenchymal tumors was directed towards ligands which mediate interactions from tumor cells to macrophages. As top selective interactions pairs, *Csf1-Csf1r* and *Il34-Csf1r* were identified.

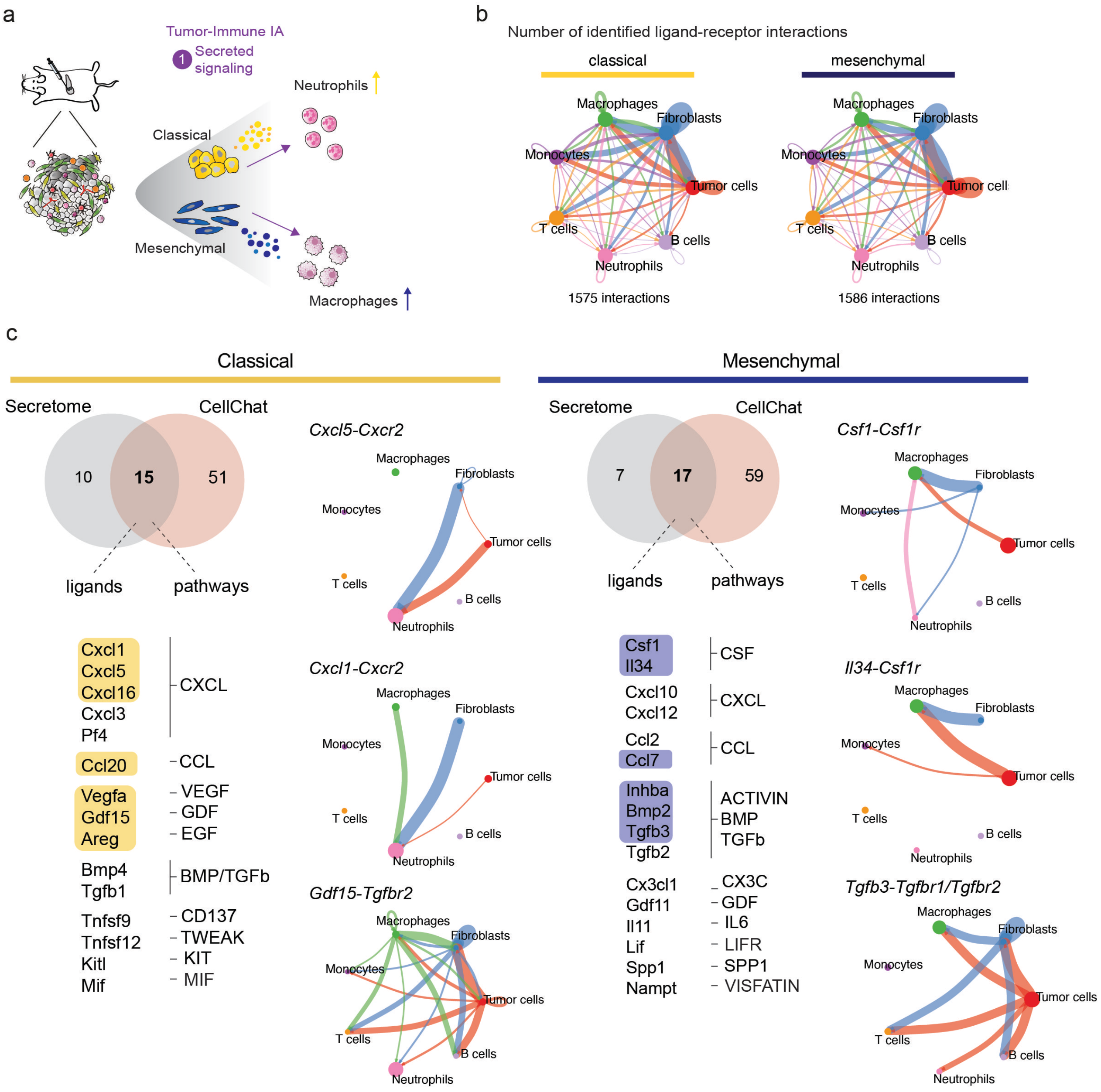

Figure 16. Cell-cell communication analysis integrating secretomics and CellChat to delineate tumor-immune crosstalk in PDAC subtypes

a, Schematic overview of proposed cell-cell communication model focusing on the tumor-immune interaction axis to identify differentially secreted factors in both subtypes. scRNA-seq data of two tumor lines (classical: 8442, mesenchymal: 9091) was integrated and cell-cell communication analysis performed using the CellChat toolkit. Individual graphical elements by courtesy of Chiara Falcomatà.
b, Circle plots show number of identified interactions from CellChat ligand-receptor interaction analysis for classical (left) and mesenchymal (right) tumors. The edge width between two cell type depicts the number of interactions between them.
c, Comparative analysis integrating secretome and CellChat analysis to identify top tumor cell secreted factors. Upper left panels show overlap of identified secreted chemokines/cytokines of secretome and CellChat analysis and overlapping ligands are depicted below. Ligands are then grouped into pathways and ligands which are either highlighted in yellow or blue were significantly enriched in the secretome analysis. Right side of each panel, Circle plots for selected ligand receptor interaction pairs in classical (left) and mesenchymal (right) tumors. Edge width between two cell types shows cell communication probability. The size of the cell type circles is proportional to the number of cells in these groups.

Similar to the classical tumor, the third ligand (*Tgfb3-Tgfbr1/Tgfbr2)* showed no specific tumor-macrophage interaction, instead mediating signaling to multiple other cell types of the TME **(Figure 16c, right panels)**. Notably, the two top identified ligands per tumor subtype are predicted to signal to the same receptor: *Cxcr2* in the classical tumor and *Csf1r* in the mesenchymal tumor TME.

As CXCL/CSF/CCL signaling was enriched in both subtypes, we further analyzed ligand-receptor interactions with tumor cells as the source of the signal and compared both subtypes side-by-side **(Figure 17a)**. This analysis revealed *Cxcl5-Cxcr2* for classical and *Csf1-Csf1r* for mesenchymal tumors as significant interaction pairs with the highest communication probabilities that are specific to their respective subtype **(Figure 17a and c/d)**.

Interestingly, *Cxcl1-Cxcr2* and *Il34-Csf1r* did not display exclusivity for the respective subtype, a phenomenon also accompanied by lower communication probabilities. Albeit *Il34-Csf1r* showed the highest communication probability for the interaction from mesenchymal tumor cells to macrophages, communication probabilities were also computed from classical tumor cells to macrophages/monocytes and, interestingly, for the interaction classical tumor cells – neutrophils, although to a much lower extent. The *Cxcl1-Cxcr2* signaling was likewise not exclusive to classical tumor cells and neutrophils, but also present in the mesenchymal tumor **(Figure 17a)**. It can be hypothesized that macrophage and neutrophil recruitment in the two PDAC subtypes is primarily mediated by Csf1 and Cxcl5, respectively, with a potential contribution from Il34 and Cxcl1, possibly acting in a synergistic fashion. Interestingly, also interactions between tumor cells and T cells via CXCL chemokines were inferred in this analysis. *Cxcl12-Cxcr4* was a specific tumor – T cell interaction in the mesenchymal subtype, but Cxcl12 was not significantly secreted in the secretome analysis. In the classical tumor cells, Cxcl16 was identified as significant differentially secreted protein in classical tumor cells and showed a higher interaction strength in the CellChat analysis between tumor cells and T cells than the mesenchymal subtype (**Figure 16c and 17a)**. In PDAC, CXCL16 was previously described as contributor of tumor progression and invasiveness and CXCL16-CXCR6 signaling was also reported to be important for adhesion of lymphocytes (Lesch et al., 2021; Wente et al., 2008). In addition to the tumor cell mediated signaling, we observed that *Cxcl5/Cxcl1* and *Csf1/Il34* is engaged by fibroblasts with a high communication probability. Therefore, we visualized the ligand-receptor interactions for CXCL and CSF signaling in chord diagrams with tumor cells and fibroblasts as source cell types comparing both subtypes **(Figure 17b)**.

This approach revealed that fibroblasts interact via *Cxcl5/Cxcl1* and *Csf1/Il34* with neutrophils and macrophages, respectively, with a higher interaction strength than the corresponding tumor cells. Since these fibroblast interaction patterns are similar in classical and mesenchymal tumors, we hypothesize that the high difference in infiltrating macrophages and neutrophils stems from the signaling mediated by the tumor cell compartment, an assumption that needs further functional validation.

In conclusion, we identified *Cxcl5* in the classical and *Csf1* in the mesenchymal subtype as tumor cell secreted factors with the highest communication probability mediating recruitment of neutrophils and macrophages, respectively, into the TME **(Figure 17c/d)**. This comparative analysis also highlights the power of integrating protein (secretome) with RNA (scRNA-seq) expression to infer cell-cell communication networks with high confidence.

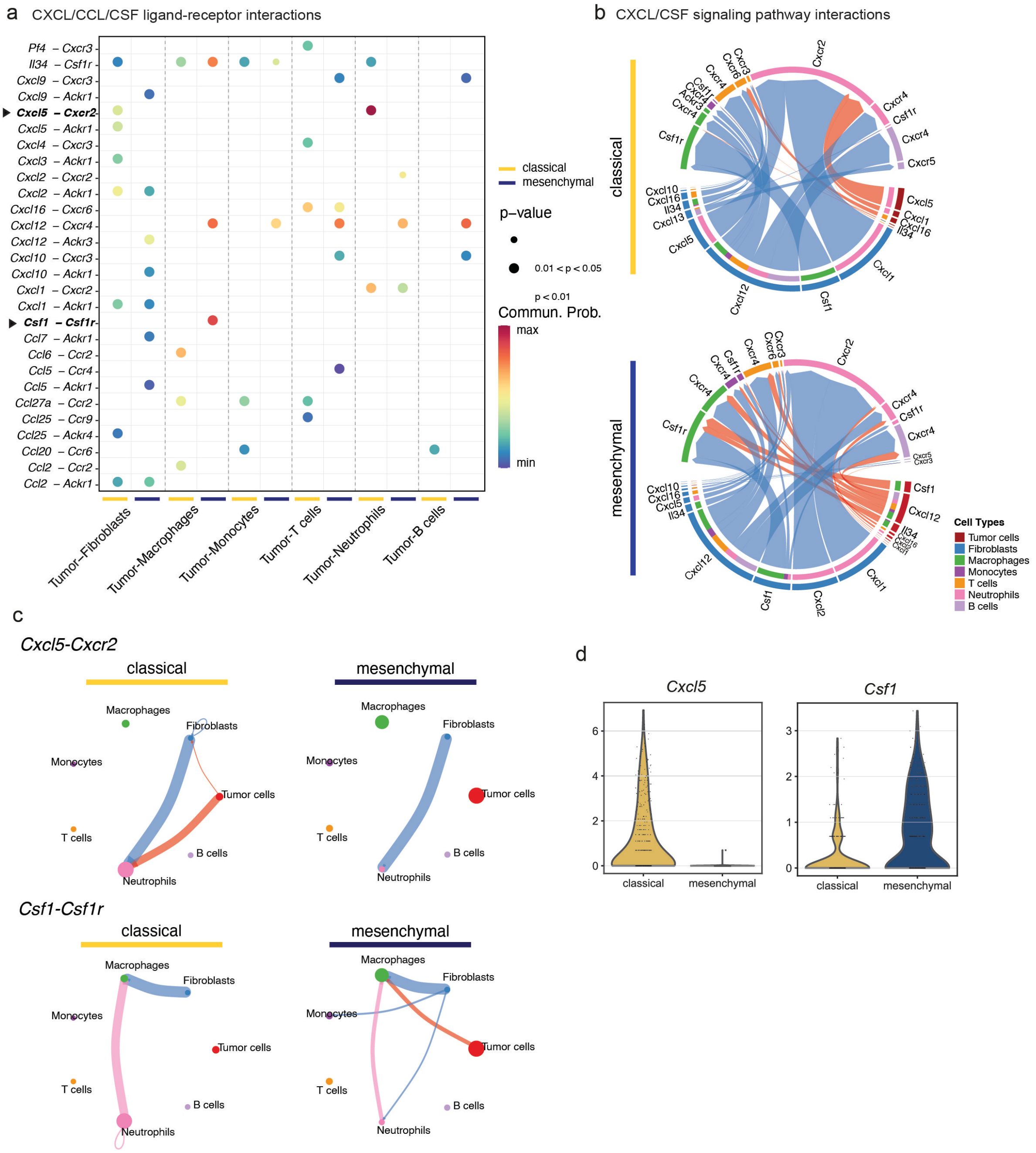

Figure 17. Cell-cell communication to myeloid cells is mediated by Cxcl5 in classical and Csf1 in mesenchymal tumor cells

a, Comparison of significant tumor-immune interactions between classical and mesenchymal tumors. Bubble plot depicts identified ligand-receptor pairs (belonging to CXCL/CCL/CSF signaling pathways) for both subtypes mediating interactions from tumor cells (source) to other TME cell types and. Color of dots visualizes communication probability and dot size represents computed *p*-values from a one-sided permutation test. Empty spaces denote that communication probability is zero for this specific interaction.
b, Chord diagrams visualizing the ligand-receptor interactions of CXCL/CSF signaling pathways for source cell types (tumor cells and fibroblasts) and target cell types (neutrophils, macrophages, monocytes, T and B cells). Edge width between two cell types is proportional to the cell communication probability. The inner bar circle shows the target cells which receive signaling from the source cells via a specific ligand.
c, Circle plots for *Cxcl5-Cxcr2* (upper panel) and *Csf1-Csf1r* (lower panel) comparing their signaling interactions in both subtypes. Edge width between two cell types shows cell communication probability. The size of the cell type circles is proportional to the number of cells in these groups.
d, Violin plots depicting expression of *Cxcl5* and *Csf1* in tumor cells comparing both subtypes.

The next main question that was posed was to interrogate how macrophages and neutrophils communicate with T cells, thereby potentially mediating T cell exhaustion and suppression. To this end, we extended our CellChat analysis by implementing the cell-cell contact database and analyzed cell-cell contact signaling specifically between macrophages – T cells and neutrophils – T cells, using our full scRNA-seq data set presented in Figure 9 **(Figure 18a)**. First, cell-cell contact signaling pathways were globally compared between classical and mesenchymal tumors. In mesenchymal tumors, several inhibitory immune checkpoint signaling pathways, such as PD-L1, PD-L2, PVR and TIGIT signaling, as well as MHC I and II signaling were enriched compared to classical tumors (**Figure 18b).** We decided to further focus on PD-L1 and MHC signaling as PD-1/PD-L1 inhibitors play a major role in cancer immunotherapy, further warranting detailed exploration of subtype-specific differences in the PD-L1 cell-cell communication network (Brahmer et al., 2012; Waldman et al., 2020). MHC signaling plays a fundamental role in T cell activation and, by using CellChat, we determined differences in antigen-presentation between subtypes. In both subtypes, we did not detect interaction originating from tumor cells via PD-L1 signaling, but instead noted differences in the other TME cell types. In classical tumors, while PD-L1 signaling from neutrophils to CD8$^+$ T cells showed the highest interaction strength, minor communication probabilities were detected that emerged from NK cells, dendritic cells and macrophages/monocytes **(Figure 18c, left)**. In contrast, dendritic cells and macrophages/monocytes displayed the highest interactions strengths when signaling to CD8$^+$ T cells via PD-L1 in the mesenchymal subtype. This suggests that mesenchymal PDAC could benefit more from PD-1/PD-L1 immune checkpoint blockade and indeed, we could previously show clinical benefit specific to the mesenchymal subtype in an *in vivo* treatment study, when a combination of targeted therapy with anti-PD-L1 treatment was administered (Falcomatà et al., 2022).

Next, we analyzed MHC-I signaling which is important for signaling to CD8$^+$ T cells (Hennecke and Wiley, 2001; Neefjes et al., 2011). Overall, MHC-I signaling displayed higher interaction strengths in the mesenchymal tumors compared to classical cancers across all immune cell types as well as tumor cells and fibroblasts, suggestive of a generally higher antigen-presentation in this subtype. MHC-II signaling (which is important for CD4$^+$ T cell activation) was mostly mediated by macrophages, dendritic cells and B cells, and displayed higher interaction strength in the mesenchymal subtype akin to MHC-I signaling **(Figure 18d and e)**. In summary, the mesenchymal subtype is characterized by higher antigen-presentation and amplified inhibitory PD-L1-signaling compared to the classical subtype.

Our subsequent analysis focused on cell-cell contact signaling between macrophages or neutrophils and CD4$^+$/CD8$^+$ T cells, allowing inference of significantly enriched ligand-receptor interaction pairs through comparison of both subtypes. First, the enriched ligand-receptor

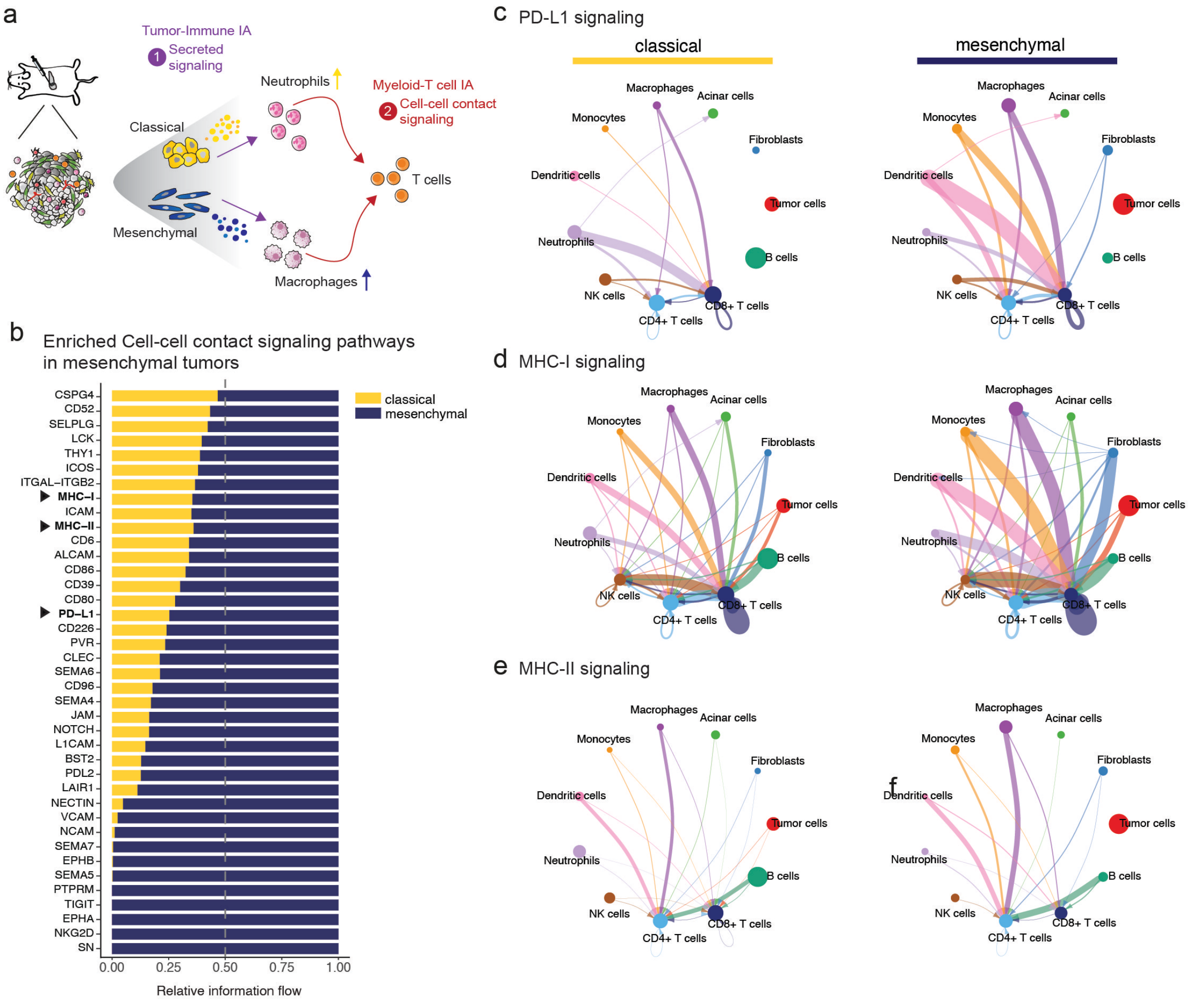

Figure 18. Myeloid-T cell interaction analysis reveals subtype-specific cell-cell contact signaling

a, Schematic overview of proposed cell-cell communication model focusing on the myeloid cell-T cell communication axis. This model has implications to pinpoint cell-cell contact signaling enriched in both subtypes and ligand-receptor interactions potentially mediating T cell suppression. The full scRNA-seq data set from Figure 9 was used as input for the analysis. Individual graphical elements by courtesy of Chiara Falcomatà.
b, Bar plots displays significantly enriched signaling pathways in the mesenchymal versus classical subtype. Significant pathways were ranked based on differences in information flow between the two subtypes, which is calculated by summarizing all communication probabilities of the interactions within the respective signaling network.
c, Circle plots for PD-L1 signaling comparing these signaling interactions in both subtypes. Edge width between two cell types shows cell communication probability. The size of the cell type circles is proportional to the number of cells in these groups.
d, Circle plots for MHC-I signaling comparing these signaling interactions in both subtypes.
e, Circle plots for MHC-II signaling comparing these signaling interactions in both subtypes.

interactions in the mesenchymal tumors that mediate signaling from macrophages to CD4$^+$/CD8$^+$ T cells were identified. In total, we detected 51 interaction pairs, which were enriched in the mesenchymal tumors compared to the classical tumors. Interestingly, many of those interactions were also present in the classical tumors, but with partly lower communication probabilities.

While most identified ligand-receptor interaction pairs were associated with MHC signaling, *H2-k1–Cd8a* and *H2-d1–Cd8a* were identified with highest interaction strengths between macrophages and CD8$^+$ T cells in the mesenchymal subtype. Other interaction pairs could be associated to ICOS and NOTCH signaling as well as immune checkpoints, such as *Cd274-Pdcd1*, *Cd86-Ctla4* and *Pvr-Tigit*, which showed lower communication probabilities compared to the MHC interactions **(Figure 19a)**.

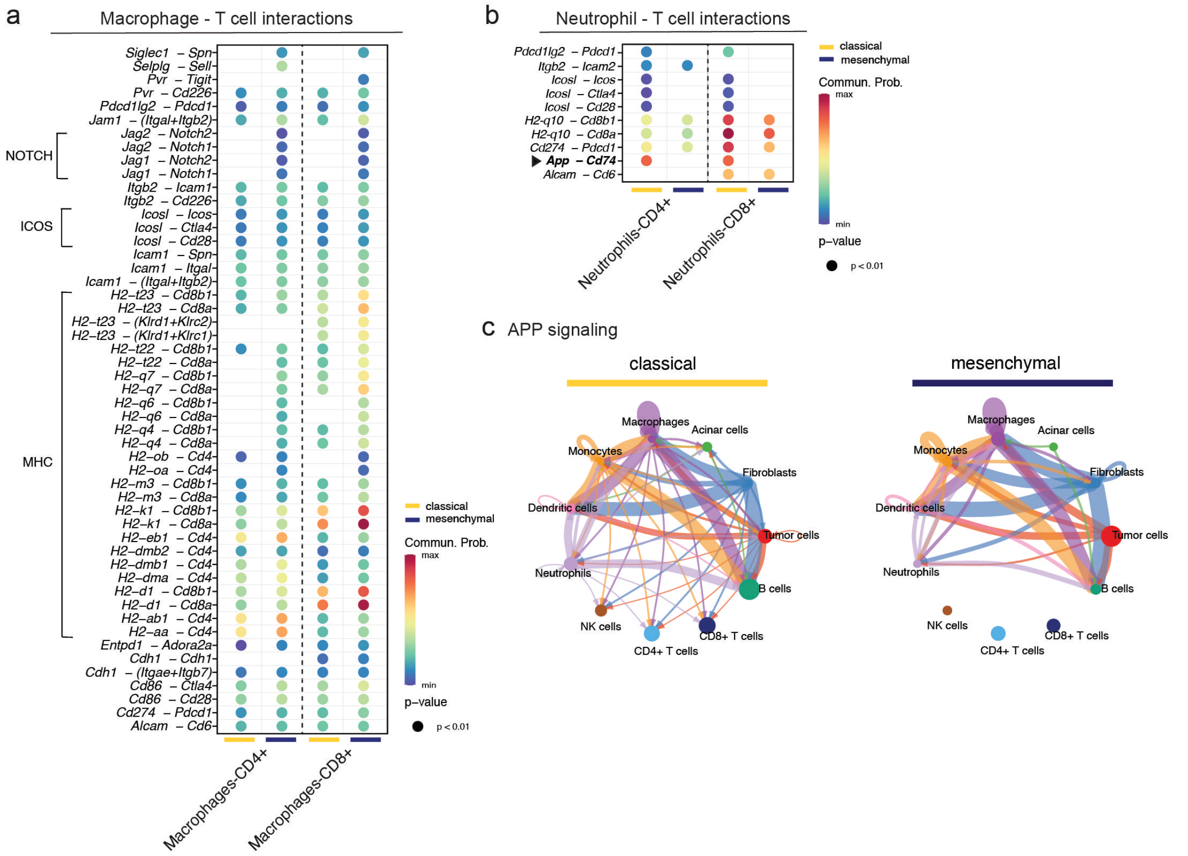

Figure 19. Comparison of myeloid – T cell cell-cell communication in classical and mesenchymal tumors

a, Bubble plot displays significant identified ligand-receptor interaction pairs between macrophages and CD4$^+$/CD8$^+$ T cells, which are enriched in the mesenchymal subtype. Ligand-receptor interactions are grouped into signaling pathways. Color of dots visualizes communication probability and dot size represents computed *p*-values from a one-sided permutation test. Empty spaces mean that communication probability is zero for this specific interaction.
b, Bubble plot displays significant identified ligand-receptor interaction pairs between neutrophils and CD4$^+$/CD8$^+$ T cells, which are enriched in the classical subtype. Color of dots visualizes communication probability and dot size represents computed *p*-values from a one-sided permutation test. Empty spaces mean that communication probability is zero for this specific interaction.
c, Circle plots for APP signaling comparing these signaling interactions in both subtypes. Edge width between two cell types shows cell communication probability. The size of the cell type circles is proportional to the number of cells in these groups.

As a result, interactions between macrophages and CD4$^+$/CD8$^+$ T cells are alike in both subtypes, even though macrophages are more abundant in the mesenchymal tumors as shown in the analyses before.

Secondly, interactions between neutrophils and CD4$^+$/CD8$^+$ T cells were analyzed for cell-cell contact signaling, focusing on those ligand-receptor interaction pairs which are enriched in the classical compared to mesenchymal subtype. Here, a smaller number of significant interactions (n=10) was detected, but six of these interaction pairs were exclusive to the classical subtype. Among these, *App-Cd74* displayed the highest communication probability **(Figure 19b)**. Interestingly, while APP signaling does not engage in any interactions towards CD4$^+$/CD8$^+$ T cells in the mesenchymal tumors, it does so in the classical subtype **(Figure 19c)**. Therefore, *App* could be an interesting factor for further functional validation. PD-L1 signaling mediated by *Cd274-Pdcd1* similarly displayed a higher communication probability in the classical compared to the mesenchymal subtype for neutrophil – CD8$^+$ T cell interactions and *Pdcd1lg2-Pdcd1* interaction was only present in the classical tumors.

In conclusion, mesenchymal tumors showed increased signaling via PD-L1 and MHC ligand-receptor interactions to mediate cell-cell communication towards T cells which is an attractive option for designing new treatment rationales including immunotherapies.

In a complimentary approach, interactions between myeloid cells and CD4$^+$/CD8$^+$ T cells were investigated for secreted signaling following the same analysis workflow as for the cell-cell contact signaling **(Figure 20a)**. First, secreted signaling interactions between neutrophils and CD4$^+$/CD8$^+$ T cells were inferred, focusing again on ligand-receptor pairs which are enriched in the classical subtype. In total, 13 interaction pairs were identified in the classical tumors, with *Mif – (Cd74+Cd44)* presenting a specific interaction between neutrophils and CD8$^+$ T cells and showing the highest communication probability of all inferred interaction pairs **(Figure 20b)**. Interestingly, *Mif* is described to be widely expressed by multiple innate and adaptive immune cell types and is also known to inhibit T cell activation by inducing activation-induced T cell death (Noe and Mitchell, 2020). Interestingly, *Mif – (Cd74+Cd44)* signaling to CD8$^+$ T cells was the only interaction towards T cells via *Mif* in the classical subtype. In the mesenchymal tumors, there were no *Mif* interactions with T cells observed **(Figure 20c)**. This makes *Mif* an interesting vulnerability for further follow-up. It can also be noted that only three out of 13 identified neutrophil – T cell interactions are shared by both subtypes, the remaining ligand-receptor interactions are exclusively inferred in the classical subtype **(Figure 20b)**.

Next, macrophage - CD4$^+$/CD8$^+$ T cell signaling via secreted factors was analyzed and 28 ligand-receptor interaction pairs were inferred as enriched in the mesenchymal subtype **(Figure 20d)**. Although not exclusive, *Cxcl16-Cxcr6* siganling from macrophages to CD8$^+$ T cells displayed one of the highest communication probabilities in the mesenchymal tumors. In contrast, we identified Cxcl16 as differentially secreted factor enriched in the classical PDAC cell lines in our previous secretome analysis in **Figure 15b**. *Cxcl16* interactions towards CD8$^+$ T cells are additionally outgoing from dendritic cells (both subtypes) and monocytes (mesenchymal subtypes), which also display high communication probabilities **(Figure 20e)**.

Other macrophage – T cell interactions with high interaction strengths were mediated by *Spp1* and *Lgals9*, but these are widely present in all immune cell types and therefore we did not investigate them further. To this end, both subtypes show a specific secreted signaling communication network in terms of myeloid – T cell interactions.

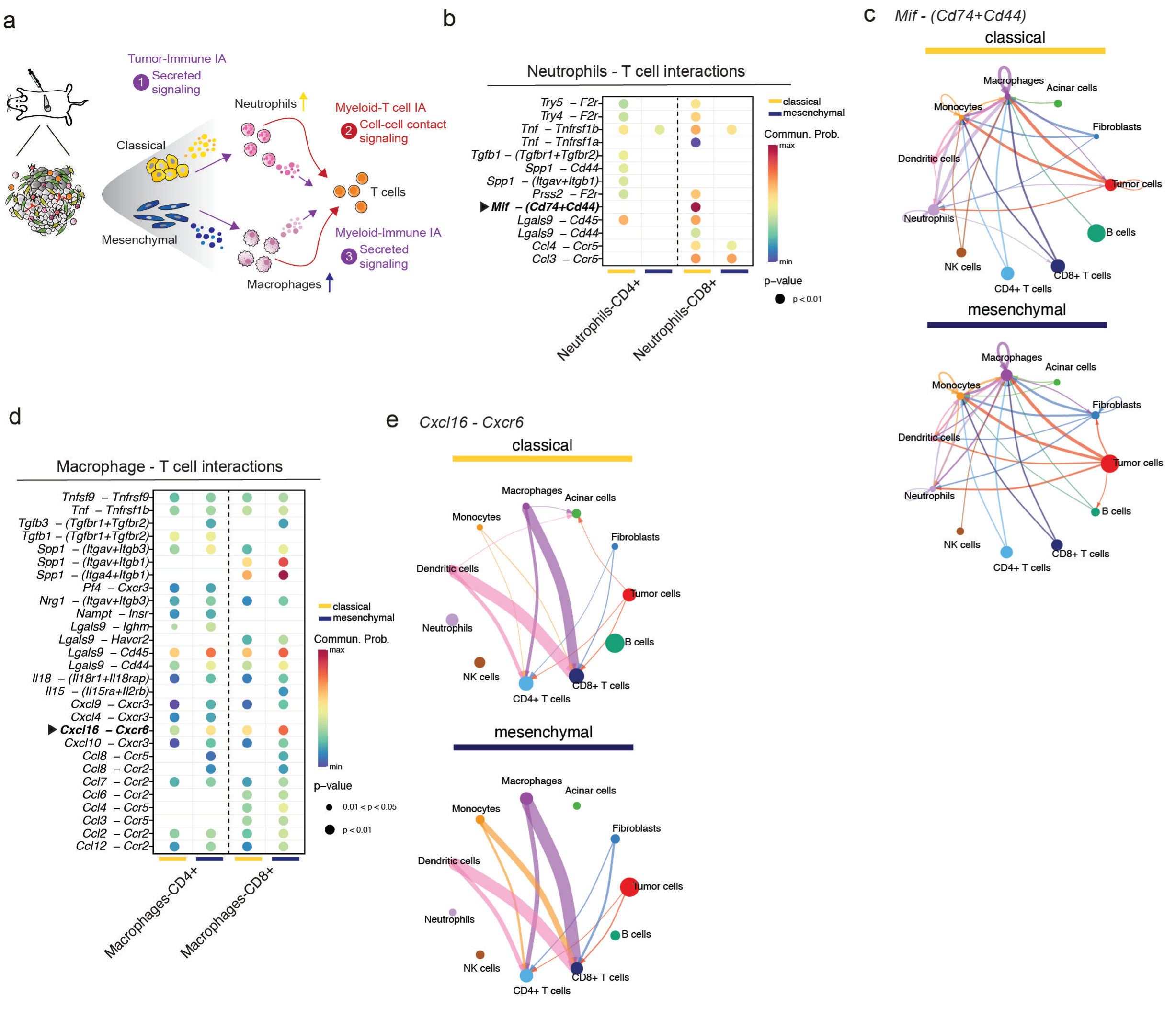

Figure 20. Cell-cell communication analysis of secreted signaling between myeloid cells and T cells in classical and mesenchymal tumors

a, Schematic overview of proposed cell-cell communication model focusing on the myeloid cell-T cell communication axis. This model has implications to pinpoint secreted signaling enriched in both subtypes and ligand-receptor interactions potentially mediating T cell suppression. The full scRNA-seq data set from Figure 9 was used as input for the analysis. Individual graphical elements by courtesy of Chiara Falcomatà.
b, Bubble plot displays significant identified ligand-receptor interaction pairs between neutrophils and $CD4^{+}/CD8^{+}$ T cells, which are enriched in the mesenchymal subtype. Color of dots visualizes communication probability and dot size represents computed *p*-values from a one-sided permutation test. Empty spaces mean that communication probability is zero for this specific interaction.
c, Circle plots for ligand-receptor interaction *Mif – (Cd74+Cd77)* signaling comparing these signaling interaction in both subtypes. Edge width between two cell types shows cell communication probability. The size of the cell type circles is proportional to the number of cells in these groups.
d, Bubble plot displays significant identified ligand-receptor interaction pairs between neutrophils and $CD4^{+}/CD8^{+}$ T cells, which are enriched in the classical subtype. Color of dots visualizes communication probability and dot size represents computed *p*-values from a one-sided permutation test. Empty spaces mean that communication probability is zero for this specific interaction.
e, Circle plots for ligand-receptor interaction *Cxcl6 – Cxcr6* signaling comparing these signaling interaction in both subtypes. Edge width between two cell types shows cell communication probability. The size of the cell type circles is proportional to the number of cells in these groups.

4.5. Conclusion

To design more effective treatment strategies, it is crucial to understand the tumor ecosystem in all aspects. In this study, we performed a comprehensive TME characterization of the clinically relevant classical and mesenchymal PDAC subtype to unravel the TME composition and cell-cell communication networks. The classical and mesenchymal subtype differed substantially in their immune infiltrates, with the greatest difference in myeloid cell infiltration. Albeit these differences in composition, both subtypes are T cell excluded. We delineate with the cell-cell communication analysis that T cell suppression is mostly mediated via immune cell crosstalk and to a lower extent by direct tumor – T cell interactions **(Figure 21)**.

Overall, this study proposes a refined PDAC subtype cell-cell communication network highlighting potential therapeutic vulnerabilities for targeting the PDAC TME:

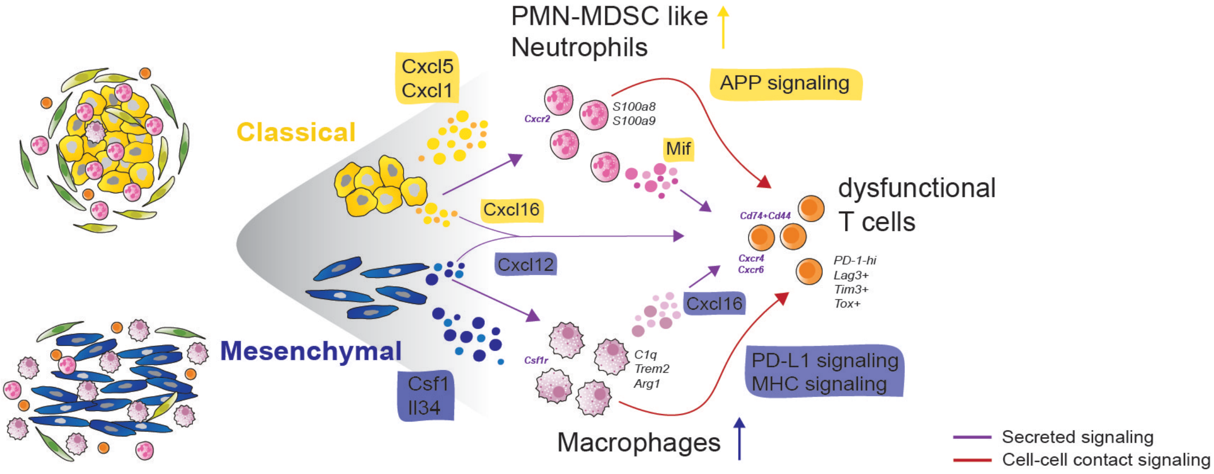

Figure 21: Summary of subtype-specific TME characteristics and resolved cell-cell communication network

Schematic overview presents TME characteristics, with focus on immune infiltration, derived from our multimodal TME analysis. Tumor cells mediate immune cell recruitment via secreted signaling. Namely, classical tumor cells secrete Cxcl5 and Cxcl1, which signal to the Cxcr2 receptor, thereby recruiting neutrophils, which display a PMN-MDSC-like phenotype. These MDSC-like cells signal to T cell via secreted (through Mif secretion) and App signaling (cell-cell contact), potentially mediating T cell suppression and exhaustion.

In contrast, mesenchymal tumor cells secrete Csf1 and Il34, which mediate recruitment and proliferation of immunosuppressive *Arg1*$^{+}$*Trem2*$^{+}$ macrophages. These engage in turn with T cells via PD-L1/MHC signaling as well as by secretion of Cxcl16, contributing to the dysfunctional T cell compartment. Tumor cells also directly interact with T cells via secretion of Cxcl16 in classical tumors and Cxcl12 in mesenchymal tumors.

5. DISCUSSION

PDAC is a dismal disease presenting a complex genetic landscape and heterogenous TME. Moreover, PDAC belongs to one of the most lethal cancer entities and is projected to become the second leading cause of cancer-related mortality by 2030 (Rahib et al., 2014; Siegel et al., 2022). Among the hallmarks of cancer, which were first postulated by Hanahan and Weinberg in 2011, is the ability of transformed cells to avoid immune destruction (Hanahan, 2022; Hanahan and Weinberg, 2011). Following this hypothesis, extensive research efforts in the last decade have invoked the characterization of the PDAC TME and mechanisms of immune evasion. At the same time, the wide applicability of next-generation sequencing (NGS) studies fueled the molecular characterization of PDAC patient cohorts to decipher the genetic landscape and phenotypes of PDAC. Comprehensive efforts led by Collisson, Moffitt and Bailey revealed transcriptional subtypes of PDAC which are associated with prognosis and treatment outcome. Classical and mesenchymal PDAC emerged as the two major subtypes (Bailey et al., 2016; Collisson et al., 2011; Moffitt et al., 2015). One intriguing question arising from these molecular classifiers is how these PDAC subtypes are connected to the immunosuppressive phenotype of the PDAC TME and in which way they shape their specific TME. Systematic analysis of the TME composition in PDAC subtypes was not conducted so far and thus molecular drivers of immunosuppression remained elusive.

To tackle this issue, we delineated the TME composition and cell-cell communication networks in the two major transcriptional PDAC subtypes in this study by utilization a multimodal analysis approach. Importantly, we analyzed the TME composition at high-resolution using flow cytometry and scRNA-seq, thereby considering the heterogeneity of immune cell types, as well as taking the spatial variability of these cell types into account by deploying spatial transcriptomics analyses. Through integration of secretomics with scRNA-seq data, we inferred the subtype-specific cell-cell communication networks and interrogated distinct modes towards immunosuppression in PDAC subtypes. Our work opens new possibilities for identifying therapeutic vulnerabilities or designing combinatorial therapies targeting PDAC subtypes and their immunosuppressive TME.

5.1. TME phenotypes and heterogeneity in PDAC

With the advent of high-resolution scRNA-seq approaches, detailed study of the TME composition at the single cell level became feasible. This opened new avenues in investigating the complex heterogeneity of tissue architectures, such as delineation of organ cell type composition in development or adulthood (Pijuan-Sala et al., 2019; Tabula Muris et al., 2018). Considering cancer research, scRNA-seq has helped to elucidate distinct stromal and immune cell types in the PDAC

TME as multiple studies investigated the cellular diversity previously in mouse and human PDAC (Giladi and Amit, 2018; Han et al., 2021; Sun et al., 2021) .

In the study presented here, we delineated first TME phenotypes in a large histological cohort of PDAC GEMMs reflecting the genetic complexity of the human disease. Of note, while individual genetic alterations influence TME composition, significant heterogeneity within each genotype group was observed. Five distinct TME phenotypes were identified and annotated as enriched in lymphocytes, granulocytes, proliferating cells and stroma content as well as one cluster named as immune excluded, which was devoid of immune cells. One drawback of this analysis was the source material being H&E-stained FFPE tissue sections, thus preventing identification of specific cell types other than lymphocytes and granulocytes. Liudahl et al performed a multiplexed immunohistochemistry analysis on FFPE PDAC sections from 135 patient specimens, enabling the precise description of specific cell populations and functional states. In total, 17 distinct cell types including epithelial cells, multiple T cell populations, B cells, neutrophils, macrophages, mast cells and dendritic cell subsets could be identified. Similarly, distinct functional states, such as proliferation, cytotoxicity and immunoregulation were described. Analysis of treatment-naïve PDAC revealed three main TME phenotypes, namely the hypo-inflamed, myeloid and lymphoid TME, which were partly overlapping with our histopathological analysis. Moreover, the spatial distribution of these cell types throughout different tumor regions, e.g. invasive tumor, tumor adjacent stroma and adjacent normal tissue, was analyzed. Among the cell types showing distinct spatial variability over different tumor regions were neutrophils and CD8$^+$ T cells. The former were highly accumulating in areas near tumor cells, while the latter were excluded from those areas, but could be found outside tumor regions (Liudahl et al., 2021). These findings corroborate the results from our spatial transcriptomics analysis, in which close proximity between neutrophils and classical tumor cells was observed to a similar extent, in contrast to T cells showing sparse infiltration and a dispersed occurrence in the stroma regions of mouse PDAC.

5.2. Subtype-specific TME characteristics

An inherent advantage of orthotopic implantation models in cancer research is the ability to characterize cells prior to implantation, thus obtaining insight into molecular pathomechanisms of disease subtypes. In this study, we deployed an orthotopic allograft model to investigate tumors allocated to a defined subtype state and showing distinct molecular features. As model system, we orthotopically implanted mouse PDAC cell lines with an extensively history of molecular characterization (Falcomatà et al., 2022; Mueller et al., 2018). Importantly, the phenotype of these subtypes is stable *in vivo* and faithfully recapitulated in our implantation models. In this work, we analyzed the most pronounced phenotypic states of PDAC subtypes, by comparing the most classical versus the most mesenchymal subtypes. These are typically characterized by a pure classical or mesenchymal gene expression signature and morphological phenotype. Although a recent research study showed the existence of an intermediate co-expressor subtype, presenting as a transitional state between classical and mesenchymal, profound knowledge of either classical or mesenchymal cells on immune cells recruitment in PDAC is of utmost importance to stratify patients into clinically actionable cohorts (Raghavan et al., 2021). The TME characteristics of this intermediate subtype need to be systematically addressed in further studies.

Moreover, TME properties of PDAC subtypes were also analyzed in bulk RNA-sequencing cohorts and were previously associated to distinct gene expression signatures (Maurer et al., 2019; Puleo et al., 2018). The structural TME in classical PDAC is characterized by a high abundance of activated CAFs and a dense desmoplastic stroma, but low in tumor cellularity. In contrast, the mesenchymal subtype shows lower extent of stroma and a higher tumor cell fraction (Steins et al., 2020). Notably, mesenchymal/ECM-rich tumors were associated with the poorest survival in comparison to classical/immune-rich tumors (Maurer et al., 2019). In their comprehensive analysis of intratumor TME heterogeneity, Grünwald et al identified the reactive, deserted and intermediate TME state, which can co-occur within the same tumor, warranting the annotation as subTMEs. Importantly, these subTMEs were associated with PDAC subtypes defined by the transcriptional profile of tumor cells. Focusing their analysis on the malignant cells, the authors showed that the dominant reactive subTMEs displayed enrichment of mesenchymal tumor cells, distinguished by proliferative and mesenchymal gene expression signatures, while classical PDAC showed a lower frequency of dominant deserted TMEs. Conversely, the dominant deserted TMEs showed histologically more well-differentiated glandular tumor structures and were positively correlated with a better patient outcome (Grünwald et al., 2021).

In this study, we focused on the investigation of the immune TME subtype-specific differences as these have not been systematically analyzed so far. While our data supports the notion that both PDAC subtypes show sparse infiltration of T cells and a dysfunctional T cell compartment, the most striking difference was found in the myeloid compartment. Classical tumors were infiltrated by high fractions of activated PMN-MDSC like neutrophils, while mesenchymal tumors displayed high abundance of immunosuppressive *Arg1*$^{+}$*/Trem2*$^{+}$ macrophages. Only few recent studies focused on specific cell lineages of the immune TME in PDAC subtypes. Our findings of high macrophage infiltration in the mesenchymal subtype are corroborated by a study from Tu et al in which the authors found that TNFα expressing macrophages are recruited by CCL2 secretion from mesenchymal tumor cells, which is secreted from tumor cells and regulated via BRD4-mediated cJUN/AP1 expression. Conversely, regulatory elements of the CCL2 locus were not active in classical PDAC cells, determined by absence of cJUN binding to the corresponding enhancer. TNFα, secreted by macrophages in mesenchymal PDAC, was furthermore found to maintain the aggressive mesenchymal subtype through downregulation of lineage-specific classical differentiation genes (Tu et al., 2021). This study also highlights tumor cell intrinsic mediation of secreted factors as potential therapeutic vulnerability to inhibit infiltration of immunosuppressive macrophages. In another study, patient-derived PDAC liver metastasis samples were subjected to scRNA-seq analysis and subsequent subtype-stratification. Additional to the classical and mesenchymal subtype classification, an intermediate co-expressor state was identified which exhibits shared gene expression originating from both classical and mesenchymal signatures. These refined subtypes were associated with TME compositions. Notably, the mesenchymal state was associated with a high abundance of *C1QC*$^{+}$ macrophages and generally a lower TME cell type diversity (Raghavan et al., 2021).

Modulation of the PDAC TME can furthermore lead to differences in therapeutic responses. Our recent findings show that a novel combinatorial targeted therapy elicits significant response in the therapy-refractory mesenchymal subtype. The combined kinase-targeted therapy induced a remodeling of the TME *in vivo* and led to a higher infiltration of effector T cells, specifically in the mesenchymal subtype. Thus, this subtype was more receptive for PD-L1 checkpoint inhibition, contrasting the classical subtype where we could not detect this T cell influx (Falcomatà et al., 2022).

5.3. Subtype-specific cell-cell communication networks and therapeutic vulnerabilities

The differences in the TME composition in classical and mesenchymal PDAC led us to hypothesize that these subtypes also differ in their cell-cell communication networks. Understanding the cell-cell communication relationships between the diverse cell types within a tumor is crucial for identifying therapeutic vulnerabilities as a rising number of biologics is achieving FDA approval, thus positioning elimination of chemokine-mediated cell communication through antibody administration as a powerful treatment regimen (Mullard, 2021). To understand these communication networks in PDAC subtypes, we propose a cell-cell communication model where we delineate (i) how tumor-cell intrinsic properties influence immune cell recruitment and (ii) how immune cells communicate with each other to shape an immunosuppressive PDAC TME.

5.3.1. Tumor-immune crosstalk in PDAC

It is known that the genetic landscape of a tumor can influence the immune composition, but these complex genotype-phenotype relationships remain to be fully understood (Binnewies et al., 2018; Wellenstein and de Visser, 2018). As an example, it was reported that *KRAS*^{G12D}-driven PDAC cells secrete GM-CSF (CSF2) which correlated with an infiltration of Gr1^{+}CD11b^{+} myeloid cells (Bayne et al., 2012; Pylayeva-Gupta et al., 2012). Similarly, PDAC tumors with a high FAK activity were associated with increased levels of fibrosis and low infiltration of CD8^{+} T cell infiltration (Jiang et al., 2016). In another study of *Kras*^{G12D}-driven PDAC, higher infiltration of immunosuppressive CD11b^{+} myeloid cells and regulatory T cells was dependent on additional loss of p53 in the tumor cells. Furthermore, these malignant cells were also shown to secrete multiple cytokines and chemokines (e.g. Csf1, Mcp1, Cxcl10 and Cxcl1) important for myeloid cell recruitment at higher levels (Blagih et al., 2020). Particularly, cytokines and chemokines are crucial mediators of immune cell trafficking and cell-cell interactions in cancer (Nagarsheth et al., 2017; Ozga et al., 2021). In our study, we identified multiple cytokines/chemokines which differ in secretion levels between classical and mesenchymal PDAC by integrating an *in vitro* secretome analysis with an *in vivo* scRNA-seq ligand-receptor interaction analysis (CellChat). As top differentially secreted factors, Csf1 (mesenchymal PDAC) and Cxcl5 (classical PDAC) emerged. The Csf1/Csf1r signaling axis plays a central role in differentiation, proliferation and chemotaxis of macrophages and is thus an attractive therapeutic target to inhibit accumulation of immunosuppressive macrophages (Pathria et al., 2019; Stanley and Chitu, 2014). *CSF1R*-expressing macrophages were associated with a poor prognosis and could be linked to the squamous and immunogenic PDAC subtypes in patients (Bailey et al., 2016; Candido et al., 2018). Using a small-molecule CSF1R inhibitor, which inhibits CSF1R phosphorylation, led to a significant reduction of macrophages and a reduced tumor mass in a PDAC mouse model (PKP genotype). In addition, CSF1R inhibition increased $CD4^+$ and $CD8^+$ T cell infiltration, suggesting TME reprogramming to an immune-infiltrated TME (Candido et al., 2018). In contrast, Kumar et al tested CSF1R inhibition in implantation models of different tumor entities, such as melanoma, lung cancer and breast carcinoma, and described higher infiltration of PMN-MDSC granulocytes upon treatment. Further analysis revealed that CAFs upregulated chemokines important for granulocyte recruitment upon CSF1R inhibition and thereby mediated the PMN-MDSC influx. The authors proceeded to combine CSF1R inhibition with selective CXCR2 inhibition, resulting in a delay in tumor progression in lung carcinoma and melanoma models (Kumar et al., 2017). Moreover, CSF1 was found to influence the CAF compartment specifically in the mesenchymal PDAC subtype. Steins et al described an deactivation of pancreatic stellate cells via CSF1 secretion from mesenchymal tumor cells, accounting for the low stromal content in the mesenchymal subtype (Steins et al., 2020). In addition to Csf1, Il34, a chemokine binding the Csf1r receptor as well, was equally secreted at high levels in the mesenchymal subtype. Similarly to Csf1, it was shown that Il34 mediates macrophage recruitment and leads to an exclusion of T cells in murine cancer mouse models (Hama et al., 2020). A high co-expression of CSF1 and IL34 in lung cancer patients was associated with a poor survival, an association particularly strong in advanced stages of this tumor type (Baghdadi et al., 2018). Thus, a combinatorial approach to inhibit CSF1 and IL34, either by inhibiting both factors through antibody-mediated ablation or by targeting the common CSF1R receptor, could be an effective approach to modulate antitumor immunity in PDAC.

In the classical PDAC subtype, we identified *Cxcl5* as top differentially secreted factor and inferred that *Cxcl5-Cxcr2* signaling leads to an accumulation of PMN-MDSCs in the TME. CXCL5 was recently described in the context of prostate cancer to be associated with higher PMN-MDSC infiltration (Bezzi et al., 2018). Moreover, Raghavan et al identified CXCL5 as differentially secreted factor enriched in the classical tumor cell state in a scRNA-seq data set of patient-derived metastatic PDAC (Raghavan et al., 2021). Across TCGA cancer cohorts, *CXCL5* expression levels were generally highest in PDAC. Furthermore, it was shown that *Cxcl5* expression in tumor cells is mediated by NF-kB activation via TNFα in a PDAC mouse model. Subsequent inhibition of the Cxcr2 receptor led to delayed tumor growth in mice and to infiltration of activated T cells (Chao et al., 2016). Combination of CXCR2 inhibitors with anti-PD1 immunotherapy entailed significant longer survival time in a PDAC mouse model and highlights the immunosuppressive effects of Cxcr2 expressing PMN-MDSCs in PDAC (Steele et al., 2016). Besides Cxcl5, we identified other chemokines which were significantly enriched in classical PDAC, among them Cxcl1 and Cxcl16. PDAC cell derived Cxcl1 was previously reported to induce a T cell excluded TME with high infiltration of MDSCs. Further analysis of tumor cell intrinsic properties showed that *Cxcl1* expression is induced by higher c-Myc activity in tumor cells, thus presenting a potential therapeutic vulnerability. Tumor cell specific knockout of Cxcl1 followed by implantation into mice led to higher infiltration of PD-1$^+$CD8$^+$ T cells accompanied by a lower infiltration of PMN-MDSCs, thereby inducing antitumor immunity (Li et al., 2018). We identified *Cxcl16* secreted by classical tumor cells as well as macrophages as abundant sources in classical tumors, communicating with the *Cxcr6* receptor on T cells. Previous reports suggest that CXCL16 has a role in PDAC tumor progression and induces PDAC cell invasiveness (Wente et al., 2008). As T cell abundance in both PDAC subtypes is negligible and T cells are excluded from the tumor core, the *Cxcl16-Cxcr6* interaction axis did not lead to increased T cell trafficking in both PDAC subtypes. Notably, Lesch et al recently showed that T cells equipped with CXCR6 and a chimeric antigen receptor (CAR) mediated higher T cell infiltration in a subcutaneous PDAC model and thus enhanced adoptive T cell transfer efficacy (Lesch et al., 2021). This study highlights the importance of considering context-specific characteristics of cell-cell communication networks and to simultaneously assess quantitative infiltration and spatial distribution of interacting cell types. Moreover, we identified Cxcl12-Cxcr4 as mesenchymal tumor cell secreted factor signaling, which is known to suppress T cell influx and accumulation of T cells within the tumor (Wang et al., 2022). Cxcl12 was further described to be secreted by FAP$^+$ CAFs in a mouse PDAC model (PKP genotype), leading to coating of the tumor cells with Cxcl12. Inhibition of the cognate receptor Cxcr4 induced T cell infiltration and synergized with anti PD-L1 therapy (Feig et al., 2013; Wang et al., 2022).

5.3.2. Immune-immune crosstalk in PDAC

Our comprehensive cell-cell communication analysis of subtype-specific secreted cytokines and chemokines indicated that immunosuppression is mainly achieved via the recruitment of immunosuppressive macrophages or PMN-MDSCs in both subtypes. Therefore, we next investigated how macrophages and PMN-MDSCs communicate with T cells and sustain a dysfunctional and exhausted T cell compartment. Investigating global differences in cell-cell contact signaling, the mesenchymal subtype was associated with upregulation of multiple immune checkpoint signaling pathways, such as PD-L1, TIGIT and CD80, as well as antigen processing pathways (MHCI and MHCII) compared to the classical subtype. Elevated TIGIT expression levels were described by Steele et al in a subset of CD8$^+$ T cells within human PDAC as well as in the patient's blood presenting a potential biomarker for advanced disease as well as a therapeutic vulnerability for immunotherapy (Steele et al., 2020). Using our combinatorial therapy, we could show that the mesenchymal subtype benefitted more from anti PD-L1 therapy after TME reprogramming than the classical subtype (Falcomatà et al., 2022). Interactions between macrophages and T cells via cell-cell contact (e.g. MHC, ICOS, NOTCH and PD-L1 signaling) and secreted signaling are mostly shared between the mesenchymal and classical subtype, indicating that the higher abundance of macrophages in the mesenchymal subtype mediates immunosuppression. Moreover, we also identified Cxcl16 as macrophage-secreted chemokine whose function was described in the previous paragraph.

Less interactions were identified between neutrophils and T cells, but we found few interactions which are specific for the classical subtype, such as *App-Cd74* and *Mif-Cd74+Cd44*. *App* (Amyloid β) is discussed as the causal protein for neurodegenerative disorders and mediates Amyloid-driven formation of neutrophil extracellular traps (NETosis) in Alzheimer's, thus predicting poor prognosis (Munir et al., 2021). There are limited studies linking neutrophils and T cells via APP in cancer, although APP is generally associated with a pro tumorigenic function (Lee et al., 2021).

MIF is known to be widely expressed in various immune cell types and has autocrine or paracrine functions which mediate immunosuppression (Noe and Mitchell, 2020). Moreover, a high expression of MIF in human PDAC specimens was correlated with a poor prognosis (Funamizu et al., 2013; Wang et al., 2018). In cancer, MIF signaling leads to a reduced cytotoxic T cell activation, fostering activation-induced T cell death via IFNγ signaling (Noe and Mitchell, 2020; Yan et al., 2006).

5.4. Outlook

In this study, we present a comprehensive analysis of TME states and cell-cell communication networks in PDAC subtypes. Our results show multiple potential targets for therapeutic intervention by immunomodulation and reprogramming of the PDAC TME.

The identified subtype-specific secreted factors will be functionally validated *in vivo* in future experiments to fully understand their effect on the TME composition. To this end, we will employ genetic knockouts via CRISPR-Cas9 and overexpression constructs of secreted factors in classical and mesenchymal PDAC cell lines and implant them into syngeneic mice. This will shed light on the question to which extent tumor cells mediate myeloid cell recruitment as well as T cell exclusion and exhaustion by modulating the amount of immunosuppressive myeloid cells. As immune cell infiltration is potentially driven by multiple chemokines and cytokines, we will also generate multiplexed genetic knockouts to investigate if these factors act synergistically.

Another intriguing question is how tumor cells intrinsically regulate secreted factor expression and if there are differences between subtypes. Therefore, we will investigate ATAC-seq and ChIP-seq data from our *Kras*^{G12D}-driven mouse cell line cohort to identify transcription factor programs associated to chemokine/cytokine expression and potentially targetable by epigenetic modifiers. Moreover, our analysis will be extended to human PDAC data sets to cross-validate our inferred cell-cell communication networks, using publicly available human scRNA-seq data sets and integrating them with secretome analysis of human PDAC cell lines which are available in our lab. These additional analyses will build an extensive framework for PDAC subtype-specific immune hubs

6. REFERENCES

Andricovich, J., Perkail, S., Kai, Y., Casasanta, N., Peng, W., and Tzatsos, A. (2018). Loss of KDM6A Activates Super-Enhancers to Induce Gender-Specific Squamous-like Pancreatic Cancer and Confers Sensitivity to BET Inhibitors. Cancer Cell *33*, 512-526.e518.

Armingol, E., Officer, A., Harismendy, O., and Lewis, N.E. (2021). Deciphering cell-cell interactions and communication from gene expression. Nat Rev Genet *22*, 71-88.

Aung, K.L., Fischer, S.E., Denroche, R.E., Jang, G.H., Dodd, A., Creighton, S., Southwood, B., Liang, S.B., Chadwick, D., Zhang, A.*, et al.* (2018). Genomics-Driven Precision Medicine for Advanced Pancreatic Cancer: Early Results from the COMPASS Trial. Clin Cancer Res *24*, 1344-1354.

Baghdadi, M., Endo, H., Takano, A., Ishikawa, K., Kameda, Y., Wada, H., Miyagi, Y., Yokose, T., Ito, H., Nakayama, H.*, et al.* (2018). High co-expression of IL-34 and M-CSF correlates with tumor progression and poor survival in lung cancers. Sci Rep *8*, 418.

Bailey, P., Chang, D.K., Nones, K., Johns, A.L., Patch, A.M., Gingras, M.C., Miller, D.K., Christ, A.N., Bruxner, T.J., Quinn, M.C.*, et al.* (2016). Genomic analyses identify molecular subtypes of pancreatic cancer. Nature *531*, 47-52.

Baslan, T., and Hicks, J. (2017). Unravelling biology and shifting paradigms in cancer with single-cell sequencing. Nat Rev Cancer *17*, 557-569.

Bayne, L.J., Beatty, G.L., Jhala, N., Clark, C.E., Rhim, A.D., Stanger, B.Z., and Vonderheide, R.H. (2012). Tumor-derived granulocyte-macrophage colony-stimulating factor regulates myeloid inflammation and T cell immunity in pancreatic cancer. Cancer Cell *21*, 822-835.

Bear, A.S., Vonderheide, R.H., and O'Hara, M.H. (2020). Challenges and Opportunities for Pancreatic Cancer Immunotherapy. Cancer Cell *38*, 788-802.

Becht, E., McInnes, L., Healy, J., Dutertre, C.-A., Kwok, I.W.H., Ng, L.G., Ginhoux, F., and Newell, E.W. (2019). Dimensionality reduction for visualizing single-cell data using UMAP. Nature biotechnology *37*, 38-44.

Becht, E., McInnes, L., Healy, J., Dutertre, C.A., Kwok, I.W.H., Ng, L.G., Ginhoux, F., and Newell, E.W. (2018). Dimensionality reduction for visualizing single-cell data using UMAP. Nat Biotechnol.

Bezzi, M., Seitzer, N., Ishikawa, T., Reschke, M., Chen, M., Wang, G., Mitchell, C., Ng, C., Katon, J., Lunardi, A.*, et al.* (2018). Diverse genetic-driven immune landscapes dictate tumor progression through distinct mechanisms. Nat Med *24*, 165-175.

Biffi, G., Oni, T.E., Spielman, B., Hao, Y., Elyada, E., Park, Y., Preall, J., and Tuveson, D.A. (2019). IL1-Induced JAK/STAT Signaling Is Antagonized by TGFβ to Shape CAF Heterogeneity in Pancreatic Ductal Adenocarcinoma. Cancer Discov *9*, 282-301.

Binnewies, M., Roberts, E.W., Kersten, K., Chan, V., Fearon, D.F., Merad, M., Coussens, L.M., Gabrilovich, D.I., Ostrand-Rosenberg, S., Hedrick, C.C.*, et al.* (2018). Understanding the tumor immune microenvironment (TIME) for effective therapy. Nat Med *24*, 541-550.

Blagih, J., Zani, F., Chakravarty, P., Hennequart, M., Pilley, S., Hobor, S., Hock, A.K., Walton, J.B., Morton, J.P., Gronroos, E.*, et al.* (2020). Cancer-Specific Loss of p53 Leads to a Modulation of Myeloid and T Cell Responses. Cell Rep *30*, 481-496.e486.

Brahmer, J.R., Tykodi, S.S., Chow, L.Q., Hwu, W.J., Topalian, S.L., Hwu, P., Drake, C.G., Camacho, L.H., Kauh, J., Odunsi, K.*, et al.* (2012). Safety and activity of anti-PD-L1 antibody in patients with advanced cancer. N Engl J Med *366*, 2455-2465.

Bronte, V., Brandau, S., Chen, S.H., Colombo, M.P., Frey, A.B., Greten, T.F., Mandruzzato, S., Murray, P.J., Ochoa, A., Ostrand-Rosenberg, S.*, et al.* (2016). Recommendations for myeloid-derived suppressor cell nomenclature and characterization standards. Nat Commun *7*, 12150.

Bronte, V., Serafini, P., Mazzoni, A., Segal, D.M., and Zanovello, P. (2003). L-arginine metabolism in myeloid cells controls T-lymphocyte functions. Trends Immunol *24*, 302-306.

Candido, J.B., Morton, J.P., Bailey, P., Campbell, A.D., Karim, S.A., Jamieson, T., Lapienyte, L., Gopinathan, A., Clark, W., McGhee, E.J.*, et al.* (2018). CSF1R(+) Macrophages Sustain Pancreatic Tumor Growth through T Cell Suppression and Maintenance of Key Gene Programs that Define the Squamous Subtype. Cell Rep *23*, 1448-1460.

Chan-Seng-Yue, M., Kim, J.C., Wilson, G.W., Ng, K., Figueroa, E.F., O'Kane, G.M., Connor, A.A., Denroche, R.E., Grant, R.C., McLeod, J.*, et al.* (2020). Transcription phenotypes of pancreatic cancer are driven by genomic events during tumor evolution. Nat Genet *52*, 231-240.

Chao, T., Furth, E.E., and Vonderheide, R.H. (2016). CXCR2-Dependent Accumulation of Tumor-Associated Neutrophils Regulates T-cell Immunity in Pancreatic Ductal Adenocarcinoma. Cancer Immunol Res *4*, 968-982.

Chytil, A., Magnuson, M.A., Wright, C.V., and Moses, H.L. (2002). Conditional inactivation of the TGF-beta type II receptor using Cre:Lox. Genesis *32*, 73-75.

Collisson, E.A., Bailey, P., Chang, D.K., and Biankin, A.V. (2019). Molecular subtypes of pancreatic cancer. Nat Rev Gastroenterol Hepatol *16*, 207-220.

Collisson, E.A., Sadanandam, A., Olson, P., Gibb, W.J., Truitt, M., Gu, S., Cooc, J., Weinkle, J., Kim, G.E., Jakkula, L.*, et al.* (2011). Subtypes of pancreatic ductal adenocarcinoma and their differing responses to therapy. Nat Med *17*, 500-503.

Conroy, T., Desseigne, F., Ychou, M., Bouché, O., Guimbaud, R., Bécouarn, Y., Adenis, A., Raoul, J.L., Gourgou-Bourgade, S., de la Fouchardière, C.*, et al.* (2011). FOLFIRINOX versus gemcitabine for metastatic pancreatic cancer. N Engl J Med *364*, 1817-1825.

Conroy, T., Hammel, P., Hebbar, M., Ben Abdelghani, M., Wei, A.C., Raoul, J.L., Choné, L., Francois, E., Artru, P., Biagi, J.J.*, et al.* (2018). FOLFIRINOX or Gemcitabine as Adjuvant Therapy for Pancreatic Cancer. N Engl J Med *379*, 2395-2406.

Cox, J., and Mann, M. (2008a). MaxQuant enables high peptide identification rates, individualized p.p.b.-range mass accuracies and proteome-wide protein quantification. Nature biotechnology *26*, 1367-1372.

Cox, J., and Mann, M. (2008b). MaxQuant enables high peptide identification rates, individualized p.p.b.-range mass accuracies and proteome-wide protein quantification. Nat Biotechnol *26*, 1367-1372.

Dominguez, C.X., Müller, S., Keerthivasan, S., Koeppen, H., Hung, J., Gierke, S., Breart, B., Foreman, O., Bainbridge, T.W., Castiglioni, A.*, et al.* (2020). Single-Cell RNA Sequencing Reveals Stromal Evolution into LRRC15(+) Myofibroblasts as a Determinant of Patient Response to Cancer Immunotherapy. Cancer Discov *10*, 232-253.

Edge, S.B., and Compton, C.C. (2010). The American Joint Committee on Cancer: the 7th edition of the AJCC cancer staging manual and the future of TNM. Ann Surg Oncol *17*, 1471-1474.

Elyada, E., Bolisetty, M., Laise, P., Flynn, W.F., Courtois, E.T., Burkhart, R.A., Teinor, J.A., Belleau, P., Biffi, G., Lucito, M.S.*, et al.* (2019). Cross-Species Single-Cell Analysis of Pancreatic Ductal Adenocarcinoma Reveals Antigen-Presenting Cancer-Associated Fibroblasts. Cancer Discov *9*, 1102-1123.

Eser, S., Reiff, N., Messer, M., Seidler, B., Gottschalk, K., Dobler, M., Hieber, M., Arbeiter, A., Klein, S., Kong, B.*, et al.* (2013). Selective requirement of PI3K/PDK1 signaling for Kras oncogene-driven pancreatic cell plasticity and cancer. Cancer Cell *23*, 406-420.

Falcomatà, C., Bärthel, S., Schneider, G., Saur, D., and Veltkamp, C. (2019). Deciphering the universe of genetic context-dependencies using mouse models of cancer. Curr Opin Genet Dev *54*, 97-104.

Falcomatà, C., Bärthel, S., Ulrich, A., Diersch, S., Veltkamp, C., Rad, L., Boniolo, F., Solar, M., Steiger, K., Seidler, B.*, et al.* (2021). Genetic Screens Identify a Context-Specific PI3K/p27Kip1 Node Driving Extrahepatic Biliary Cancer. Cancer Discov *11*, 3158-3177.

Falcomatà, C., Bärthel, S., Widholz, S.A., Schneeweis, C., Montero, J.J., Toska, A., Mir, J., Kaltenbacher, T., Heetmeyer, J., Swietlik, J.J.*, et al.* (2022). Selective multi-kinase inhibition sensitizes mesenchymal pancreatic cancer to immune checkpoint blockade by remodeling the tumor microenvironment. Nat Cancer.

Feig, C., Jones, J.O., Kraman, M., Wells, R.J., Deonarine, A., Chan, D.S., Connell, C.M., Roberts, E.W., Zhao, Q., Caballero, O.L.*, et al.* (2013). Targeting CXCL12 from FAP-expressing carcinoma-associated fibroblasts synergizes with anti-PD-L1 immunotherapy in pancreatic cancer. Proc Natl Acad Sci U S A *110*, 20212-20217.

Funamizu, N., Hu, C., Lacy, C., Schetter, A., Zhang, G., He, P., Gaedcke, J., Ghadimi, M.B., Ried, T., Yfantis, H.G.*, et al.* (2013). Macrophage migration inhibitory factor induces epithelial to mesenchymal transition, enhances tumor aggressiveness and predicts clinical outcome in resected pancreatic ductal adenocarcinoma. Int J Cancer *132*, 785-794.

Giladi, A., and Amit, I. (2018). Single-Cell Genomics: A Stepping Stone for Future Immunology Discoveries. Cell *172*, 14-21.

Goswami, S., Anandhan, S., Raychaudhuri, D., and Sharma, P. (2022). Myeloid cell-targeted therapies for solid tumours. Nat Rev Immunol.

Grünwald, B.T., Devisme, A., Andrieux, G., Vyas, F., Aliar, K., McCloskey, C.W., Macklin, A., Jang, G.H., Denroche, R., Romero, J.M.*, et al.* (2021). Spatially confined sub-tumor microenvironments in pancreatic cancer. Cell *184*, 5577-5592.e5518.

Hama, N., Kobayashi, T., Han, N., Kitagawa, F., Kajihara, N., Otsuka, R., Wada, H., Lee, H.K., Rhee, H., Hasegawa, Y.*, et al.* (2020). Interleukin-34 Limits the Therapeutic Effects of Immune Checkpoint Blockade. iScience *23*, 101584.

Han, J., DePinho, R.A., and Maitra, A. (2021). Single-cell RNA sequencing in pancreatic cancer. Nat Rev Gastroenterol Hepatol *18*, 451-452.

Hanahan, D. (2022). Hallmarks of Cancer: New Dimensions. Cancer Discov *12*, 31-46.

Hanahan, D., and Weinberg, R.A. (2011). Hallmarks of cancer: the next generation. Cell *144*, 646-674.

Hao, Y., Hao, S., Andersen-Nissen, E., Mauck, W.M., 3rd, Zheng, S., Butler, A., Lee, M.J., Wilk, A.J., Darby, C., Zager, M.*, et al.* (2021). Integrated analysis of multimodal single-cell data. Cell *184*, 3573-3587.e3529.

Hennecke, J., and Wiley, D.C. (2001). T cell receptor-MHC interactions up close. Cell *104*, 1-4.

Hingorani, S.R., Petricoin, E.F., Maitra, A., Rajapakse, V., King, C., Jacobetz, M.A., Ross, S., Conrads, T.P., Veenstra, T.D., Hitt, B.A.*, et al.* (2003). Preinvasive and invasive ductal pancreatic cancer and its early detection in the mouse. Cancer Cell *4*, 437-450.

Hosein, A.N., Brekken, R.A., and Maitra, A. (2020). Pancreatic cancer stroma: an update on therapeutic targeting strategies. Nat Rev Gastroenterol Hepatol *17*, 487-505.

Hosein, A.N., Huang, H., Wang, Z., Parmar, K., Du, W., Huang, J., Maitra, A., Olson, E., Verma, U., and Brekken, R.A. (2019). Cellular heterogeneity during mouse pancreatic ductal adenocarcinoma progression at single-cell resolution. JCI Insight *5*.

Hruban, R.H., Goggins, M., Parsons, J., and Kern, S.E. (2000). Progression model for pancreatic cancer. Clin Cancer Res *6*, 2969-2972.

Huang, H., Wang, Z., Zhang, Y., Pradhan, R.N., Ganguly, D., Chandra, R., Murimwa, G., Wright, S., Gu, X., Maddipati, R.*, et al.* (2022). Mesothelial cell-derived antigen-presenting cancer-associated fibroblasts induce expansion of regulatory T cells in pancreatic cancer. Cancer Cell.

Hutton, C., Heider, F., Blanco-Gomez, A., Banyard, A., Kononov, A., Zhang, X., Karim, S., Paulus-Hock, V., Watt, D., Steele, N.*, et al.* (2021). Single-cell analysis defines a pancreatic fibroblast lineage that supports anti-tumor immunity. Cancer Cell *39*, 1227-1244.e1220.

Ijichi, H., Chytil, A., Gorska, A.E., Aakre, M.E., Fujitani, Y., Fujitani, S., Wright, C.V., and Moses, H.L. (2006). Aggressive pancreatic ductal adenocarcinoma in mice caused by pancreas-specific blockade of transforming growth factor-beta signaling in cooperation with active Kras expression. Genes Dev *20*, 3147-3160.

Jackson, E.L., Willis, N., Mercer, K., Bronson, R.T., Crowley, D., Montoya, R., Jacks, T., and Tuveson, D.A. (2001). Analysis of lung tumor initiation and progression using conditional expression of oncogenic K-ras. Genes Dev *15*, 3243-3248.

Jiang, H., Hegde, S., Knolhoff, B.L., Zhu, Y., Herndon, J.M., Meyer, M.A., Nywening, T.M., Hawkins, W.G., Shapiro, I.M., Weaver, D.T.*, et al.* (2016). Targeting focal adhesion kinase renders pancreatic cancers responsive to checkpoint immunotherapy. Nat Med *22*, 851-860.

Jin, S., Guerrero-Juarez, C.F., Zhang, L., Chang, I., Ramos, R., Kuan, C.H., Myung, P., Plikus, M.V., and Nie, Q. (2021). Inference and analysis of cell-cell communication using CellChat. Nat Commun *12*, 1088.

Juiz, N., Elkaoutari, A., Bigonnet, M., Gayet, O., Roques, J., Nicolle, R., Iovanna, J., and Dusetti, N. (2020). Basal-like and classical cells coexist in pancreatic cancer revealed by single-cell analysis on biopsy-derived pancreatic cancer organoids from the classical subtype. Faseb j *34*, 12214-12228.

Kalimuthu, N., Wilson, G.W., Grant, R.C., Seto, M., O'Kane, G., Vajpeyi, R., Notta, F., Gallinger, S., and Chetty, R. (2020). Morphological classification of pancreatic ductal adenocarcinoma that predicts molecular subtypes and correlates with clinical outcome. Gut *69*, 317-328.

Kanda, M., Matthaei, H., Wu, J., Hong, S.M., Yu, J., Borges, M., Hruban, R.H., Maitra, A., Kinzler, K., Vogelstein, B.*, et al.* (2012). Presence of somatic mutations in most early-stage pancreatic intraepithelial neoplasia. Gastroenterology *142*, 730-733.e739.

Katzenelenbogen, Y., Sheban, F., Yalin, A., Yofe, I., Svetlichnyy, D., Jaitin, D.A., Bornstein, C., Moshe, A., Keren-Shaul, H., Cohen, M.*, et al.* (2020). Coupled scRNA-Seq and Intracellular Protein Activity Reveal an Immunosuppressive Role of TREM2 in Cancer. Cell *182*, 872-885.e819.

Kemp, S.B., Carpenter, E.S., Steele, N.G., Donahue, K.L., Nwosu, Z.C., Pacheco, A., Velez-Delgado, A., Menjivar, R.E., Lima, F., The, S.*, et al.* (2021a). Apolipoprotein E Promotes Immune Suppression in Pancreatic Cancer through NF-κB-Mediated Production of CXCL1. Cancer Res *81*, 4305-4318.

Kemp, S.B., Steele, N.G., Carpenter, E.S., Donahue, K.L., Bushnell, G.G., Morris, A.H., The, S., Orbach, S.M., Sirihorachai, V.R., Nwosu, Z.C.*, et al.* (2021b). Pancreatic cancer is marked by complement-high blood monocytes and tumor-associated macrophages. Life Sci Alliance *4*.

Klimstra, D.S., Pitman, M.B., and Hruban, R.H. (2009). An algorithmic approach to the diagnosis of pancreatic neoplasms. Arch Pathol Lab Med *133*, 454-464.

Kloesch, B., Ionasz, V., Paliwal, S., Hruschka, N., Martinez de Villarreal, J., Öllinger, R., Mueller, S., Dienes, H.P., Schindl, M., Gruber, E.S.*, et al.* (2022). A GATA6-centred gene regulatory network involving HNFs and ΔNp63 controls plasticity and immune escape in pancreatic cancer. Gut *71*, 766-777.

Krieger, T.G., Le Blanc, S., Jabs, J., Ten, F.W., Ishaque, N., Jechow, K., Debnath, O., Leonhardt, C.S., Giri, A., Eils, R.*, et al.* (2021). Single-cell analysis of patient-derived PDAC organoids reveals cell state heterogeneity and a conserved developmental hierarchy. Nat Commun *12*, 5826.

Krimpenfort, P., Quon, K.C., Mooi, W.J., Loonstra, A., and Berns, A. (2001). Loss of p16Ink4a confers susceptibility to metastatic melanoma in mice. Nature *413*, 83-86.

Kumar, V., Donthireddy, L., Marvel, D., Condamine, T., Wang, F., Lavilla-Alonso, S., Hashimoto, A., Vonteddu, P., Behera, R., Goins, M.A.*, et al.* (2017). Cancer-Associated Fibroblasts Neutralize the Anti-tumor Effect of CSF1 Receptor Blockade by Inducing PMN-MDSC Infiltration of Tumors. Cancer Cell *32*, 654-668.e655.

Lee, C.L., Moding, E.J., Huang, X., Li, Y., Woodlief, L.Z., Rodrigues, R.C., Ma, Y., and Kirsch, D.G. (2012). Generation of primary tumors with Flp recombinase in FRT-flanked p53 mice. Dis Model Mech *5*, 397-402.

Lee, H.N., Jeong, M.S., and Jang, S.B. (2021). Molecular Characteristics of Amyloid Precursor Protein (APP) and Its Effects in Cancer. Int J Mol Sci *22*.

Lesch, S., Blumenberg, V., Stoiber, S., Gottschlich, A., Ogonek, J., Cadilha, B.L., Dantes, Z., Rataj, F., Dorman, K., Lutz, J.*, et al.* (2021). T cells armed with C-X-C chemokine receptor type 6 enhance adoptive cell therapy for pancreatic tumours. Nat Biomed Eng *5*, 1246-1260.

Lesokhin, A.M., Hohl, T.M., Kitano, S., Cortez, C., Hirschhorn-Cymerman, D., Avogadri, F., Rizzuto, G.A., Lazarus, J.J., Pamer, E.G., Houghton, A.N.*, et al.* (2012). Monocytic CCR2(+) myeloid-derived suppressor cells promote immune escape by limiting activated CD8 T-cell infiltration into the tumor microenvironment. Cancer Res *72*, 876-886.

Li, J., Byrne, K.T., Yan, F., Yamazoe, T., Chen, Z., Baslan, T., Richman, L.P., Lin, J.H., Sun, Y.H., Rech, A.J.*, et al.* (2018). Tumor Cell-Intrinsic Factors Underlie Heterogeneity of Immune Cell Infiltration and Response to Immunotherapy. Immunity *49*, 178-193.e177.

Lin, W., Noel, P., Borazanci, E.H., Lee, J., Amini, A., Han, I.W., Heo, J.S., Jameson, G.S., Fraser, C., Steinbach, M.*, et al.* (2020). Single-cell transcriptome analysis of tumor and stromal compartments of pancreatic ductal adenocarcinoma primary tumors and metastatic lesions. Genome Med *12*, 80.

Liudahl, S.M., Betts, C.B., Sivagnanam, S., Morales-Oyarvide, V., da Silva, A., Yuan, C., Hwang, S., Grossblatt-Wait, A., Leis, K.R., Larson, W.*, et al.* (2021). Leukocyte Heterogeneity in Pancreatic Ductal Adenocarcinoma: Phenotypic and Spatial Features Associated with Clinical Outcome. Cancer Discov *11*, 2014-2031.

Luecken, M.D., and Theis, F.J. (2019). Current best practices in single-cell RNA-seq analysis: a tutorial. Mol Syst Biol *15*, e8746.

Maitra, A., and Hruban, R.H. (2008). Pancreatic cancer. Annu Rev Pathol *3*, 157-188.

Marino, S., Vooijs, M., van Der Gulden, H., Jonkers, J., and Berns, A. (2000). Induction of medulloblastomas in p53-null mutant mice by somatic inactivation of Rb in the external granular layer cells of the cerebellum. Genes Dev *14*, 994-1004.

Martinelli, P., Carrillo-de Santa Pau, E., Cox, T., Sainz, B., Jr., Dusetti, N., Greenhalf, W., Rinaldi, L., Costello, E., Ghaneh, P., Malats, N.*, et al.* (2017). GATA6 regulates EMT and tumour dissemination, and is a marker of response to adjuvant chemotherapy in pancreatic cancer. Gut *66*, 1665-1676.

Maurer, C., Holmstrom, S.R., He, J., Laise, P., Su, T., Ahmed, A., Hibshoosh, H., Chabot, J.A., Oberstein, P.E., Sepulveda, A.R.*, et al.* (2019). Experimental microdissection enables functional harmonisation of pancreatic cancer subtypes. Gut *68*, 1034-1043.

Miyabayashi, K., Baker, L.A., Deschênes, A., Traub, B., Caligiuri, G., Plenker, D., Alagesan, B., Belleau, P., Li, S., Kendall, J.*, et al.* (2020). Intraductal Transplantation Models of Human Pancreatic Ductal Adenocarcinoma Reveal Progressive Transition of Molecular Subtypes. Cancer Discov *10*, 1566-1589.

Moffitt, R.A., Marayati, R., Flate, E.L., Volmar, K.E., Loeza, S.G., Hoadley, K.A., Rashid, N.U., Williams, L.A., Eaton, S.C., Chung, A.H.*, et al.* (2015). Virtual microdissection identifies distinct tumor- and stroma-specific subtypes of pancreatic ductal adenocarcinoma. Nat Genet *47*, 1168-1178.

Mueller, S., Engleitner, T., Maresch, R., Zukowska, M., Lange, S., Kaltenbacher, T., Konukiewitz, B., Öllinger, R., Zwiebel, M., Strong, A., *et al.* (2018). Evolutionary routes and KRAS dosage define pancreatic cancer phenotypes. Nature *554*, 62-68.

Mullard, A. (2021). FDA approves 100th monoclonal antibody product. Nat Rev Drug Discov *20*, 491-495.

Munir, H., Jones, J.O., Janowitz, T., Hoffmann, M., Euler, M., Martins, C.P., Welsh, S.J., and Shields, J.D. (2021). Stromal-driven and Amyloid β-dependent induction of neutrophil extracellular traps modulates tumor growth. Nat Commun *12*, 683.

Nagarsheth, N., Wicha, M.S., and Zou, W. (2017). Chemokines in the cancer microenvironment and their relevance in cancer immunotherapy. Nat Rev Immunol *17*, 559-572.

Nakhai, H., Sel, S., Favor, J., Mendoza-Torres, L., Paulsen, F., Duncker, G.I., and Schmid, R.M. (2007). Ptf1a is essential for the differentiation of GABAergic and glycinergic amacrine cells and horizontal cells in the mouse retina. Development *134*, 1151-1160.

Neefjes, J., Jongsma, M.L., Paul, P., and Bakke, O. (2011). Towards a systems understanding of MHC class I and MHC class II antigen presentation. Nat Rev Immunol *11*, 823-836.

Neesse, A., Algül, H., Tuveson, D.A., and Gress, T.M. (2015). Stromal biology and therapy in pancreatic cancer: a changing paradigm. Gut *64*, 1476-1484.

Neoptolemos, J.P., Kleeff, J., Michl, P., Costello, E., Greenhalf, W., and Palmer, D.H. (2018). Therapeutic developments in pancreatic cancer: current and future perspectives. Nat Rev Gastroenterol Hepatol *15*, 333-348.

Nicolle, R., Blum, Y., Marisa, L., Loncle, C., Gayet, O., Moutardier, V., Turrini, O., Giovannini, M., Bian, B., Bigonnet, M., *et al.* (2017). Pancreatic Adenocarcinoma Therapeutic Targets Revealed by Tumor-Stroma Cross-Talk Analyses in Patient-Derived Xenografts. Cell Rep *21*, 2458-2470.

Noe, J.T., and Mitchell, R.A. (2020). MIF-Dependent Control of Tumor Immunity. Front Immunol *11*, 609948.

O'Reilly, E.M., Oh, D.Y., Dhani, N., Renouf, D.J., Lee, M.A., Sun, W., Fisher, G., Hezel, A., Chang, S.C., Vlahovic, G., *et al.* (2019). Durvalumab With or Without Tremelimumab for Patients With Metastatic Pancreatic Ductal Adenocarcinoma: A Phase 2 Randomized Clinical Trial. JAMA Oncol *5*, 1431-1438.

Öhlund, D., Handly-Santana, A., Biffi, G., Elyada, E., Almeida, A.S., Ponz-Sarvise, M., Corbo, V., Oni, T.E., Hearn, S.A., Lee, E.J., *et al.* (2017). Distinct populations of inflammatory fibroblasts and myofibroblasts in pancreatic cancer. J Exp Med *214*, 579-596.

Olive, K.P., Tuveson, D.A., Ruhe, Z.C., Yin, B., Willis, N.A., Bronson, R.T., Crowley, D., and Jacks, T. (2004). Mutant p53 gain of function in two mouse models of Li-Fraumeni syndrome. Cell *119*, 847-860.

Özdemir, B.C., Pentcheva-Hoang, T., Carstens, J.L., Zheng, X., Wu, C.C., Simpson, T.R., Laklai, H., Sugimoto, H., Kahlert, C., Novitskiy, S.V., *et al.* (2014). Depletion of carcinoma-associated fibroblasts and fibrosis induces immunosuppression and accelerates pancreas cancer with reduced survival. Cancer Cell *25*, 719-734.

Ozga, A.J., Chow, M.T., and Luster, A.D. (2021). Chemokines and the immune response to cancer. Immunity *54*, 859-874.

Palla, G., Spitzer, H., Klein, M., Fischer, D., Schaar, A.C., Kuemmerle, L.B., Rybakov, S., Ibarra, I.L., Holmberg, O., Virshup, I., *et al.* (2022). Squidpy: a scalable framework for spatial omics analysis. Nat Methods *19*, 171-178.

Pathria, P., Louis, T.L., and Varner, J.A. (2019). Targeting Tumor-Associated Macrophages in Cancer. Trends Immunol *40*, 310-327.

Paul, M.E. (2013). Functions of snail homolog 1 (Snail) in pancreatic cancer. In Lehrstuhl für Biotechnologie der Nutztiere (Technische Universität München).

Pijuan-Sala, B., Griffiths, J.A., Guibentif, C., Hiscock, T.W., Jawaid, W., Calero-Nieto, F.J., Mulas, C., Ibarra-Soria, X., Tyser, R.C.V., Ho, D.L.L., *et al.* (2019). A single-cell molecular map of mouse gastrulation and early organogenesis. Nature *566*, 490-495.

Polański, K., Young, M.D., Miao, Z., Meyer, K.B., Teichmann, S.A., and Park, J.E. (2020). BBKNN: fast batch alignment of single cell transcriptomes. Bioinformatics *36*, 964-965.

Puleo, F., Nicolle, R., Blum, Y., Cros, J., Marisa, L., Demetter, P., Quertinmont, E., Svrcek, M., Elarouci, N., Iovanna, J., *et al.* (2018). Stratification of Pancreatic Ductal Adenocarcinomas Based on Tumor and Microenvironment Features. Gastroenterology *155*, 1999-2013.e1993.

Pylayeva-Gupta, Y., Lee, K.E., Hajdu, C.H., Miller, G., and Bar-Sagi, D. (2012). Oncogenic Kras-induced GM-CSF production promotes the development of pancreatic neoplasia. Cancer Cell *21*, 836-847.

Raghavan, S., Winter, P.S., Navia, A.W., Williams, H.L., DenAdel, A., Lowder, K.E., Galvez-Reyes, J., Kalekar, R.L., Mulugeta, N., Kapner, K.S.*, et al.* (2021). Microenvironment drives cell state, plasticity, and drug response in pancreatic cancer. Cell *184*, 6119-6137.e6126.

Rahib, L., Smith, B.D., Aizenberg, R., Rosenzweig, A.B., Fleshman, J.M., and Matrisian, L.M. (2014). Projecting cancer incidence and deaths to 2030: the unexpected burden of thyroid, liver, and pancreas cancers in the United States. Cancer Res *74*, 2913-2921.

Rhim, A.D., Oberstein, P.E., Thomas, D.H., Mirek, E.T., Palermo, C.F., Sastra, S.A., Dekleva, E.N., Saunders, T., Becerra, C.P., Tattersall, I.W.*, et al.* (2014). Stromal elements act to restrain, rather than support, pancreatic ductal adenocarcinoma. Cancer Cell *25*, 735-747.

Royal, R.E., Levy, C., Turner, K., Mathur, A., Hughes, M., Kammula, U.S., Sherry, R.M., Topalian, S.L., Yang, J.C., Lowy, I.*, et al.* (2010). Phase 2 trial of single agent Ipilimumab (anti-CTLA-4) for locally advanced or metastatic pancreatic adenocarcinoma. J Immunother *33*, 828-833.

Sahai, E., Astsaturov, I., Cukierman, E., DeNardo, D.G., Egeblad, M., Evans, R.M., Fearon, D., Greten, F.R., Hingorani, S.R., Hunter, T.*, et al.* (2020). A framework for advancing our understanding of cancer-associated fibroblasts. Nat Rev Cancer *20*, 174-186.

Schneider, G., Schmidt-Supprian, M., Rad, R., and Saur, D. (2017). Tissue-specific tumorigenesis: context matters. Nat Rev Cancer *17*, 239-253.

Schönhuber, N., Seidler, B., Schuck, K., Veltkamp, C., Schachtler, C., Zukowska, M., Eser, S., Feyerabend, T.B., Paul, M.C., Eser, P.*, et al.* (2014). A next-generation dual-recombinase system for time- and host-specific targeting of pancreatic cancer. Nat Med *20*, 1340-1347.

Siegel, R.L., Miller, K.D., Fuchs, H.E., and Jemal, A. (2022). Cancer statistics, 2022. CA Cancer J Clin *72*, 7-33.

Somerville, T.D.D., Xu, Y., Miyabayashi, K., Tiriac, H., Cleary, C.R., Maia-Silva, D., Milazzo, J.P., Tuveson, D.A., and Vakoc, C.R. (2018). TP63-Mediated Enhancer Reprogramming Drives the Squamous Subtype of Pancreatic Ductal Adenocarcinoma. Cell Rep *25*, 1741-1755.e1747.

Stanley, E.R., and Chitu, V. (2014). CSF-1 receptor signaling in myeloid cells. Cold Spring Harb Perspect Biol *6*.

Steele, C.W., Karim, S.A., Leach, J.D.G., Bailey, P., Upstill-Goddard, R., Rishi, L., Foth, M., Bryson, S., McDaid, K., Wilson, Z.*, et al.* (2016). CXCR2 Inhibition Profoundly Suppresses Metastases and Augments Immunotherapy in Pancreatic Ductal Adenocarcinoma. Cancer Cell *29*, 832-845.

Steele, N.G., Carpenter, E.S., Kemp, S.B., Sirihorachai, V., The, S., Delrosario, L., Lazarus, J., Amir, E.D., Gunchick, V., Espinoza, C.*, et al.* (2020). Multimodal Mapping of the Tumor and Peripheral Blood Immune Landscape in Human Pancreatic Cancer. Nat Cancer *1*, 1097-1112.

Steins, A., van Mackelenbergh, M.G., van der Zalm, A.P., Klaassen, R., Serrels, B., Goris, S.G., Kocher, H.M., Waasdorp, C., de Jong, J.H., Tekin, C.*, et al.* (2020). High-grade mesenchymal pancreatic ductal adenocarcinoma drives stromal deactivation through CSF-1. EMBO Rep *21*, e48780.

Sun, G., Li, Z., Rong, D., Zhang, H., Shi, X., Yang, W., Zheng, W., Sun, G., Wu, F., Cao, H.*, et al.* (2021). Single-cell RNA sequencing in cancer: Applications, advances, and emerging challenges. Mol Ther Oncolytics *21*, 183-206.

Tabula Muris, C., Overall, c., Logistical, c., Organ, c., processing, Library, p., sequencing, Computational data, a., Cell type, a., Writing, g.*, et al.* (2018). Single-cell transcriptomics of 20 mouse organs creates a Tabula Muris. Nature *562*, 367-372.

Thorsson, V., Gibbs, D.L., Brown, S.D., Wolf, D., Bortone, D.S., Ou Yang, T.H., Porta-Pardo, E., Gao, G.F., Plaisier, C.L., Eddy, J.A.*, et al.* (2018). The Immune Landscape of Cancer. Immunity *48*, 812-830.e814.

Tiriac, H., Belleau, P., Engle, D.D., Plenker, D., Deschênes, A., Somerville, T.D.D., Froeling, F.E.M., Burkhart, R.A., Denroche, R.E., Jang, G.H.*, et al.* (2018). Organoid Profiling Identifies Common Responders to Chemotherapy in Pancreatic Cancer. Cancer Discov *8*, 1112-1129.

Traag, V.A., Waltman, L., and van Eck, N.J. (2019). From Louvain to Leiden: guaranteeing well-connected communities. Sci Rep *9*, 5233.

Tu, M., Klein, L., Espinet, E., Georgomanolis, T., Wegwitz, F., Li, X., Urbach, L., Danieli-Mackay, A., Küffer, S., Bojarczuk, K.*, et al.* (2021). TNF-α-producing macrophages determine subtype identity and prognosis via AP1 enhancer reprogramming in pancreatic cancer. Nat Cancer *2*, 1185-1203.

Veglia, F., Hashimoto, A., Dweep, H., Sanseviero, E., De Leo, A., Tcyganov, E., Kossenkov, A., Mulligan, C., Nam, B., Masters, G.*, et al.* (2021a). Analysis of classical neutrophils and polymorphonuclear myeloid-derived suppressor cells in cancer patients and tumor-bearing mice. J Exp Med *218*.

Veglia, F., Sanseviero, E., and Gabrilovich, D.I. (2021b). Myeloid-derived suppressor cells in the era of increasing myeloid cell diversity. Nat Rev Immunol *21*, 485-498.

Von Hoff, D.D., Ervin, T., Arena, F.P., Chiorean, E.G., Infante, J., Moore, M., Seay, T., Tjulandin, S.A., Ma, W.W., Saleh, M.N.*, et al.* (2013). Increased survival in pancreatic cancer with nab-paclitaxel plus gemcitabine. N Engl J Med *369*, 1691-1703.

Waddell, N., Pajic, M., Patch, A.M., Chang, D.K., Kassahn, K.S., Bailey, P., Johns, A.L., Miller, D., Nones, K., Quek, K.*, et al.* (2015). Whole genomes redefine the mutational landscape of pancreatic cancer. Nature *518*, 495-501.

Waldman, A.D., Fritz, J.M., and Lenardo, M.J. (2020). A guide to cancer immunotherapy: from T cell basic science to clinical practice. Nat Rev Immunol *20*, 651-668.

Wang, D., Wang, R., Huang, A., Fang, Z., Wang, K., He, M., Xia, J.T., and Li, W. (2018). Upregulation of macrophage migration inhibitory factor promotes tumor metastasis and correlates with poor prognosis of pancreatic ductal adenocarcinoma. Oncol Rep *40*, 2628-2636.

Wang, Z., Moresco, P., Yan, R., Li, J., Gao, Y., Biasci, D., Yao, M., Pearson, J., Hechtman, J.F., Janowitz, T.*, et al.* (2022). Carcinomas assemble a filamentous CXCL12-keratin-19 coating that suppresses T cell-mediated immune attack. Proc Natl Acad Sci U S A *119*.

Wellenstein, M.D., and de Visser, K.E. (2018). Cancer-Cell-Intrinsic Mechanisms Shaping the Tumor Immune Landscape. Immunity *48*, 399-416.

Wente, M.N., Gaida, M.M., Mayer, C., Michalski, C.W., Haag, N., Giese, T., Felix, K., Bergmann, F., Giese, N.A., and Friess, H. (2008). Expression and potential function of the CXC chemokine CXCL16 in pancreatic ductal adenocarcinoma. Int J Oncol *33*, 297-308.

Wherry, E.J., and Kurachi, M. (2015). Molecular and cellular insights into T cell exhaustion. Nat Rev Immunol *15*, 486-499.

Witkiewicz, A.K., McMillan, E.A., Balaji, U., Baek, G., Lin, W.C., Mansour, J., Mollaee, M., Wagner, K.U., Koduru, P., Yopp, A.*, et al.* (2015). Whole-exome sequencing of pancreatic cancer defines genetic diversity and therapeutic targets. Nat Commun *6*, 6744.

Wolf, F.A., Angerer, P., and Theis, F.J. (2018). SCANPY: large-scale single-cell gene expression data analysis. Genome Biol *19*, 15.

Yan, X., Orentas, R.J., and Johnson, B.D. (2006). Tumor-derived macrophage migration inhibitory factor (MIF) inhibits T lymphocyte activation. Cytokine *33*, 188-198.

Yang, X., Li, C., Herrera, P.L., and Deng, C.X. (2002). Generation of Smad4/Dpc4 conditional knockout mice. Genesis *32*, 80-81.

Ying, H., Dey, P., Yao, W., Kimmelman, A.C., Draetta, G.F., Maitra, A., and DePinho, R.A. (2016). Genetics and biology of pancreatic ductal adenocarcinoma. Genes Dev *30*, 355-385.

Zhang, L., Li, Z., Skrzypczynska, K.M., Fang, Q., Zhang, W., O'Brien, S.A., He, Y., Wang, L., Zhang, Q., Kim, A.*, et al.* (2020). Single-Cell Analyses Inform Mechanisms of Myeloid-Targeted Therapies in Colon Cancer. Cell *181*, 442-459.e429.

Zhao, C. (2021). Generation and Characterization of genetically engineered mouse models of pancreatic ductal adenocarcinoma. In Fakultät für Medizin (Technische Universität München).

Zhao, E., Stone, M.R., Ren, X., Guenthoer, J., Smythe, K.S., Pulliam, T., Williams, S.R., Uytingco, C.R., Taylor, S.E.B., Nghiem, P.*, et al.* (2021). Spatial transcriptomics at subspot resolution with BayesSpace. Nat Biotechnol *39*, 1375-1384.

Zhu, Y., Herndon, J.M., Sojka, D.K., Kim, K.W., Knolhoff, B.L., Zuo, C., Cullinan, D.R., Luo, J., Bearden, A.R., Lavine, K.J.*, et al.* (2017). Tissue-Resident Macrophages in Pancreatic Ductal Adenocarcinoma Originate from Embryonic Hematopoiesis and Promote Tumor Progression. Immunity *47*, 323-338.e326.

Zilionis, R., Engblom, C., Pfirschke, C., Savova, V., Zemmour, D., Saatcioglu, H.D., Krishnan, I., Maroni, G., Meyerovitz, C.V., Kerwin, C.M.*, et al.* (2019). Single-Cell Transcriptomics of Human and Mouse Lung Cancers Reveals Conserved Myeloid Populations across Individuals and Species. Immunity *50*, 1317-1334.e1310.

7. PUBLICATIONS

First-authorship publications (*peer-reviewed articles)*

Selective multi-kinase inhibition sensitizes mesenchymal pancreatic cancer to immune checkpoint blockade by remodeling the tumor microenvironment**.** Falcomatà, C.*, **Baerthel, S.*,** Widholz, SA, Schneeweis, C., Montero JJ., Toska, A., Mir, J., Kaltenbacher T, Heetmeyer, J., Swietlik JJ., Cheng J., Teodorescu, B., Reichert O., Schmitt C., Grabichler, K., Coluccio, A., Boniolo, F., Veltkamp, C., Zukowska, M., Vargas, AA., Paik WH., Jesinghaus, M., Steiger, K., Maresch, R., Oellinger, R., Ammon T., Baranov O., Robles MS., Rechenberger, J., Kuster, B., Meissner, F., Reichert, M., Flossdorf, M., Rad, R., Schmidt-Supprian, M., Schneider, G., Saur, D. (2022). *Nature Cancer* (doi:10.1038/s43018-021-00326-1)

Genetic screens identify a context-specific PI3K/p27Kip1 node driving extrahepatic biliary cancer. Falcomatà, C.*, **Baerthel, S.*,** Ulrich, A.*, Diersch, S., Veltkamp, C., Rad, L., Boniolo, F., Solar, M., Steiger, K., Seidler, B., Zukowska, M., Madej, J., Wang, M., Oellinger, R., Maresch, R., Barenboim, M., Eser, S., Tschurtschenthaler, M., Mehrabi, A., Roessler, S., Goeppert, B., Kind, A., Schnieke, A., Robles, MS., Bradley, A., Schmid, RM., Schmidt-Supprian, M., Reichert, M., Weichert, W., Sansom, OJ., Morton, JP., Rad, R., Schneider, G., Saur, D. (2021). *Cancer Discovery* (doi: 10.1158/2159-8290.CD-21-0209)

News & views comment

Blocking the road to de-differentiation: HNF1A/KDM6A complex safeguards epithelial integrity in pancreatic cancer. **Baerthel, S.**, Schneider, G., Saur, D. (2020). *EMBO Journal* (doi: 10.15252/embj.2020104759*)*

Review article

Deciphering the universe of genetic context-dependencies using mouse models of cancer. Falcomatà, C.*, **Baerthel, S.*,** Schneider, G., Saur, D., Veltkamp, C. (2019)**.** *Current Opinion in Genetics & Development* (doi: 10.1016/j.gde.2019.04.002)

Co-authorship publications (peer-reviewed):

CRISPR somatic genome engineering and cancer modeling in the mouse pancreas and liver. Kaltenbacher, T.*, Löprich, J.*, Maresch, R., Weber, J., Müller, S., Oellinger, R., Groß, N., Griger, J., de Andrade Krätzig, N., Avramopoulos, P., Ramanujam, D., Brummer, S., Widholz, SA., **Baerthel, S.**, Falcomatà, C., Pfaus, A., Alnatsha, A., Mayerle, J., Schmidt-Supprian, M., Reichert, M., Schneider, G., Ehmer, U., Braun, CJ., Saur, D., Engelhardt, S., Rad, R. (2022). *Nature Protocols* (doi: 10.1038/s41596-021-00677-0)

Mass spectrometry-based draft of the mouse proteome. Giansanti, P.*, Samaras, P.*, Bian, Y.*, Meng, C., Coluccio, A., Frejno, M., Jakubowsky, H., Dobiasch, S., Hazarika, RR., Rechenberger, J., Calzada-Wack, J., Krumm, J., Mueller, S., Lee, C-Y., Wimberger, N., Lautenbacher, L., Hassan, Z., Chang, Y-C., Falcomatà, C., Bayer, FP., **Baerthel, S.**, Schmidt, T., Rad, R., Combs, SE., The, M., Johannes, F., Saur, D., de Angelis, MH., Wilhelm, M., Schneider, G., Kuster, B. (2022) *Nature Methods* (doi: 10.1038/s41592-022-01526-y)

(* indicates shared first-authorship)

8. ACKNOWLEDGEMENTS

I am sincerely thankful to everyone who supported me during my PhD studies, helping me with my research projects or in any other matter. I am very grateful for meeting so many people as colleagues and close friends.

I deeply thank my PhD supervisor Dieter Saur for not only giving me the opportunity to work in his group, but moreover to trusting me handling challenging projects, implementing novel methods and to engage in collaborative work, which undoubtedly influenced my development as scientist. I thank him for everything, and I am also very grateful for his constant support and the multiple opportunities to present my research at conferences.

I would like to thank my thesis committee members Marc Schmidt-Supprian and Laszlo Nagy for all their help and advice.
Marc, whom I thank for his invaluable advice, critical suggestions, and immunology perspective on my research, which immensely improved the project.
Laszlo, whom I sincerely thank for his generous support, scientific knowledge and mentoring over all these years. Most of all I thank him for an exceptional research internship experience in his lab in 2015, which built my fascination for molecular biology and ultimately encouraged me to pursue a PhD.
I would also like to thank Felix Meissner for participating in my thesis committee meetings and giving helpful and critical advice as well as for a great collaboration and the secretome analysis of our cell line cohort.

Moreover, I am also extremely grateful to…

… Chiara Falcomatà for being the most amazing colleague, friend and team player. I want to thank her especially for her scientific enthusiasm, motivation and creativity and simply for going through everything together. Without her help and support these thesis results would have not been possible.

… Sebastian Widholz for his constant, unwavering support, compassion, empathy and for helping me with any situation possible. I thank him further for proofreading my thesis.

… Jack Barton and Saskia Ettl for their great help with orthotopic implantation experiments and flow cytometry support.

… Chen Zhao and Moritz Jesinghaus for generating the invaluable tissue PDAC cohort and conducting the histopathological analysis.

… Albulena Toska and Jonas Mir for showing me all aspects of scRNA-seq sample generation and data analysis. Special thanks to Lena for becoming a great friend and helping me with every scRNA-seq problem.

… Jonathan Swietlik for conducting the MS-based secretomics analysis and for being a great collaboration partner.

… Olga Seelbach and Katja Steiger for technical support with the spatial transcriptomics workflow.

… Giovanni Palla and Fabian Theis for helping with spatial transcriptomics analysis.

… Constantin Schmitt for helping with conditioned media generation, mouse experiments and being part of the TME project team.

… Vanessa Gölling for helping and supporting the TME project and for being a flow cytometry/macrophage expert.

… Kathrin Grabichler, Angelica Arenas Vargas, Cheng-En Lu, Diana David, Sarah Keegan, Bianca Teodorescu, Jeannine Heetmeyer, Fabio Boniolo, Daniele Lucarelli, Salvatore Milite, Christian Schneeweis, Magda Zukowska, Markus Tschurtschenthaler, Juliano Caraballo, Stella Koutsouli, Chuan Shan, Christian Veltkamp and Angelika Ulrich and all other members of the Saur group for all the help with my research projects and being great colleagues.

… Andreas Patsalos and Laszlo Halasz from the Nagy group for recommendations for spatial transcriptomics analysis, such as implementation of the BayesSpace toolkit.

… Toni Lechner for being friends since Florida and supporting each other through our PhD time.

… to all members of the Roland Rad, Günter Schneider and Maximilian Reichert groups for a great collegial and collaborative atmosphere as well as sharing resources and protocols.

Finally, I want to thank my parents, grandparents, parents in law and friends for their unwavering support.

9. APPENDIX

A Gating strategy innate flow cytometry panel

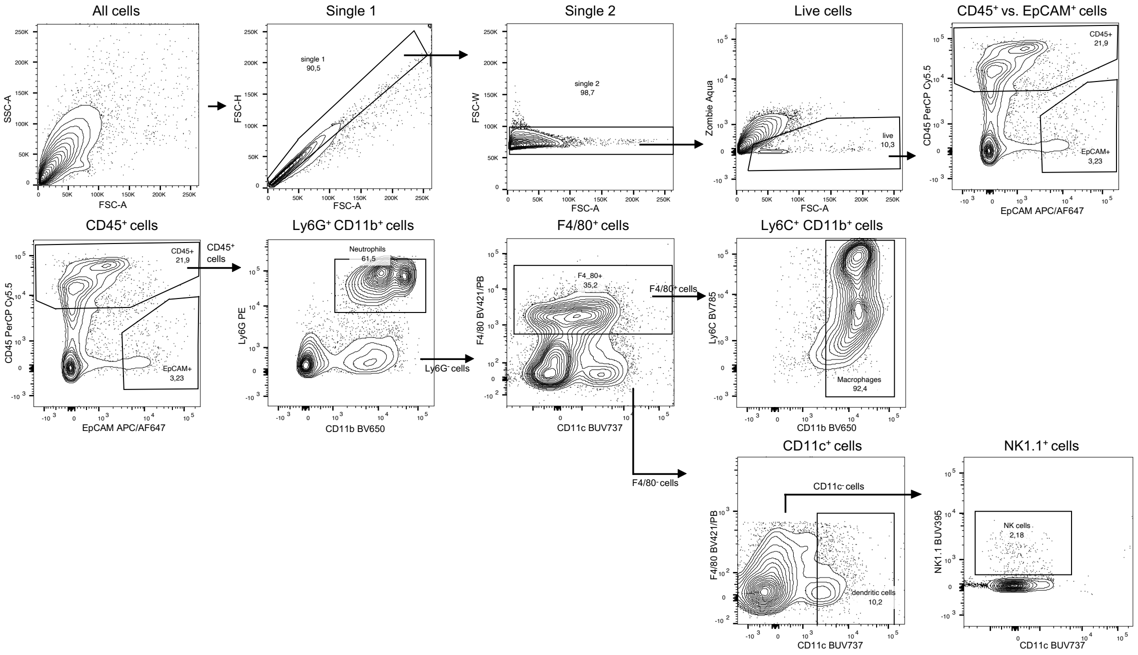

B Gating strategy adaptive flow cytometry panel

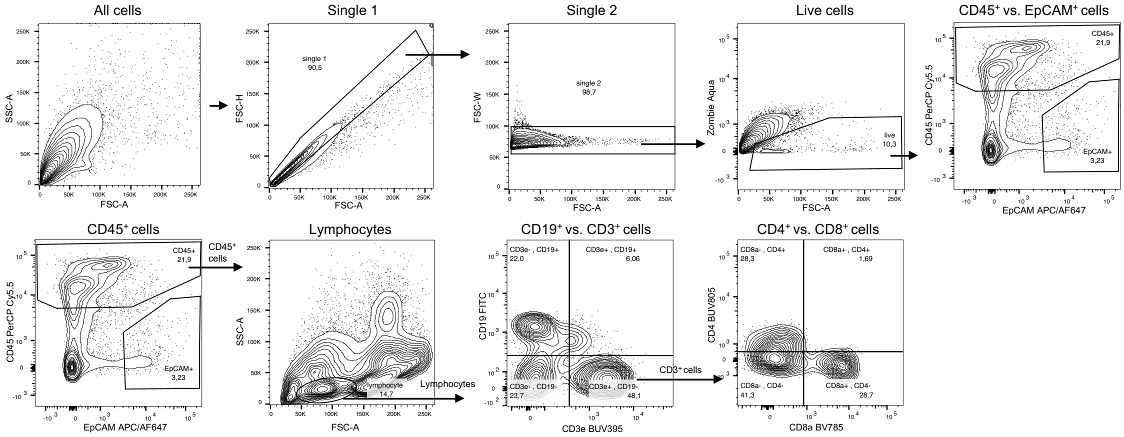

Figure 22. Flow cytometry gating strategy

a, Gating strategy for the innate flow cytometry panel. FSC and SSC gates were used to identify cells and exclude doublets. Live/dead cells were distinguished by Zombie Aqua staining, which stains dead cells. Live cell fraction was further analyzed for innate cell types of interest, which can be analyzed by the following marker combinations: CD45+Ly6G+CD11b+ (Neutrophils), CD45+Ly6G-CD11b+F4/80+ (Macrophages), CD45+Ly6G-F4/80-CD11c+ (Dendritic cells), CD45+Ly6G-F4/80-CD11c-NK1.1+ (NK cells)

b, Gating strategy for the adaptive flow cytometry panel. FSC and SSC gates were used to identify cells and exclude doublets. Live/dead cells were distinguished by Zombie Aqua staining, which stains dead cells. Live cell fraction was further analyzed for adaptive cell types of interest, which can be analyzed by the following marker combinations: CD45+CD3+ (T cells), CD45+CD19+ (B cells), CD45+CD3+CD4+ (CD4+ T cells), CD45+CD3+CD8a+ (CD8+ T cells)